UNIVERSITY OF SOUTHAMPTON

SCHOOL OF CIVIL ENGINEERING AND THE ENVIRONMENT

Violent disturbance and fragmentation of free surfaces

by

Giuseppina Colicchio

Thesis for the degree of Doctor of Philosophy

August 2004

To my family: papà, mamma,
Salvatore and Mario

And to my friend and scientific
father Maurizio

UNIVERSITY OF SOUTHAMPTON

ABSTRACT

SCHOOL OF CIVIL ENGINEERING AND THE ENVIRONMENT

Doctor of Philosophy

VIOLENT DISTURBANCE AND FRAGMENTATION OF FREE SURFACES

by Giuseppina Colicchio

A multi-phase fluid method has been adopted to model the behaviour of fragmenting interfaces. The flow field is described through the solution of the Navier-Stokes equations with an approximate projection method. The interface separating the two phases is captured by a *level-set* function. The interface dynamics and its modelling are the main topics addressed in the present numerical study.

High gradients of density, viscosity, pressure and velocity are localized at the interface. Therefore attention has to be paid to the discretization of the equations in that area. Here, an original variable coefficients ENO scheme and a redefined reinitalizaiton procedure for the Level set function led to higher accuracy. An exponential smoothing of the density and the split of the Poisson equations for the pressure terms improved the stability properties of the solver.

The resulting scheme has been extensively verified and validated through canonical problems, where the method showed good capability of handling: a) high deformation of the interface with breaking and air entrainment; b) generation and evolution of vorticity and c) its interaction with the interface.

Dedicated experiments have been performed for the case of a surface piercing plate in forward motion. Flow visualizations and velocity field measurements were carried out and compared with the numerical results. The globally satisfactory agreements allowed for a synergistic use of the numerical and experimental tools within a parametric analysis. The influence of the Froude number and of the plate inclination have been investigated. The former highlighted the role of the post-breaking phenomena in the definition of the different regimes of interaction between vorticity and free surface. The latter highlighted the influence of the inclination on the occurrence of breaking and on the dynamics of the vorticty released. In particular, very large positive and negative inclinations of the plate prevent energetic breaking.

Contents

List of Figures

List of Tables

Table of notations

General Rules

- Only the most used symbols are listed in the following table
- The meaning of symbols is always given when first introduced in the thesis

Symbols

$\boldsymbol{u}$	Velocity vector
p	Pressure
ϕ	Colour function (for LS distance function)
$c(\phi)$	cut-off function
α	cut-off function
δ_{ρ_w,ρ_a}	Displacement of the smoothing function
C	Correction of the distance function in the reintialization
C^m	Modified correction of the distance function in the reintialization
a_{rs}, a_m	weight function for C and C^m
κ	Curvature
$\mathcal{H}$	Smoothed Heaviside function
w,a	water and air property
ϵ	smoothing parameter
τ	pseudo-time
h	Initial submergence of the plate
d	Still water depth
L	Length of the dam
L_c	Length of the tank
H	Height of the dam
U_{MAX}	Maximum velocity of the surface piercing plate
ρ	Density
σ	Surface tension
μ	Viscosity
$\boldsymbol{D}$	Strain of tensor

$Re = \frac{LU\rho_w}{\mu_w}$	Reynolds number
$We = \frac{LU^2\rho_w}{\sigma}$	Weber number
$Fn = \frac{U}{\sqrt{gh}}$	Froude number

Glossary

BEM	Boundary Element Method
BIE	Boundary Integral Equations
CIP	Constrained Interpolation Profile
ENO	Essentially Non Oscillatory
HLSP	Hybrid Level Set and Particles
LS	Level Set
LSc	Classical Level Set
MAC	Marker and Cell
NS	Navier-Stokes
PIV	Particle Image velocimetry
SPH	Smoothed Particles Hydrodynamics
VOF	Volume Of Fluid

Commonly used Synonymous

The terms air-water interface and interface refer to multi-phase problems, while the term free surface refers to single phase problems. Even though different in their meanings, here these terms are used as synonymous.

I cannot rest from travel;
I will drink life to the less
Ulysses, Alfred Tennyson

Chapter 1

Introduction

The processes of free surface violent deformation and merging are very common in our daily life. While pouring milk into a glass (left image of figure 1.1), it is possible to notice the formation of small drops (fragmentation) that can fall in the milk again (merging). These phenomena happen either when the milk impacts against the glass or against the liquid that is already inside. Fluid fragmentation and merging can develop for all fluids and at very different scales: for example a cloud of bubbles forms at the bottom of waterfalls (see right image of figure 1.1) but also a single drop falling on a solid surface splits into many other smaller drops.

Even though the free surface breaking is such a common phenomenon, the study of its features and the phenomena that accompany it or that are excited by it is still far from complete. The liquid-liquid interactions at the impact and the interaction between the entrapped air and the liquid are difficult to model numerically and to analyze experimentally.

Because of its diverse applications, in recent decades this problem has represented the target of much research. Surface piercing bodies, *e.g.* ships, moving in water can create large deformations and breaking of the sea surface. The same is true for submerged bodies, submarines, close enough to the free surface. The flow around these vessels determines the drag that acts on the hull, the wave pattern and the formation of bubbly regions. Moreover their far wake can make military vessels detectable from satellite (Fingas & Brown, 2001). So good predictions of the detailed flow conditions established in these cases and the physical mechanisms associated with free surface body interactions are acquiring a more and more important role even at the design stage.

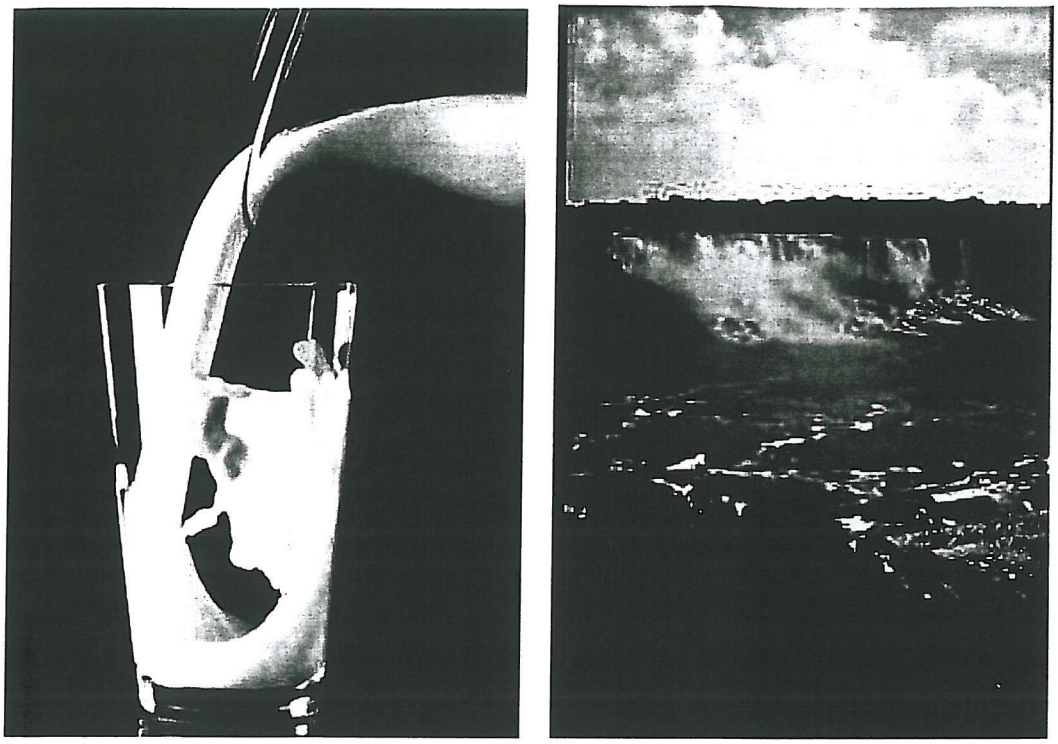

Figure 1.1: Two examples of water fragmentation from our daily life. Left: milk poured into a glass. Right: the Niagara falls.

Apart from naval engineering applications, the study of the violent impact of water waves against solid obstacles is a practical issue for other fields as for environmental science and geology. Periodical storms cause the erosion of shorelines and damage breakwaters. Even though less common than storms, tsunami waves can change the shoreline very quickly and with a result that differs substantially from that of storm waves. The study of the different erosion signatures can help to date back catastrophic tsunami from several geological eras, as those caused by large submarine slides on the continental slope or by the impact of meteorites with the ocean (Bryant & Nott, 2001).

Until a few decades ago (due to its complexity), the phenomena of surface fragmentation was studied only by means of quite simplified analysis. The key factor in the advancing of such study, both from numerical and experimental points of view, has been the understanding that a crucial role during a fragmentation phenomenon is given by the interaction between air and water.

The motion of a mixture of fluids of different natures or in different states, such as gases and liquids as in our case, is referred to as multiphase flow. As multiphase flows are very common in nature and in industrial processes their study is spread

over a large number of disciplines.

In a general form, multiphase fluid flow dynamics encompasses the exchange of heat and possibly chemical reactions between the different phases. So it can be analytically described by a system composed of the mass conservation, the momentum conservation and the energy conservation equations, written over the entire domain, together with some closure of the problem if turbulent flows, chemical reactions or soluble phases are being considered.

The recent availability of large computational power has allowed the development of numerical methods to solve these systems of equations.

Multiphase flow models have been applied in meteorology to study the movement of polluted clouds (Leriche *et al.*, 2001), in metallurgy for the processes of casting and injection of metals (Bai & Thomas, 2001; Im *et al.*, 2001) and mechanical engineering for the interface propagation between the mixture comburent-combustible and exhaust gases (Nguyen *et al.*, 2001).

From an experimental point of view, the types of measurements performed can vary according to the application, the nature of the fluid and the quantity of entrapped gas. Different measuring techniques are available in various applications, from the simple conductivity probes (Hibiki *et al.*, 1998) to X-ray tomography (Seeger *et al.*, 2002). In chemical and nuclear engineering applications bubbly flows are mostly limited to a column of bubbles, so they are spatially limited. For inherently three-dimensional phenomena the measurement of a local void fraction is much more difficult, and optical measurements are affected by the light scattering from the bubbles (Dong *et al.*, 1997). Only recently a 3D version of Particle Image Velocimetry (PIV), the so called defocusing digital particle image velocimetry (DDPIV), has been introduced to detect more accurately the presence of bubbles and their velocity (Pereira & Gharib, 2002). Acoustic measurements of the void fraction have been performed on the ocean surface (Phelps & Leighton, 1998). This is a large scale technique and has not yet been specialized to local measurements.

1.1 Objectives and findings

The aim of this work has been the study of violent (fast, large and non-linear) deformations of an air-water interface with strong interactions with vorticity and entrapped air.

A Navier-Stokes solver with an approximate projection method for the evaluation of the pressure field and a level set function for the tracking of the air-water interface has been used. Novel features include:

- **The splitting of the pressure terms** into two contributions, one independent of the surface tension, and one directly linked to it but independent of the density.
- **The exponential smoothing of the density** across the interface to ensure higher stability of the method.
- **The use of variable coefficients advective Essentially Non Oscillatory (ENO) scheme** to avoid problems of vorticity diffusion across the interface.
- **Improvement of the reinitialization procedure** for the level set function to achieve a higher accuracy of the solver.

The solver has been applied to 2D cases, in order to better control physical and numerical problems. In particular the case of a surface piercing plate has been used to analyze the problems of strong interaction between the deformation of the free surface and the vorticity generated by the body motion. The problems has been analyzed both from a numerical and experimental point of view. The latter has an intrinsic value in the validation of numerical codes. The combined numerical and experimental study made it possible to analyze the effects of the Froude number and the inclination of the plate on the development of the flow.

1.2 Structure of the thesis

The thesis is formally divided into two parts. The first deals with the development and verification of the numerical solver, and the second with its application to practical problems such as that of the surface piercing plate.

In the first part, an introduction to multiphase solvers is presented in chapter 2, through a review of the state of the art. From this study the essential elements for the development of the numerical codes have been derived and later improved and specialized as described in chapter 3. Chapter 4 shows many verifications and validation studies by comparisons with published results, thus showing the capability of the method.

In the second part, the developed numerical method is compared to new measurements of surface piercing plates that were performed in this project. The experimental set-up is described in chapter 5. The numerical and experimental comparison for the vertical plate is shown in chapter 6 and for the inclined plate in chapter 7, confirming the code's capability.

Part I

Development of a numerical method for two-phase flows

Much have I seen and known, –cities of men
and manners, climates, councils, governments,
myself not least, but honour'd of them all.
Ulysses, Alfred Tennyson

Chapter 2

Multiphase flows: the state of the art

In recent decades, Boundary Integral Equations (BIE) methods have been used more frequently than any others to predict the deformation of free surfaces, within the limitations of potential flow theory.

A complete description of such a solver is presented in Longuet-Higgins & Cokelet, 1976. The mathematical use of a velocity potential and a Green function permits the volume integral of the incompressible condition $\int \nabla \cdot \boldsymbol{u} dV = 0$ to be transformed into a surface integral along the boundaries of the fluid domain. The transformation of an nD problem into (n-1)D problem (2D $\rightarrow$ 1D, 3D $\rightarrow$ 2D) allows a much higher accuracy once the number of discrete unknowns has been fixed. The kinematic and dynamic (Bernoulli equation) conditions on the interface complete the system (Brebbia & Power, 1999).

Its computational efficiency and its accuracy have made this technique widespread, and after several decades it has achieved a high reliability, through the detection and correction of shortcomings. Even though this method is very accurate it cannot handle problems with topological changes of the interface and its fragmentation.

The fragmentation of the interface is a limit also when BIEs solvers for multiphase flows with surface tension (Hou *et al.*, 2001) are used.

However, because of the high accuracy in the case of smooth free surfaces, the classic BIE solver have been used, when possible, as a reference for the verification of multiphase codes.

2.1 Numerical modelling

Lagrangian Solvers	Boundary fitted Solvers	Eulerian Solvers
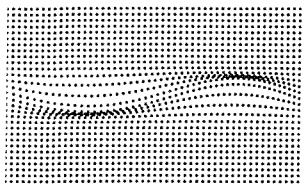 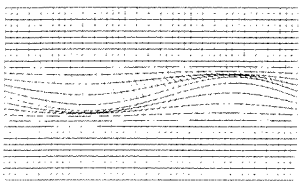 The points where the solution is calculated do not change their properties in time. **SPH**: the particles of fluids (small masses of fluids) are moved with their own velocity, no mesh links them together but their mutual interaction (Colagrossi & Landrini, 2003). **Lagrangian mesh**: A mesh is generated on the whole domain and its nodes move with the velocity obtained integrating the Navier-Stokes equations (Shopov *et al.*, 1990).	 Eulerian meshes are used to discretize each single phase, but their boundaries change in time. Jump conditions are used to link the different phases (Caiden *et al.*, 2001).	 A single fluid with variable properties is considered. The Navier-Stokes equations are discretized on an Eulerian mesh and the position of the interface is obtained with different methods. **Interface tracking**: points are spread on the interface, they are advected in a Lagrangian way (Tryggvason *et al.*, 2001). **Interface capturing**: A colour function is linked to the density so the continuity equation becomes an advection equation for this function (VOF, LS) (Hirt & Nichols, 1981; Sussman *et al.*, 1994). **Hybrid methods:** both a colour function and a set of points are used to trace the interface (HLSP, CIP, MAC) (Yabe *et al.*, 2001). .

Table 2.1: Schematic description of the multiphase solvers, the different colours in the figures represent different phases.

The first attempt at using a multiphase solver can be traced back to 1965 (Harlow & Welch, 1965). The revolutionary idea introduced was to follow the evolution of both air and water with the same equations but different fluid

properties, overcoming the problems of topological changes of the fluid boundary.

Since 1965 different models have been introduced both for the discretization of the equations and for the tracking of the interface.

In table 2.1 there is a brief classification of multiphase flows solvers with some key references. The first distinction is between Lagrangian and Eulerian solvers, between cases where the solution is calculated on moving fluid particles or at fixed points.

There is a third class that can be considered intermediate between these two; the methods falling in this class are referred to as Boundary Fitted Methods (BFM). For them the domain of analysis is divided into deformable sub-domains; the boundaries of each domain adapt themselves to the interface between the fluids. An Eulerian discretization for Navier-Stokes equation is usually adopted inside each domain.

There are two groups of methods that can be classified as properly Lagrangian; one is referred to as a meshless solver and the other uses Lagrangian meshes.

The former method is known as Smoothed Particles Hydrodynamics (SPH) and has been inherited from astrophysics (Monaghan, 1994). At the initial time, the fluid domain is divided in a finite number of particles, each one representing a volume of the fluid mass. This property allows the method to preserve mass intrinsically. The SPH method has been applied mainly to single phase fluids with no surface tension and no viscosity. The multi-phase version has been implemented only recently (Colagrossi & Landrini, 2003). As compressible Euler equations are written for each particle, the real behaviour of the air can be modelled easily, even though some problems of pseudo-compressibility can extend to the water phase. Attempts to model the motion of viscous fluids with surface tension in this way have so far not achieved good results.

The other Lagrangian method (Shopov *et al.*, 1990) uses a mesh whose nodes move with the velocity obtained by solving the Navier-Stokes equations. The motion of nodes can lead to an extreme deformation of the grid and, consequently a regridding technique is necessary; this procedure is time consuming and represents a source of numerical errors since fluid variables have to be projected from the old grid to the new one.

However, if the frequency of regridding is limited, the deformation of the interface can be followed through the grid deformation with very good accuracy. Moreover no smoothing of fluid variables is necessary at the interface.

A drawback of this method is the difficulty of extending it to three dimensional cases.

An intermediate solution between the Lagrangian and the Eulerian solvers is offered by the Boundary Fitted Methods (BFM). For these methods (Caiden *et al.*, 2001) each phase is solved separately and the boundary conditions at the air-water interface are enforced as jump conditions. This allows for different methods to be used in the solution of each phase. Eulerian meshes can still be used, and in this case the cells can be switched off if the fluid they describe is not present. The main advantage that this offers is the possibility of following the deformation of the interface (traced by one of the methods described later for the Eulerian solver) without any smoothing of fluid properties. The main disadvantage is the difficult reconstruction of the jump conditions. In fact applications are limited to 2D cases (Caiden *et al.*, 2001; Li & Yan, 2002).

Most of the methods currently used to model multiphase flows are based on an Eulerian discretization of the Navier-Stokes equations. The grid can be either structured or unstructured, possibly with an adaptive refinement of the discretization where particular conditions occur. For example in Sussman *et al.* (1999) the mesh size is halved where the ratio between the curvature and the mesh size exceeds an *a priori* stated limit. This procedure can be repeated in the smaller cells until this condition is no longer satisfied.

The choice of an Eulerian grid introduces the problem of tracking the interface. Different methods can be used for this purpose; predominantly surface capturing and surface tracking algorithms. The former defines a function explicitly linked to the interface that is advected in an Eulerian way. The latter uses particles spread on the interface or in its neighbourhood to follow the Lagrangian displacement of the interface.

All these methods are direct descendants of the Marker and Cell (MAC) method first introduced in the Los Alamos laboratory. This was based on the idea that a set of particles spread around the interface and advected in a Lagrangian way can locate the material in the cell and define the position of the interface itself (Harlow & Welch, 1965).

The interface tracking methods are the closest to this formulation. For them a set of points is positioned on the interface at the initial time and then convected with the velocity obtained by the Eulerian grid. These points represent a secondary grid of lower order with respect to the one adopted for the solution of

the Navier-Stokes equations and they can either modify the grid to follow the interface, or they can simply be used to recover the physical properties of the fluid (Tryggvason *et al.*, 2001).

The main problem with this kind of tracers is the exact calculation of the velocity at the point on the interface. Usually an interpolation method is adopted, but for high Reynolds numbers it is very likely that the interpolation of quantities characterized by a very steep gradient can cause an increasing error. Moreover interpolation techniques do not generally preserve the mass properly as no physical meaning is associated to them.

The Volume of Fluid (VOF) and the Level Set (LS) are the most popular Eulerian methods. In both cases the position of the interface is derived from the values of a so called colour function ϕ. For the former the colour function ϕ is the void fraction in the cell, while for the latter it is the distance from the interface. As it is possible to write an explicit link between these functions ϕ and the density ρ, an equation of convection can be easily derived for the colour function from mass conservation equation

$$\frac{\partial \rho(\phi)}{\partial t} + \boldsymbol{u} \cdot \nabla \rho(\phi) = 0 \Rightarrow \frac{\partial \rho}{\partial \phi}\left(\frac{\partial \phi}{\partial t} + \boldsymbol{u} \nabla \phi\right) = 0 \, . \tag{2.1}$$

The VOF method, introduced by Hirt & Nichols (1981), represents the mass in the cell explicitly, so that a good numerical scheme to evaluate the evolution of the function should lead to a very good conservation of the mass throughout the computation. Its limitation is the fact that an approximation has to be made of the position of the interface and of its curvature when describing problems characterized by surface tension. A description of the methods currently used to define the normal and the curvature on the interface is in Scardovelli & Zaleski (1999). Various examples of VOF applications can be found for example in Lafaurie *et al.* (1994), Lawson *et al.* (1999) and Zhao *et al.* (2002).

The LS method was first applied to incompressible multiphase flows a decade ago. It was introduced in Sussman *et al.* (1994). In the LS method, ϕ is a function indicating the signed distance from the interface, so that the function is positive if the point is in one of the fluids and negative if it is in the other. Because of the analytical nature of the distance, it provides much more accurate information on the position and curvature of the interface than the corresponding function in the VOF.

The disadvantage of the LS method is the difficulty in preserving the

conservation of mass. The ϕ function solution of equation 2.1 cannot preserve the meaning of a distance function for more than a few time-steps so that a reinitialization is necessary to restore the analytical properties of ϕ. This procedure results in the smoothing of the interface in some cases. Corrections for the procedure of reinitialization can be found in Sussman & Fatemi (1999), Russo & Smereka (2000).

Another choice has been presented in Sussman & Puckett (2000), where LS and VOF methods are combined to preserve the advantages of each of the two schemes.

Then there are some hybrid methods: the hybrid LS-particles method (HLSP) (Enright *et al.*, 2002) and the Constrained Interpolation Profile method (CIP) (Yabe *et al.*, 2001; Yabe *et al.*, 2002). The idea behind the former is the use of Lagrangian markers in a narrow band around the interface. A circle of radius $r(k)$ equal to their distance from the interface itself is associated to each point $k = 1, 2, ..,$ so that the zero level becomes the envelope of all those circles (see figure 2.1). Moreover, a sign $s(k)$ characterizes the markers, to indicate the phase to which they belong.

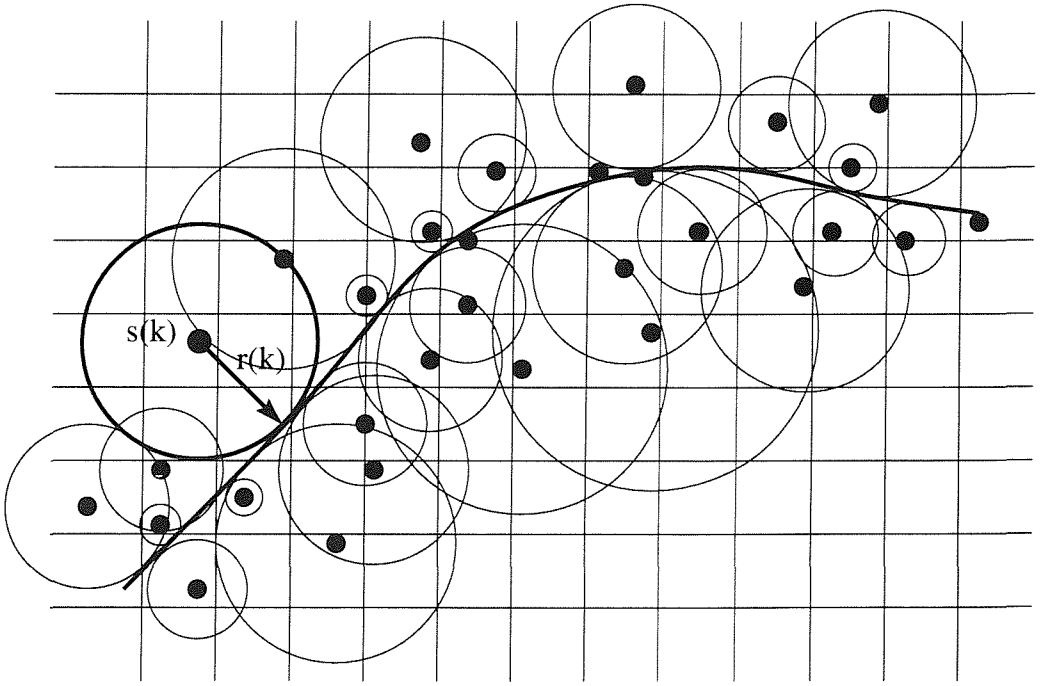

Figure 2.1: Example of the hybrid method HLSP: the k-th particle is characterized by a radius r(k) and a sign; the circle of radius r(k) is tangent to the interface. The envelope of the different circles defines the position of the zero level.

The markers are moved in a Lagrangian fashion and the Level Set function is

updated using equation 2.1. In the process of the Level Set reinitialization the signs $s(k)$ of the markers are used as a check for the sign of the distance at the cell centre. If they differ, the distance associated with the markers in the cell is donated to the cell centre. This procedure is particularly accurate when the velocity field has no steep gradient and when the characteristics are not convergent. Its application becomes more difficult when the velocity is not so smooth, as processes of interpolation have to accommodate the sudden change of the tangential components.

The CIP method introduces a colour function $F(\boldsymbol{x})$ and its gradient $\boldsymbol{G}(\boldsymbol{x})$. After a time Δt the particle that was in the position $\boldsymbol{x}$ has moved to a new position $\boldsymbol{x} + \boldsymbol{u}\Delta t + O(\Delta t^2)$, consequently the colour function, that moves with it, is represented by $F(\boldsymbol{x}+\boldsymbol{u}\Delta t + O(\Delta t^2))$, similarly its gradient is $\boldsymbol{G}(\boldsymbol{x} + \boldsymbol{u}\Delta t + O(\Delta t^2))$. The projections of the new F and $\boldsymbol{G}$ functions on the Eulerian mesh give the position of the interface at the new time step, preserving the slope of the colour function. Figure 2.2 (from (Yabe *et al.*, 2001)) gives a practical idea of how this method works. In plot a) there is the initial profile of the

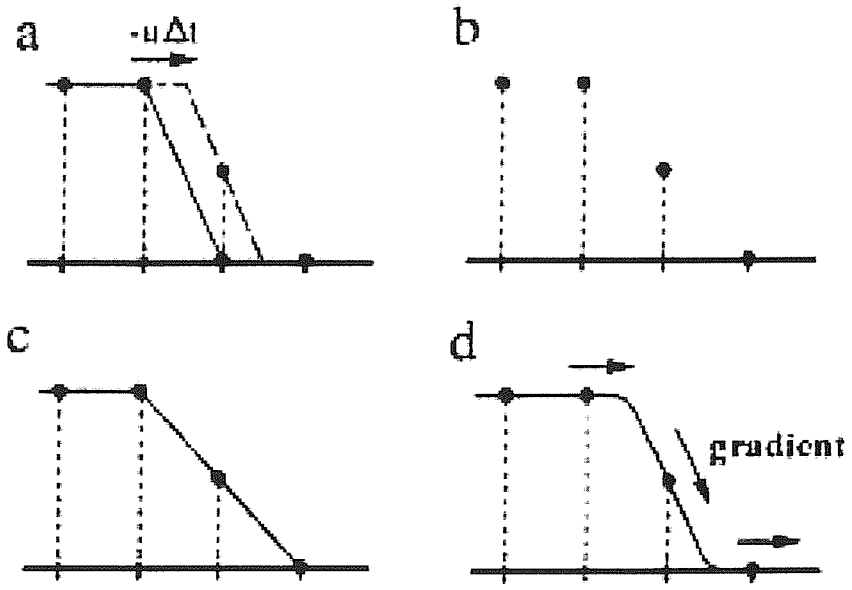

Figure 2.2: Example advection with the CIP method (Yabe *et al.*, 2001).

color function and in dashed line the exact solution after the advection; plot b) shows the discrete solution after the advection. If a linear interpolation is used, the numerical solution produces diffusion (see plot c), that is recovered in d) by the

advection of the spatial derivatives as well.

This method avoids errors in the velocity interpolation, because, the points that transport F and $\boldsymbol{G}$ have coordinates equal to those of the node of the grid (if a non-staggered grid is used). It requires only the projection of an almost smooth function on the mesh. The main difficulties are the choice of a steep transition function F, able to limit the dissipation linked to the problem of advection and reinitialization of the function if it is highly deformed in the advection procedure.

Once the kind of mesh has been selected another choice has to be made about the kind of solver to use. There are essentially three main methods to solve the Navier-Stokes equations with primitive variables[1]: the pseudo-compressibility method, the pseudo-velocity method and the approximate projection method.

The pseudo-compressibility method was first introduced in Chorin (1967) for stationary flows and later extended to non-stationary flows (see Kelecy & Pletcher (1997)). It consists of replacing the continuity equation with one dependent on a pseudo-time τ:

$$\frac{1}{\beta}\frac{\partial p}{\partial \tau} + \nabla \cdot \boldsymbol{u} = 0 \tag{2.2}$$

where β is a constant arbitrarily chosen, that has the dimension of a velocity and represents a pseudo-speed of sound. Pressure and velocity are updated iteratively until equation 2.2 has reached stationary conditions. An implicit scheme can be used for the solution of this system that does not require any matrix manipulation (see Zhao *et al.* (2002) and Helenbrook *et al.* (1999)).

The projection method makes a first approximation of the velocity at the new time step by solving approximated Navier-Stokes equations. The velocity field that is obtained does not satisfy the mass conservation conditions and a velocity correction is needed. This is obtained projecting the momentum conservation equations on a divergence-free space. This procedure leads to a Poisson equation for the pressure correction (Harlow & Welch, 1965; Hirt & Nichols, 1981; Kim & Moin, 1985).

Something similar is done in the pseudo-velocity method. An implicit solution is obtained by the introduction of the guessed velocity (the pseudo-velocity) into a system of equation where the guessed velocity is used as a pseudo-variable alongside the pressure and the actual velocity, in a system of equations upgraded by the splitting of the Navier-Stokes equations. This leads to an implicit solution for the velocity. The only shortcoming is that viscosity and density cannot be

[1]The streamfunction-vorticity formulation is limited to two dimensional or axi-symmetric flows

implicitly introduced into the system but they have to be provided from previous time steps (Rhie & Chow, 1983).

As can be seen from this brief review, there is a large variety of numerical methods, but their properties of numerical stability and accuracy are not well known (Fraigneau *et al.*, 2001; Lemos, 1996; Morinishi *et al.*, 1998). It is possible to show that interface problems for high Reynolds numbers are not well posed, and this means that small variation in the discretization can cause profound changes in the solution (Birkhoff, 1962).

2.2 Experiments

Several detailed experiments have been performed with free surface flows, but only for a limited number of them have measurements been made with breaking interfaces. This is mainly due to practical difficulties in the bubbly regions formed after the impact between portions of the interface.

The experiments performed with breaking interfaces and bubbly flows are mainly of three kinds: a) those where there are measurements available all over the studied fluid domain apart from the bubbly region, b) those that study exclusively the bubbly regions with measurements of bubbles velocity and of void fraction, c) those where large cavities are involved and very few bubbles are generated, so that some measurements of the trapped air are possible.

In the first category of experiments we find for example those performed by Chang & Liu (1998) and Dong *et al.* (1997). Chang & Liu (1998) measured velocities in the tip of a 2D overturning jet and in the flow caused by breaking, with a PIV (Particle imagine velocimetry) method. Unfortunately, owing to the scattering of light in the very thin region of the jet before impact, there was very little data in the interesting region where vertical voriticy is generated.

Dong *et al.* (1997) measured the velocity field around surface piercing bodies, but their measurements did not include the bubbly patch. For instance, during their tests for a surface piercing strut, the free surface and the bow regions are not analysed, even though it is there that vorticity is generated and develops its distinctive features.

Bubbly flows are of interest in many fields and a large variety of experiments falls in the second category. Current measurement techniques are able to measure the void fraction and the velocity of the single bubbles, assuming that all the

bubbles have almost the same spherical shape and dimension. These assumptions are necessary for the use of optical devices, for which the reflection and the refraction of the light are predictable only for spherical bubbles with given diameter (Bonetto & Lahey, 1993; Oakley *et al.*, 1997).

In Gopalan & Katz (2000) the study of the velocity of the bubbles is performed with a PIV technique using a seeding that reflects the light on a different wavelength with respect to the bubble. This is one of the first attempts to measure bubble velocity without any assumption on the shape and size.

In the third category there are experiments that take into account large amounts of air entrapped into water; in this case the likelihood of small bubbles being formed is reduced, and the bubbly region is less important. The experiments by Lawson *et al.* (1999) with a large bursting bubble belong to the same category. In this case the velocity field in the water domain can be calculated quite well and the problems are mainly connected with the definition of the interface. The spherical geometrical nature of this experiment does not permit an easy visualization of the interface. Good visualizations of it are instead available in the experiments by Walters & Davidson (1962), where a two-dimensional bubble of air is created in water.

Another experiment with large amount of air in the water domain is that performed by Zhou *et al.* (1999). A dam-break problem is studied allowing the water to impact against a vertical wall placed downstream the initial dam.

In Zhou *et al.* (1999) measurements of pressure and water height are available, even though they are affected by uncertainties as pointed out by the authors. They are as yet one of the few measurements available for a problem that is easy reproducible numerically, and are therefore useful for the validation of multiphase numerical models.

2.3 Inheritance from the past, and future developments

From a numerical point of view, the introduction of multiphase solvers has revolutionized the way that flow fields which are characterized by air entrainment are modelled.

Several multi-phase solvers have been described here, differing in their ability to model different phenomena that are involved in the fluid motion. For given

conditions, the choice among them should be based mostly on the kind of flow to modelled.

The Eulerian surface capturing solvers are the most versatile, because they can easily model merging and fragmentation, large density and viscosity gradients across the interface as well as surface tension. Nonetheless the implications of the numerical smoothing of physical properties across the interface is still to be understood. Moreover the gaseous phase is commonly described as incompressible and this is still a limitation when thinking of the effects of compressibility on small pockets of air entrapped below violent jets.

The aim of the present work is to formulate and use a model which is as versatile as possible and therefore an Eulerian solver has been chosen. The idea of keeping the computational complexity as small as possible has made the interface capturing solver the most suitable, while the analytical properties of the Level-Set has made this technique more interesting for future development.

Yet all experience is an arch wherethro'
gleams that untravell'd world whose margin fades
for ever and for ever when I move.
Ulysses, Alfred Tennyson

Chapter 3

Numerical modelling

In this chapter the numerical model developed for the two-phase flow problem is described (see for example Sussman *et al.*, 1994). Its features, advantages and challenges are outlined.

3.1 General features

In the present work interfacial flows are dealt with by considering the two phases as a continuous field where any generic fluid property, say f, is defined by patching the corresponding fields in the two phases, that is

$$f = \chi f_{air} + (1 - \chi) f_{water} \ . \tag{3.1}$$

A rapid but smooth transition from one phase to another is guaranteed by the so called bridge function $\chi \in [0, 1]$. The evolution of the resulting compound flow field is described by the Navier-Stokes equations for a continuum fluid with non-uniform properties and, in principle, there is no need to distinguish explicitly between the two phases. Continuity conditions of velocity and tangential stresses at the interface are automatically fulfilled, though in a smoothed sense, while surface-tension effects have to be modelled explicitly. Clearly, most of the numerical difficulties are shifted to the treatment of the bridge function.

In this framework an incompressible fluid in laminar and isothermal conditions is described by the mass and momentum conservation equations:

$$\begin{cases} \nabla \cdot \boldsymbol{u} = 0 \\ \\ \rho \dfrac{D\boldsymbol{u}}{Dt} = -\nabla p + 2\nabla \cdot \mu \boldsymbol{D} + \sigma \kappa \delta_S \boldsymbol{n} + \rho \boldsymbol{g} \ , \end{cases} \tag{3.2}$$

where $\boldsymbol{u}$ is the velocity, p the pressure, ρ the density, μ the viscosity, $\boldsymbol{g}$ the field force and in particular the gravity, σ the surface tension, $\boldsymbol{n}$ the normal to the interface, κ the curvature of the interface and δ_S the Dirac delta function equal to unity on the interface and zero elsewhere. The term $\boldsymbol{D}$ has components

$$(\boldsymbol{D})_{ij} = D_{ij} = \frac{1}{2}\left(\frac{\partial u_j}{\partial x_i} + \frac{\partial u_i}{\partial x_j}\right)$$

and represents the rate of strain tensor.

Within the one-fluid formulation, the conditions at the interface between two viscous fluids are automatically captured, see *e.g.* Wehausen & Laitone (1960).

3.2 Discretization of the Navier-Stokes equations

An Eulerian discretization scheme has been used to solve the set of equations (3.2) rewritten as:

$$\begin{cases} \nabla \cdot \boldsymbol{u} = 0 \\ \dfrac{\partial \boldsymbol{u}}{\partial t} + (\boldsymbol{u} \cdot \nabla)\boldsymbol{u} = -\dfrac{\nabla p}{\rho} + \dfrac{2\nabla \cdot \mu \boldsymbol{D}}{\rho} + \dfrac{2\sigma\kappa\delta_S \boldsymbol{n}}{\rho} + \boldsymbol{g} \, . \end{cases} \tag{3.3}$$

A finite difference solver coupled with a projection scheme is used to solve numerically the system (3.3) on a fixed grid. A second order approximation is adopted both in spatial and time discretizations.

3.2.1 Time discretization

The second order approximation in time is written as

$$\begin{aligned} \frac{\boldsymbol{u}^{n+1} - \boldsymbol{u}^n}{\Delta t} &= -\frac{\nabla p^{n+1/2}}{\rho^{n+1/2}} - [(\boldsymbol{u} \cdot \nabla)\boldsymbol{u}]^{n+1/2} \\ &+ \frac{[2\nabla \cdot \mu \boldsymbol{D}]^{n+1/2}}{\rho^{n+1/2}} + \frac{[\sigma\kappa\delta_S \boldsymbol{n}]^{n+1/2}}{\rho^{n+1/2}} + \boldsymbol{g} \end{aligned} \tag{3.4}$$

and it is solved through a predictor-corrector scheme. The iterative step is repeated until convergence in pressure and velocity fields is reached, improving the stability of the solution (Fraigneau *et al.*, 2001). For brevity the following term is introduced

$$\boldsymbol{F}(\boldsymbol{u}, \boldsymbol{g}, \mu) = -(\boldsymbol{u} \cdot \nabla)\boldsymbol{u} + \frac{2\nabla \cdot \mu \boldsymbol{D}}{\rho} + \boldsymbol{g} \, .$$

It contains all the terms that are approximated with Taylor expansions in the predictor and corrector steps. The iterative procedure is described below.

Predictor step. The density and the surface tension at the time step $n+1/2$ are approximated by using those at the time step $n-1/2$. In the following way, $[F(\boldsymbol{u})]^{n+1/2}$ is obtained through a Taylor expansion from the previous time steps. The predicted pressure gradient ∇p_0 is written as

$$\frac{\nabla p_0^{n+1/2}}{\rho^{n-1/2}} = \frac{\nabla p_0^{n+1/2}}{\rho^{n-1/2}} - \frac{\nabla p^{n-1/2}}{\rho^{n-1/2}} + \frac{\nabla p^{n-1/2}}{\rho^{n-1/2}} \ ,$$

and the two-step procedure to obtain the velocity $\boldsymbol{u}_0^{n+1}$ reads

$$\begin{aligned} \tilde{\boldsymbol{u}} \quad &= \boldsymbol{u}^n + \Delta t \left\{ [F(\boldsymbol{u})]_0^{n+1/2} - \frac{\nabla p^{n-1/2}}{\rho^{n-1/2}} \right\} \\ \boldsymbol{u}_0^{n+1} \quad &= \tilde{\boldsymbol{u}} + \Delta t \left\{ \frac{\nabla p^{n-1/2}}{\rho^{n-1/2}} - \frac{\nabla p_0^{n+1/2}}{\rho^{n-1/2}} + 2\sigma \frac{(\kappa \delta_S \boldsymbol{n})^{n-1/2}}{\rho^{n-1/2}} \right\} \end{aligned} \ . \tag{3.5}$$

For an incompressible fluid, applying the divergence operator, the second equation in (3.5) becomes

$$\frac{\nabla \cdot \tilde{\boldsymbol{u}}}{\Delta t} = \nabla \cdot \left(\frac{\nabla (p^{n-1/2} - p_0^{n+1/2})}{\rho^{n-1/2}} + 2\sigma \frac{(\kappa \delta \boldsymbol{n})^{n-1/2}}{\rho^{n-1/2}} \right) \ .$$

As in Brackbill *et al.* (1992), the delta function is discretized as a smooth function depending on the distance from the interface. However, here, the pressure p is separated into two contributions: one $p_{(st)}$ depending on the surface tension and one $p_{(nst)}$ independent from it. This makes it possible to write two Poisson equations. The first contribution

$$\nabla^2 p_{(st),0}^{n+1/2} = \nabla \cdot \left(2\sigma (\kappa \delta \boldsymbol{n})^{n-1/2} \right) \tag{3.6}$$

results in a pressure jump at the interface due to the surface-tension, and it is completely independent of the density distribution. The second contribution is

$$\nabla \cdot \left(\frac{\nabla (p^{n-1/2} - p_{(nst),0}^{n+1/2})}{\rho^{n-1/2}} \right) = \frac{\nabla \cdot \tilde{\boldsymbol{u}}}{\Delta t} \ . \tag{3.7}$$

The solution of the Poisson equations (3.6) and (3.7) gives $p_0^{n+1/2}$, and $\boldsymbol{u}_0^{n+1}$ follows from the second equation in (3.5). The viscosity and density fields are defined once the interface has been captured by the Level-set technique discussed later. These data are used to start the iterative corrector step.

Corrector step. At the k-th step of the corrector, the term $[F(\boldsymbol{u})]_k^{n+1/2}$ is obtained by a centered Taylor expansion, and the pressure gradient is written as

$$\frac{\nabla p_{(ns),k}^{n+1/2}}{\rho_{k-1}^{n+1/2}} = \frac{\nabla p_{(ns),k-1}^{n+1/2}}{\rho_{k-1}^{n+1/2}} + \frac{\nabla p_c}{\rho_{k-1}^{n+1/2}} \ ,$$

where p_c is a pressure-correction term. The pressure terms are connected to the velocity field through the projection on a divergence free space:

$$\begin{aligned}\tilde{\boldsymbol{u}} &= \boldsymbol{u}^n + \Delta t \left\{ [F(\boldsymbol{u})]_{k-1}^{n+1/2} - \frac{\nabla p_{k-1}^{n+1/2}}{\rho_{k-1}^{n+1/2}} \right\} \\ \boldsymbol{u}_k^{n+1} &= \tilde{\boldsymbol{u}} + \Delta t \left\{ 2\sigma \frac{(\kappa\delta\boldsymbol{n})_{k-1}^{n+1/2}}{\rho_{k-1}^{n+1/2}} - \frac{\nabla p_c}{\rho_{k-1}^{n+1/2}} \right\}\end{aligned}$$

and by solving the Poisson equations

$$\begin{aligned}\nabla^2 p_{(st)k}^{n+1/2} &= \nabla \cdot \left(2\sigma (\kappa\delta\boldsymbol{n})_{k-1}^{n+1/2} \right) \\ \nabla \cdot \left(\frac{\nabla p_c}{\rho_{k-1}^{n+1/2}} \right) &= \frac{\nabla \cdot \tilde{\boldsymbol{u}}}{\Delta t}\end{aligned}$$

As before, once the above Poisson equations have been solved, velocity, density and viscosity fields can be updated according to the position of the new interface. The iterative procedure is repeated until convergence of $p = p_{(st)} + p_{(nst)}$ is satisfied.

A non-iterative scheme, based on the algorithms described in Sussman *et al.* (1994), has been also implemented, but it has been found that the use of even only one corrector step can lead to improvements in accuracy and in stability of the method. For the present calculation a CFL-like (Courant-Friedrichs-Lewy) limit has been used as a stability constraint. In more detail three sources of constraint are involved: one from the level-set advection, one from the Navier-Stokes equations, and one from the surface tension. The three together lead to

$$\Delta t \leq \min \left(0.5 \frac{\Delta x}{|\boldsymbol{u}_{max}|}, 0.25 \frac{Re}{1/\Delta x^2 + 1/\Delta y^2}, 0.5 \sqrt{\frac{\Delta x^3 (\rho_w + \rho_a)}{4\pi\sigma}} \right) .$$

These conditions are very conservative, and the use of an iterative solution makes the stability limits more relaxed; the splitting of the pressure in the terms $p_{(st)}$ and $p_{(nst)}$ is less constraining.

3.2.2 Spatial discretization

For the spatial discretization a staggered grid has been chosen as shown in figure 3.1. The horizontal velocity $u_{i,j}$ is defined at the centre of the vertical side and the vertical velocity $v_{i,j}$ at the centre of the horizontal side of each cell. Pressure and other fluids properties are defined at the centre of the cell. The use of a staggered grid provides better coupling between different variables, and the achievement of a physically correct pressure field.

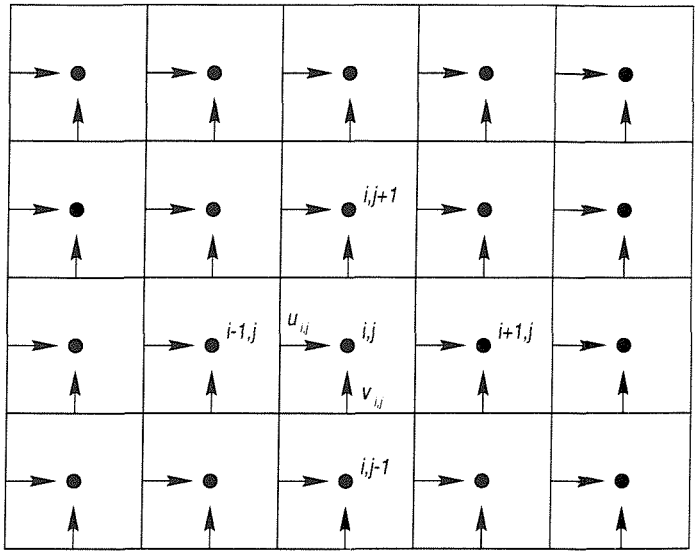

Figure 3.1: Definition of the fluid variables on the staggered grid.

Advection operator

The advective terms in the Navier-Stokes equations

$$u\frac{\partial u_i}{\partial x} + v\frac{\partial u_i}{\partial y} \ , \tag{3.8}$$

are discretized using a non-conservative scheme. For example for the u component of the velocity the advective term becomes

$$u_{i,j}\frac{u_{i+1/2,j} - u_{i-1/2,j}}{\Delta x} + v_{i-1/2,j+1/2}\frac{u_{i,j+1/2} - u_{i,j-1/2}}{\Delta y} \ . \tag{3.9}$$

The choice of a non-conservative scheme makes it impossible to ensure formally the convergence of the scheme to the physical solution according to the Lax-Wendroff theorem (Lax & Wendroff, 1960)[1], but, as it will be shown in the next section, the applications of the scheme to various test cases furnished heuristic proofs of its convergence. Further, it is possible to demonstrate that, assuming a divergence free velocity condition, the advective form $u\partial u/\partial x + v\partial u/\partial y$ of the convective term is equivalent to the divergence $\partial u^2/\partial x + \partial uv/\partial y$ and to the skew symmetric $1/2\partial u^2/\partial x + 1/2\partial uv/\partial y + 1/2u\partial u/\partial x + 1/2v\partial u/\partial y$ representations (Morinishi *et al.*, 1998). In fact, the conservative discrete form for u is

$$\frac{u^2_{i+1/2,j} - u^2_{i+1/2,j}}{\Delta x} + \frac{u_{i,j+1/2}v_{i-1/2,j+1} - u_{i,j-1/2}v_{i-1/2,j}}{\Delta y} \tag{3.10}$$

[1]The validity of the theorem is generally extended to the interfacial flows, since they can be thought similar to shock waves, but this extension has never been demonstrated formally.

which can be written

$$\begin{aligned}&\frac{u_{i+1/2,j}-u_{i+1/2,j}}{\Delta x}(u_{i+1/2,j}+u_{i+1/2,j}) \quad + \\ &+\frac{u_{i,j+1/2}-u_{i,j-1/2}}{\Delta y}\frac{v_{i-1/2,j+1}+v_{i-1/2,j}}{2} \quad + \quad . \\ &+\frac{v_{i-1/2,j+1}-v_{i-1/2,j}}{\Delta y}\frac{u_{i,j+1/2}+u_{i,j-1/2}}{2}\end{aligned} \tag{3.11}$$

Assuming that the discrete velocity is divergence free all over the domain, then the following statement holds

$$\frac{u_{i+1,j}-u_{i,j}}{\Delta x}+\frac{v_{i,j+1}-v_{i,j}}{\Delta y}=0 \Rightarrow \frac{u_{i+1/2,j}-u_{i-1/2,j}}{\Delta x}+\frac{v_{i+1/2,j+1}-v_{i-1/2,j}}{\Delta y}\simeq 0 \tag{3.12}$$

Similarly, in the framework of a second order approximation, $u_{i,j}$ can be approximated by $(u_{i+1/2,j}+u_{i-1/2,j})/2$, $u_{i,j}$ by $(u_{i,j+1/2}+u_{i,j-1/2})/2$ and $v_{i-1/2,j+1/2}$ by $(v_{i-1/2,j}+v_{i-1/2,j+1})/2$, substituting these expressions in 3.11, together with equation 3.12, this gives the non-conservative form of equation 3.8. This demonstrates that the conservative and non-conservative forms are equivalent in the second order approximation for a regular mesh.

Discretizing the generic advection equation $u_t + au_x = 0$, it can be shown that central differences are unstable (Hirsh, 1988), so upwind derivatives are substituted for them. Upwind derivatives of order higher than one develop oscillations (Engqyust & Osher, 1981). In attempting to avoid these oscillations, second order ENO (Essentially Non Oscillatory) schemes are used (Shu & Osher, 1991). Practically, these are a high order upwind schemes with a damping term. The artificial damping term is introduced in the form of a limiter to the flux across the cell sides (Harten, 1983) by the Total Variation Diminishing (TVD) schemes or as a limiter on the slope of the flux by the ENO schemes (Harten & Osher, 1987).

Even though it is computationally more complex, the latter definition of damping preserves the order of accuracy of the scheme even in the extreme points of the advected function, so it is the one most commonly used in numerical codes. Detailed descriptions of the ENO schemes can be found in Harten & Osher (1987), Shu & Osher (1991) and Barth & Deconinck (1999).

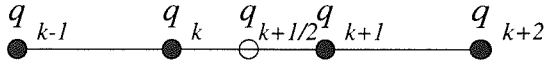

Figure 3.2: Definition of auxiliary variables for advection problems.

To simplify the description, the ENO procedure is outlined here for a 1D case. Extending it to multidimensional problems is straightforward. Assume that the

variable q is known at the grid locations $k-1$, k and $k+1$. To calculate the quantity $q_{k+1/2}$ at the intermediate position (see figure 3.2) the following approximations are defined

$$q_L = q_k + \frac{1}{2}\text{limiter}(q_{k+1} - q_k, q_k - q_{k-1})$$

$$q_R = q_{k+1} - \frac{1}{2}\text{limiter}(q_{k+2} - q_{k+1}, q_{k+1} - q_k)$$

$$q_M = \frac{1}{2}(q_L + q_R) \ .$$

and $q_{k+1/2}$ is chosen according to the advection velocity w as

$$q_{k+1/2} = \begin{cases} q_M & \text{if } |w_{k+1/2}| \leq \Delta x^4 \\ q_R & \text{if } w_{k+1/2} < -\Delta x^4 \\ q_L & \text{if } w_{k+1/2} > \Delta x^4 \ . \end{cases} \tag{3.13}$$

When the variable q coincides with the advection velocity as in the first term of equation 3.8, then its value in an intermediate value of the cell side is given by

$$u_{i+1/2,j} = \begin{cases} u_M & \text{if } u_L \leq 0 \text{ and } u_R \geq 0 \\ u_R & \text{if } u_M \leq 0 \text{ and } u_R \leq 0 \\ u_L & \text{if } u_M \geq 0 \text{ and } u_L \geq 0 \ . \end{cases}$$

Different functions can be used as limiter function $limiter(a, b)$. Here two kinds of limiter functions have been tested: minmod and superbee. The former is defined as

$$\text{limiter}(a, b) = \begin{cases} a & \text{if } |a| \leq |b| \text{ and } ab \geq 0 \\ b & \text{if } |b| \leq |a| \text{ and } ab \geq 0 \\ 0 & \text{otherwise .} \end{cases}$$

The minmod is one of the most commonly used limiters and it is known to be dissipative. This feature is usually accepted because it smooths high normal gradients of the tangential velocity, and further stabilizes the interface with a

numerical viscosity. The superbee limiter is defined as

$$\text{limiter}(a,b) = \begin{cases} \max(\min(|a|, 2|b|), \min(2|a|, |b|))\text{sign}(a) & \text{if } ab \geq 0 \\ \\ 0 & \text{otherwise .} \end{cases}$$

The superbee is the most suitable limiter to capture the advection of a steep function.

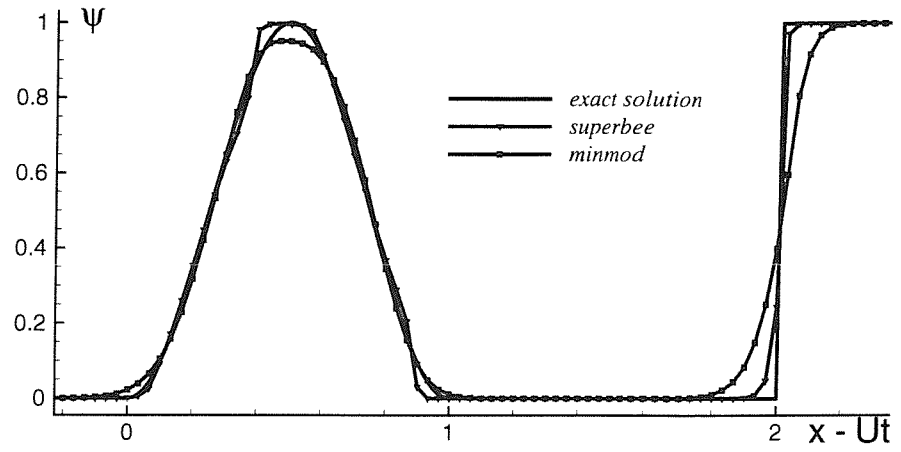

Figure 3.3: Example of advection of a sinusoidal wave followed by a step. The results obtained using the superbee and the minmod schemes are compared with analytical solution.

Figure 3.3 shows the effects of the two different limiters in the advection of a function composed of a single sinusoidal wave and a step:

$$\psi(x,0) = \begin{cases} 0 & \text{if } x < 0 \\ 1/2(\sin(2\pi x) + 1) & \text{if } 0 < x < 1 \\ 0 & \text{if } 1 < x < 2 \\ 1 & \text{if } x > 2 \end{cases}$$

The advection velocity is constant so that this composite wave is simply translated (the exact solution is indicated with a solid line). The minmod limiter (dashed line) keeps the topology of the sinusoidal wave but smooths the step. The superbee limiter (dotted line) sharpens the sinusoidal wave, but correctly advects the steps.

In the case of interfacial flows, the tangential velocity at the interface is characterized by large gradients and therefore behaves similarly to the steps. On the other hand deep inside each fluid the velocity is more likely to assume smooth gradients more closely resembling the sinusoidal wave. This means that the

minmod is more suitable far from the interface, while the superbee is very effective near the interface.

The minmod and the superbee limiters have been preferred to other limiters because of their individual features and because of the possibility of combining them in a smooth transition from one to another. This can be done by introducing a limiter function $m(a, b)$ with variable coefficients.

Assuming that $\phi(x, y, t)$ is the distance of point $\boldsymbol{P}(x, y)$ from the interface at the time t, the limiter is defined as:

$$limiter(a,b) = \begin{cases} 0 & \text{if } ab < 0 \\ \\ \max(\min(f|a|, |b|), \min(f|b|, |a|))\text{sign}(a) & \text{if } ab \geq 0 \end{cases}$$

where the coefficient f is used to model the smooth transition from one limiter function to the other. It depends on the distance ϕ from the interface in the form

$$f = \begin{cases} \frac{1}{2}\cos\left(\frac{\phi\pi}{\delta_{lim}}\right) + 1 & \text{if } |\phi| < \delta_{lim} \\ 1 & \text{if } |\phi| > \delta_{lim} \end{cases}$$

within the interval $[-\delta_{lim}, \delta_{lim}]$. The practical choice of δ_{lim} will be discussed later.

When $|\phi| > \delta_{lim}$, the new limiter represents the minmod limiter and when $\phi = 0$ it corresponds to the superbee.

This formulation is valid for sufficiently high Reynolds numbers. In fact, in the case of sufficiently large fluid viscosity, the true tangential velocity at the interface is quite smooth and the use of a superbee scheme would steepen it unphysically.

Projection operator

The Poisson equations (3.6) and (3.7) can be discretized with a second order scheme with a 5-point stencil or with a 9-point stencil method if the grid has square cells.

In the former case the discretized form is

$$\nabla\left(\frac{1}{\rho}\nabla\phi\right)_{i,j} = \frac{\dfrac{\phi_{i+1,j}-\phi_{i,j}}{\rho_{i+1/2,j}} - \dfrac{\phi_{i,j}-\phi_{i-1,j}}{\rho_{i-1/2,j}}}{\Delta x^2} + \frac{\dfrac{\phi_{i,j+1}-\phi_{i,j}}{\rho_{i,j+1/2}} - \dfrac{\phi_{i,j}-\phi_{i,j-1}}{\rho_{i,j-1/2}}}{\Delta y^2},$$

in the latter

$$\nabla\left(\frac{1}{\rho}\nabla\phi\right)_{i,j} =$$

$$= \frac{2}{3}\left(\frac{\frac{\phi_{i+1,j}-\phi_{i,j}}{\rho_{i+1/2,j}} - \frac{\phi_{i,j}-\phi_{i-1,j}}{\rho_{i-1/2,j}}}{\Delta x^2} + \frac{\frac{\phi_{i,j+1}-\phi_{i,j}}{\rho_{i,j+1/2}} - \frac{\phi_{i,j}-\phi_{i,j-1}}{\rho_{i,j-1/2}}}{\Delta y^2}\right)$$

$$+ \frac{1}{6}\left(\frac{\frac{\phi_{i+1,j+1}-\phi_{i,j}}{\rho_{i+1/2,j+1/2}} - \frac{\phi_{i,j}-\phi_{i-1,j-1}}{\rho_{i-1/2,j-1/2}}}{\Delta x^2} + \frac{\frac{\phi_{i-1,j+1}-\phi_{i,j}}{\rho_{i-1/2,j+1/2}} - \frac{\phi_{i,j}-\phi_{i+1,j-1}}{\rho_{i+1/2,j-1/2}}}{\Delta y^2}\right) .$$

The second term in the right hand side of the 9-point stencil method is obtained by applying the differential operators along the cell diagonals. Where it is possible, the latter discretization is preferred since it leads to a Laplacian operator that is less dependent on the directions chosen for the spatial discretization.

To solve the linear systems of equations 3.6 and 3.7, different methods can be used. Here a Generalized Minimum RESidual (GMRES) method has been adopted (Otto, 1996).

3.2.3 Smoothing across the interface

The coefficients of the limiter function do not represent the only quantities smoothed across the interface. In fact, not only the advective operator but also the density ρ, the viscosity μ, the delta function δ need to be smoothed. In particular, the solution of the Poisson equation for $p_{(nst)}$ requires the density to be smoothed across the interface to avoid (possibly divergent) numerical oscillations.

The use of a level-set function requires the introduction of an analytical link between the distance function and the properties of density and viscosity. No rule exits for the choice of such a function, but the requirements are mass conservation and convergence of the numerical representation to the physical solution as $\Delta x \to 0$.

Usually e.g. (Sussman *et al.*, 1994), the density is defined by a trigonometric bridge function, but this representation presents a poor stability. The compound $1/\rho$ function, as it appears in the equations, is steeper on the air side, shifting in that direction most of the transition from the water to the air fields (see figure 3.4).

A possible solution to this problem could be achieved by a trigonometric smoothing of the inverse of the density, appearing as coefficients of the Poisson equation. However, the pressure p, the solution of this equation, is related to the density as well. Therefore, if ρ is not adequately smoothed, its derivative, which appears in the calculation of the pressure derivatives near the interface, would probably introduce oscillations and eventually instabilities.

To reduce the risk of oscillations both in the discretization of the Poisson equation and in the calculation of the pressure derivatives, a similar smoothing of the density and of its inverse is necessary. For this pourpose, in the present implementation, an exponential bridge function has been introduced in the form

$$\rho(\phi) = \begin{cases} \rho_w & \text{if } (\phi - \delta_\rho c) < -\delta_\rho \\ \sqrt{\rho_w \rho_a} e^{\frac{1}{2}\log\frac{\rho_w}{\rho_a}\sin\frac{\pi}{2\delta_\rho}(\phi-\delta_\rho c)} & \text{if } |\phi - \delta_\rho c| < \delta_\rho \\ \rho_a & \text{if } (\phi - \delta_\rho c) > \delta_\rho \end{cases} \tag{3.14}$$

where ρ_w and ρ_a are respectively water and air density and the constant coefficient c is chosen to conserve the total mass according to

$$\int_{\delta_\rho(-1+c)}^{\delta_\rho(1+c)} \rho d\phi = \rho_w \delta_\rho (1-c) + \rho_a \delta_\rho (1+c) \ . \tag{3.15}$$

In practice, $c \simeq 0.5521$ for $\rho_{water}/\rho_{air} = 1000/1.23$. The use of the equation (3.14) results in the smoothing of the density and of its inverse shown in with a dashed line in figure 3.4. The difference between using the bridge function (3.14) and the trigonometric bridge function as usually adopted becomes important in the resolution of local flow details, where the mesh can be relatively coarse and the solution is more sensitive to the extension of the smoothing region.

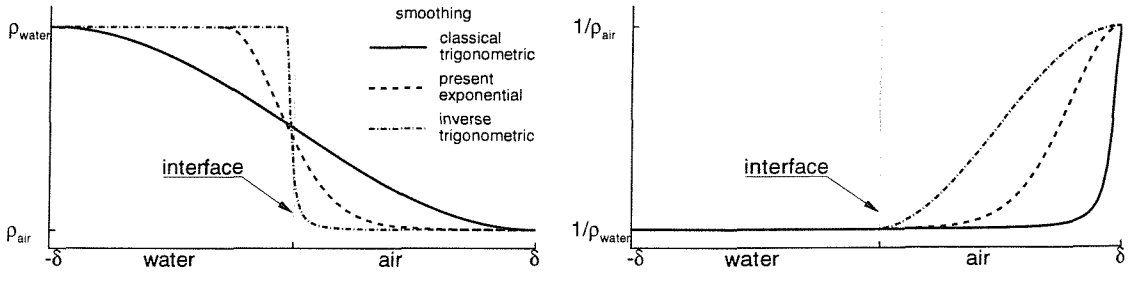

Figure 3.4: Smoothing of the density and of its inverse.

As in the case of the density term, it can be shown that, for a proper solution of the conservation equations, the inverse of the viscosity has to be smoothed

across the interface, rather than the viscosity itself. Smoothing $1/\mu$ rather than μ has been found crucial when an accurate resolution of the air-flow dynamics is needed (Tryggvason *et al.*, 2001). Here,

$$\frac{1}{\mu}(\phi) = \begin{cases} \mu_w^{-1} & \text{if } \phi < -\delta_\mu \\ \frac{\mu_w^{-1}-\mu_a^{-1}}{2}\left(\frac{\sin\left(\frac{\pi\phi}{\delta_\mu}\right)}{\pi} - \frac{\phi}{\delta_\mu}\right) + \frac{\mu_w^{-1}+\mu_a^{-1}}{2} & \text{if } |\phi| < \delta_\mu \\ \mu_a^{-1} & \text{if } \phi > \delta_\mu \end{cases}$$

has been used.

Finally, the Dirac function in the surface-tension term is smoothed as

$$\delta(\phi) = \begin{cases} 0 & \text{if } |\phi| \leq \delta_{st} \\ \frac{1}{2\delta_{st}}\left(\cos\left(\frac{\pi\phi}{\delta_{st}}\right) - 1\right) & \text{if } |\phi| < \delta_{st} \ . \end{cases}$$

similarly to what has been done in Brackbill *et al.* (1992).

In the present implementation, the amplitudes of the four smoothing intervals δ_{lim}, δ_ρ, δ_μ and δ_{st} are fixed throughout the computations and satisfy the conditions

$$\delta_{lim} \geq \delta_\rho = \delta_\mu > \delta_{st} \ .$$

The amplitude δ_{lim} of the variable-coefficient limiter function should be larger than δ_ρ to maintain accuracy in the solution of the advection term in the transition region. Usually, $\delta_{st} \geq 0.7\Delta x$ is sufficient to prevent oscillations in the solution of the corresponding Poisson equations. Such oscillations would induce unphysical parasitic currents in both air and water phases, though larger ones in air because of the density ratio. If $\delta_\rho > \delta_{st}$ the gradients of $p_{(st)}$ decrease more rapidly, reducing the presence of unphysical currents on the air side.

3.3 Interface capturing

The interface between the fluids is traced using the level set function ϕ, introduced for the first time for incompressible fluids in Sussman *et al.* (1994). The level set function is a Lipschitz continuous function that represents the distance from the interface. A complete description of the level set function can be found in Sethian (1999).

At any point P of the domain, the function ϕ (see sketch in figure 3.5) is

defined as

$$\begin{cases} \phi(P) < 0 & \text{if P is in water} \\ \phi(P) > 0 & \text{if P is in air} \\ \phi(P) = 0 & \text{if P is on the interface .} \end{cases}$$

Since a bridge function links the density to the distance from the interface,

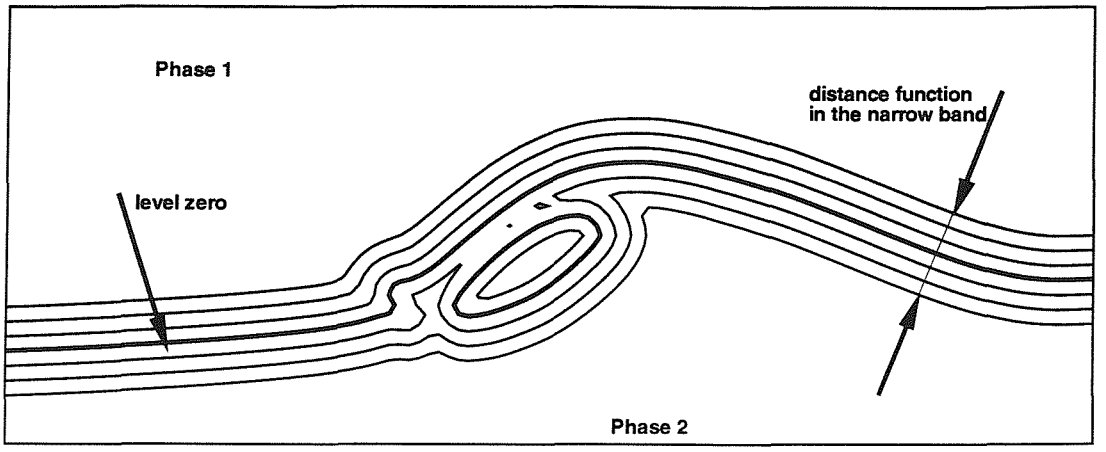

Figure 3.5: Definition of a distance function ϕ in a narrow band around the interface represented by the zero level.

$\rho = \rho(\phi)$, and the continuity equation can be written as

$$\frac{\partial \rho}{\partial \phi}\left(\frac{\partial \phi}{\partial t} + \boldsymbol{u} \cdot \nabla \phi\right) = 0 \,, \tag{3.16}$$

which provides the transport equation for the level-set function as far as $\partial\rho/\partial\phi \neq 0$[2].

The distance function defines not only the position of the interface but it offers also the possibility of an easy calculation of the normal

$$\boldsymbol{n} = \frac{\nabla \phi}{|\nabla \phi|}$$

and of the curvature as

$$\kappa = \nabla \cdot \frac{\nabla \phi}{|\nabla \phi|}$$

[2]As explained later, knowledge of the position of the zero level is a necessary and sufficient requirement for defining the level set function all over the domain. At the interface ($\phi = 0$) $\partial\rho/\partial\phi \neq 0$.

along the interface

The Lagrangian evolution of ϕ through equation 3.16 does not preserve the meaning of distance from the interface. Therefore a reinitialization procedure of ϕ is necessary to restore its geometrical properties. In the reinitialization, as introduced in Sethian (1999), ϕ is advanced in a pseudo-time τ until the solution of the equation

$$\frac{\partial \phi}{\partial \tau} + \left(\frac{\nabla \phi \cdot \nabla \phi}{|\nabla \phi|} - 1 \right) \text{sign}(\phi) = 0 \tag{3.17}$$

has reached stationary convergence, thus the geometric property of a distance function $|\nabla \phi| = 1$ is intrinsically enforced. In equation (3.17) $\text{sign}(\phi)$ represents a smooth approximation of the sign of ϕ and it is defined as $\phi / \sqrt{\phi^2 + \epsilon^2}$, where ϵ is a small smoothing parameter that can be assumed equal to the minimum grid size. This function is necessary to enforce the physical propagation of the signal from the interface to the outer regions.

Usually, equation (3.17) is solved through a second order ENO scheme with the minmod limiter. Theoretically the reinitialised distance function ϕ should have the same zero as the advected function. In Russo & Smereka (2000) a basic error in

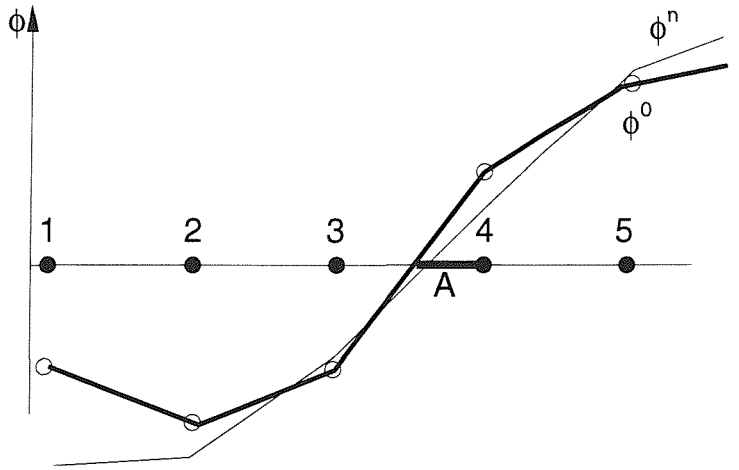

Figure 3.6: Example of reinitialization of the level-set function in the 1D case. The classical reinitialization of the level set causes the shift of the zero level. The initial function ϕ_0 has a zero different from the one of the reinitilized function ϕ.

the use of the ENO scheme has been highlighted.

For example, applying a first order ENO scheme to the 1D case in figure 3.6,

the discrete form of equation (3.17) at point 4 reads

$$\phi_4^{n+1} = \phi_4^n - \text{sign}(\phi_4)\text{sign}\left(\frac{\partial \phi_4}{\partial x}\right)\left(\frac{\partial \phi_4}{\partial x} - 1\right)\Delta\tau \tag{3.18}$$

where the advecting velocity is $\text{sign}(\phi_4)\text{sign}(\frac{\partial \phi_4}{\partial x})$. Given that the two first order derivatives

$$a = (\phi_4 - \phi_3)/\Delta x \quad \text{and} \quad b = (\phi_5 - \phi_4)/\Delta x$$

are, like ϕ_4 both positive, the upwind scheme reads

$$\phi_4^{n+1} = \phi_4^n + \left(\frac{|\phi_4^n - \phi_3^n|}{\Delta x} - 1\right)\Delta t \ . \tag{3.19}$$

Formula (3.19) contains the left derivative of point 4, so it violates the assumption that the information moves to the reinitialized point from the interface and not from beyond it.

In Russo & Smereka (2000) this problem is solved by using geometrical considerations. If $\partial\phi/\partial x = 1$, then ϕ_4 is equal to the length of a segment A marked with a thicker line in figure 3.6. A second order centred derivative at point 4 gives $(\phi_5 - \phi_3)/2\Delta x$, and a line with this slope, passing through the point (x_4, ϕ_4), intersects the zero axis at $x = x_4 - 2\Delta x\phi_4^0/|\phi_5 - \phi_3|$. Assuming that this point is the zero level, the reinitialization procedure is corrected as

$$\phi_i^{l+1} = \begin{cases} \phi_i^l - \Delta\tau\left(\text{sign}(\phi_i^0)|\phi_i^l| - \frac{\phi_i^0}{|\phi_{i+1}^0 - \phi_{i-1}^0|}\right) & \text{for an interface cell} \\ \phi_i^l - \Delta\tau\text{sign}(\phi_i^0)\left(\text{sign}\left(\frac{\partial \phi_i^l}{\partial x}\right)\frac{\partial \phi_i^l}{\partial x} - 1\right) & \text{otherwise.} \end{cases} \tag{3.20}$$

The corresponding correction in the 2D case reads

$$\phi_{i,j}^{l+1} = \begin{cases} \phi_{i,j}^l - \Delta\tau\left(\text{sign}(\phi_{i,j}^0)|\phi_{i,j}^l| - C_{i,j}\right) & \text{for an interface cell} \\ \phi_{i,j}^l - \Delta\tau\text{sign}(\phi_{i,j}^0)\left(\frac{\nabla\phi_{i,j}^l \nabla\phi_{i,j}^l}{|\nabla\phi_{i,j}^l|} - 1\right) & \text{otherwise} \end{cases} \tag{3.21}$$

where

$$C_{i,j} = \frac{\phi_{i,j}^0}{\sqrt{\left(\frac{\partial \phi_{i,j}^0}{\partial x}\right)^2 + \left(\frac{\partial \phi_{i,j}^0}{\partial y}\right)^2}} \ . \tag{3.22}$$

This correction does lead to a better accuracy of the method, yet some numerical smoothing is observed in cases with high curvature of the interface, including in the limit a discontinuous interface where the normal is not uniquely defined (see figure 3.7). For such cases, a more accurate solution can be obtained by rewriting the modulus of the gradient as:

$$|\nabla\phi| = \sqrt{\nabla\phi\cdot\nabla\phi} = \sqrt{\nabla(\phi\nabla\phi) - \phi\nabla^2\phi} = \sqrt{\nabla^2\left(\frac{\phi^2}{2}\right) - \phi\nabla^2\phi}\ .$$

This formulation takes into account the curvature of the interface and manages to reduce the numerical error committed when calculating the normal at discontinuities. So a more accurate solution can be obtained by using

$$\begin{aligned} C^m_{i,j} &= \frac{\phi^0_{i,j}}{\sqrt{A+B}} \\ A &= \frac{\phi^0_{i+1,j}\left(\frac{\phi^0_{i+1,j}}{2} - \phi^0_{i,j}\right) + (\phi^0_{i,j})^2 + \phi^0_{i-1,j}\left(\frac{\phi^0_{i-1,j}}{2} - \phi^0_{i,j}\right)}{\Delta x^2} \\ B &= \frac{\phi^0_{i,j+1}\left(\frac{\phi^0_{i,j+1}}{2} - \phi^0_{i,j}\right) + (\phi^0_{i,j})^2 + \phi^0_{i,j-1}\left(\frac{\phi^0_{i,j-1}}{2} - \phi^0_{i,j}\right)}{\Delta y^2}\ . \end{aligned} \tag{3.23}$$

This formula has an important drawback, it does not smooth the oscillations at the interface and results in a poorer stability. Therefore, in the final implementation, at the interface a weighted combination of the two methods (3.22-3.23) has been adopted, that is

$$\phi^{l+1}_{i,j} = \phi^n_{i,j} - \Delta\tau((\mathrm{sign}(\phi^0_{i,j})|\phi^l_{i,j}| - (a_{rs}C_{i,j} + a_m C^m_{i,j}))\ . \tag{3.24}$$

A suitable balance between an accurate solution and the avoidance of oscillations on the interface results in the choice of $a_{rs} = 0.8$ and $a_m = 0.2$.

As the calculation of the distance function is time consuming it is exactly defined in a narrow band 2α wide around the interface. Outside this region the distance function is kept constant and equal to $\pm\alpha$, where the sign is chosen according to the position of the point in one or the other fluid (see figure 3.5).

The width of this band α can be arbitrarily chosen as long as it is outside the range $[-\delta_p + \delta_{\rho_w,\rho_a}, \delta_p + \delta_{\rho_w,\rho_a}]$, And α must be larger than $\delta_p + \delta_{\rho_w,\rho_a}$, where density and viscosity vary.

A sharp cut-off of the distance function in the reinitialization step could introduce dangerous oscillations at the boundaries of the narrow band. Following Peng *et al.* (1999), a smoothed cut off function $c(\phi)$ is used between $[-\alpha, -\delta]$ and

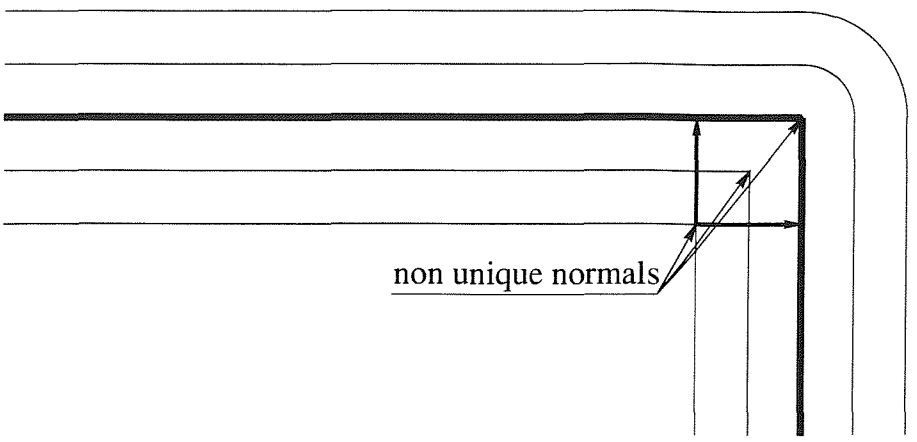

Figure 3.7: Points where the normal vector is not uniquely defined.

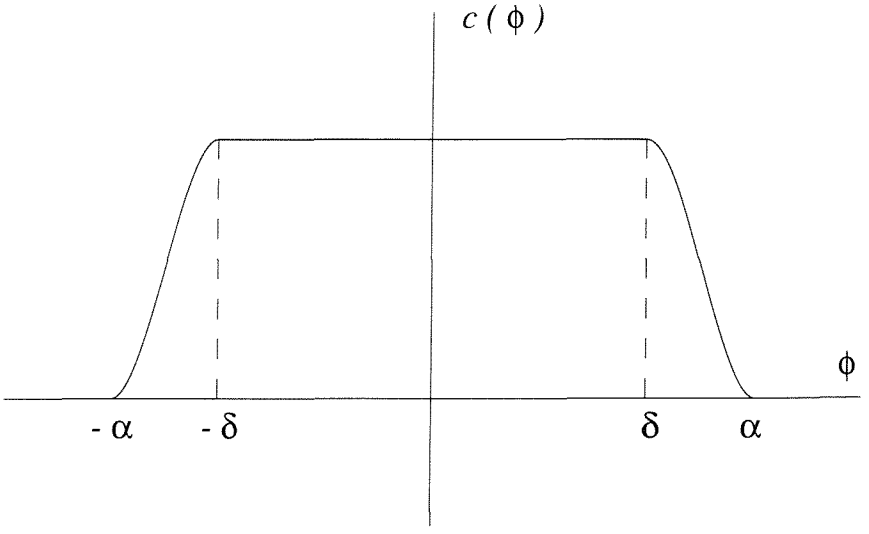

Figure 3.8: Cut off function (Peng *et al.*, 1999).

$[\delta, \alpha]$, in the form

$$c(\phi) = \begin{cases} 1 & \text{if} \quad |\phi| \leq \delta \\ \dfrac{(|\phi| - \alpha)^2(2|\phi| + \alpha - 3\delta)}{(\alpha - \delta)^3} & \text{if} \quad \delta \leq |\phi| \leq \alpha \\ 0 & \text{if} \quad |\phi| \geq \alpha \end{cases}$$

where $\delta \leq \delta_p + \delta_{\rho_w, \rho_a}$ (see figure 3.8).

In this way, far from the interface, equation (3.21) becomes

$$\phi_{i,j}^{l+1} = \phi_{i,j}^{l} - c(\phi)\Delta\tau \mathrm{sign}(\phi_{i,j}^{0}) \left(\frac{\nabla\phi_{i,j}^{l} \nabla\phi_{i,j}^{l}}{|\nabla\phi_{i,j}^{l}|} - 1 \right)$$

and the diffusion velocity of the distance function is nullified outside the narrow band. Finally, oscillations are smoothed out enforcing $|\phi| = |\alpha|$ at the mesh point where actually the inequality $|\phi| > |\alpha|$ would apply.

In all the cases treated in this thesis the solid boundaries will be considered coincident with a side of the cell, while the distance function is defined at its centre. This strategy bypasses all the problems linked with the boundary conditions at the contact point between the free surface and solid walls.

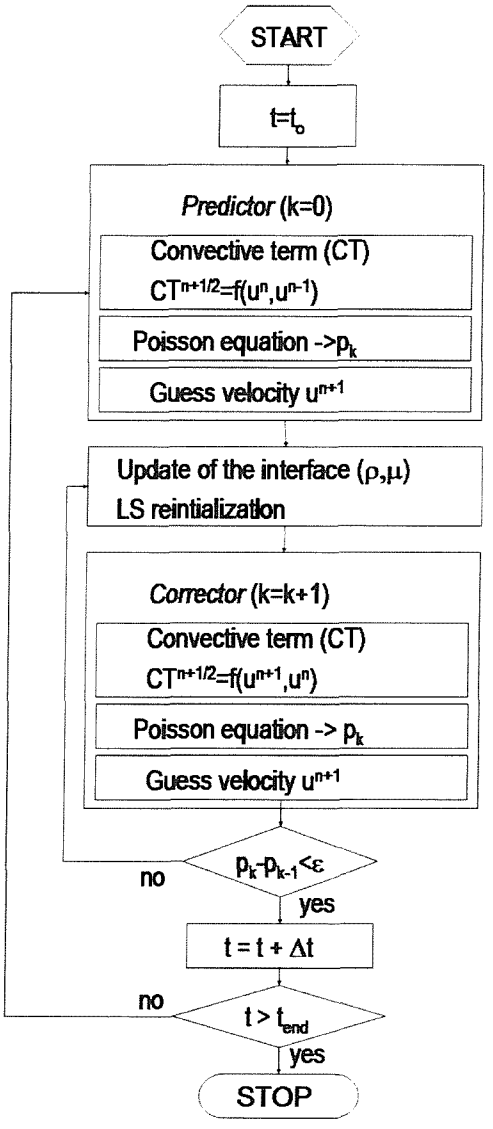

Figure 3.9: Flow diagram of the numerical scheme used here.

3.4 Conclusions

The numerical scheme outlined in this chapter is briefly summed up in the flow diagram in figure 3.9.

An iterative Predictor-Corrector scheme is used for the time discretization and an approximate projection method is adopted for the solution of the pressure.

Particular attention has been paid to the numerical methods adopted in the neighbourhood of the interface between two fluids. A variable coefficients limiter function in the convective terms prevents velocity diffusing from one fluid to the other. A pressure splitting allows a more robust solution of the surface tension problem. An exponential smoothing function for the density reduces the oscillations deriving from the high gradients in the coefficients of the Poisson equations. A corrected reintialization procedure reduces the smoothing error associated with the level set function.

..., by slow prudence to make mild
a rugged people, and thro' soft degrees
subdue them to the useful and the good.
Ulysses, Alfred Tennyson

Chapter 4

Validation of the numerical solver

Here the numerical solver described in the previous chapter is applied to simple prototype problems. Strong deformation and breaking of the free surface, air entrainment, vorticity interaction with the interface and surface tension phenomena are analyzed individually. Each case demonstrates the validity of the method.

4.1 Introduction

The aim of the numerics developed in this thesis is to simulate efficiently and accurately the deformation of the free surface in cases involving violent motions. To make sure that the results obtained are not only physically reliable but quantitatively accurate, the results of the present algorithm should be compared with experimental data.

The main problem when comparing with experimental data that are available in the literature is the lack of full information on the experimental set up used and a shortage of flow visualization in the breaking region. For this reason a set of dedicated experiments have been performed in well documented conditions to verify the numerical code. The problem chosen is the one of a bluff body moving in water. To avoid additional complexities connected with 3D effects, a 2D flow has been investigated. The problem studied is the flow field around a surface-piercing plate moving in water with known velocity. The geometry of the test is identical to that simulated by Tsai & Yue (1993). This problem preserves the main phenomena connected with the surface piercing body problem: (1) strong

deformation of the interface with eventual breaking and air entrainment, (2) generation of vorticity, and (3) its interaction with the interface. The main features described here are shown in figure 4.1.

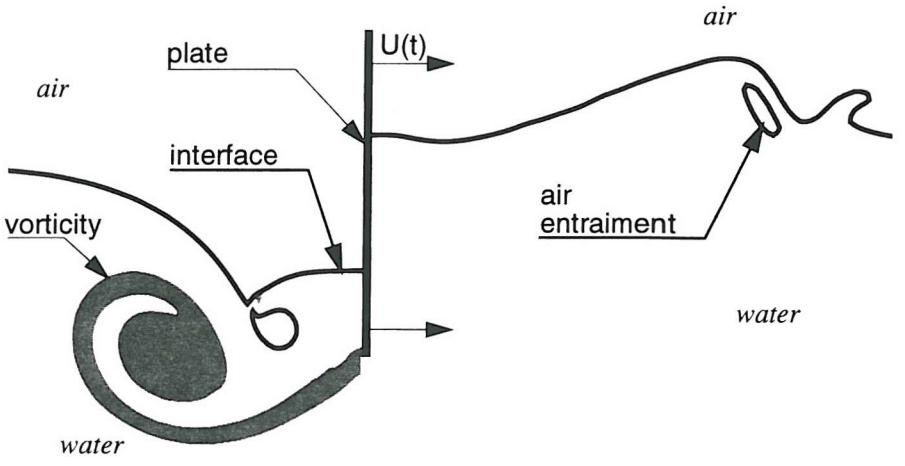

Figure 4.1: Example of flow around a surface piercing plate. The interface between air and water is highly deformed by the motion of the plate with velocity U(t) in water initially at rest. At the lower tip of the plate vorticity detaches (shadowed area), and interacts with the interface.

Before applying the numerical algorithm to this problem which is discussed in the next chapters, the validity of the solver has been tested on simpler problems where each flow feature listed above appears individually. The dam-break *plus* impact problem has been used to analyze breaking at the interface and the air entrainment; the interaction between vorticity and the interface has been investigated in the case of a vortex pair rising toward a free surface, and the modelling of surface-tension effects was studied by considering the evolution of a gas bubble.

The use of simple prototype problems indirectly connected with the more general problem of interest simplifies the problem of understanding the phenomena and the data analysis. If each aspect of the problem is analyzed separately, the detection of numerical errors is simpler.

The problems listed above have stimulated and informed the development of the numerical code described in the previous chapter. Moreover the comparison with benchmark studies represent a part of the verification of the solver. Its convergence is analyzed in appendix A.

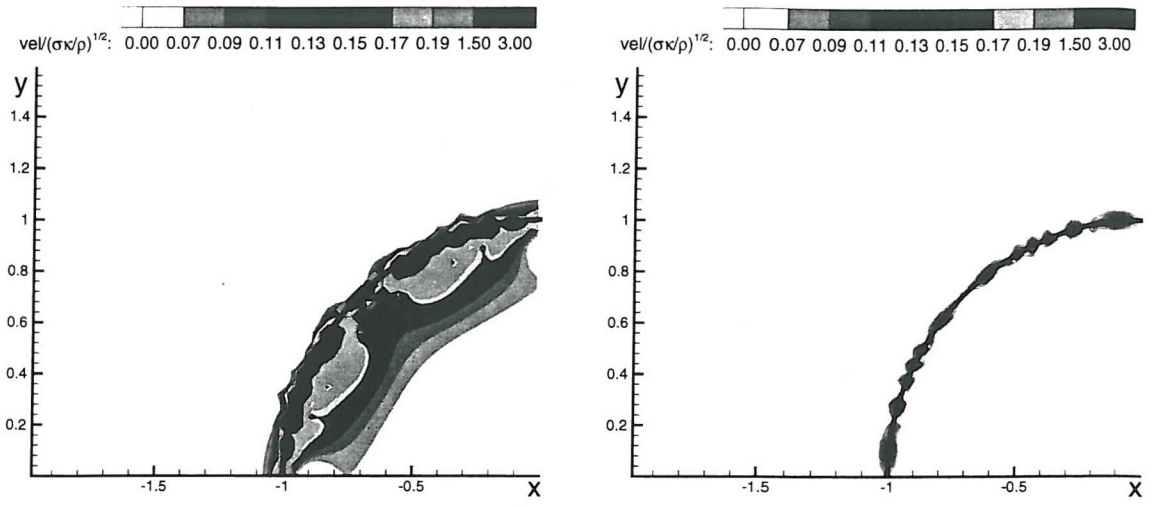

Figure 4.2: Parasitic currents for different numerical solvers. The thick line represents the surface of the bubble. Left: classical solver (Brackbill *et al.*,1992); right: present solver. $\Delta x = R/33$, $t = \Delta t = R/(2\sqrt{\sigma\kappa/\rho})$, $\delta_{st} = \delta_\rho/2 = 0.4\Delta x$

4.2 The rising bubble problem

The problem of the rising bubble has been used to study the effects of surface tension. The numerical modelling of the surface tension adopted here is very similar to the one proposed by Brackbill *et al.* (1992) except for the splitting of the pressure term into two contributions, one due to the surface tension and the other to the remaining forces acting in the Navier-Stokes equations. This implies the solution of two Poisson equations, with the pressure term due to the surface tension independent from the density. To understand the numerical difference between the pressure splitting implemented here and the classical solver used by Brackbill *et al.* (1992), the analytical solution of a flow field around a cylindrical bubble at zero gravity has been analyzed. The exact solution to this problem is zero velocity everywhere and a pressure jump proportional to the surface tension at the air-water interface. The numerical solution of the discrete Poisson equation implies numerical errors and, consequently, some parasitic currents (Liu *et al.*, 2000). The intensity of these currents is shown in figure 4.2 for the classical solver by Brackbill *et al.* (1992) on the left and by the present technique on the right. Using the same mesh and the same time-stepping, the intensity of the parasitic currents obtained with the method described in section 3.2.1 results ten times smaller than one obtained with the classical technique.

The accuracy of the solver for the surface tension has been tested by comparing

the numerical results to the experimental results of Walters & Davidson (1962) for the case of a rising cylindrical bubble. A two dimensional air bubble is formed in a water tank 3/8 inches wide. It is released impulsively by withdrawing an 1 inch diameter tube from the tank.

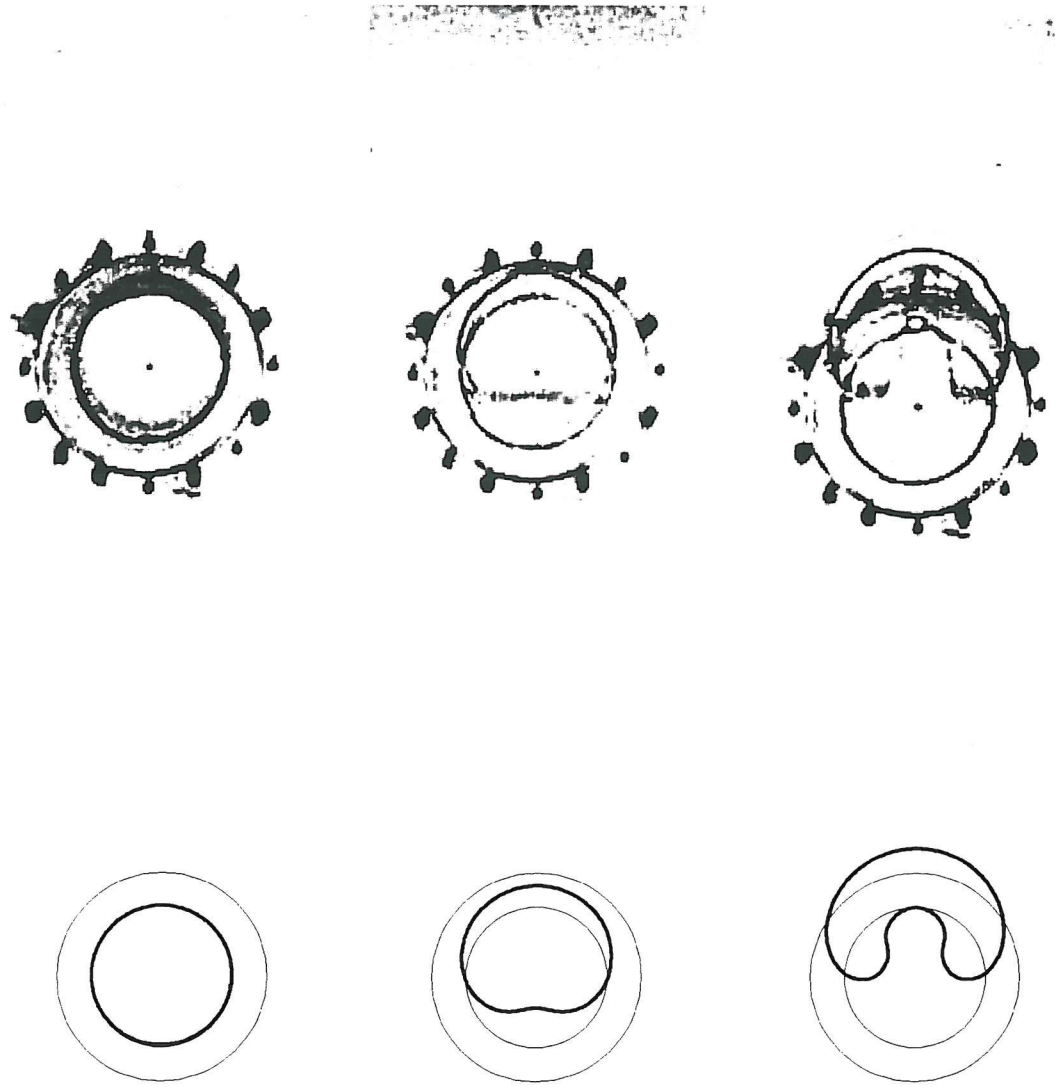

Figure 4.3: Initially circular 2D air bubble (with radius R=1inch) in water. The top figures are extracted from the experiments presented in Walter & Davidson, (1962). The lower figures are the numerical results. Time increases from left to right; the plots refer to t=0.0125s, 0.0625s, 0.1125s

The top plots of figures 4.3 and 4.4 show the experimental evolution of an air bubble immersed in water. Because of its buoyancy the bubble rises. While moving upwards into the water the rise time is strongly influenced by added mass

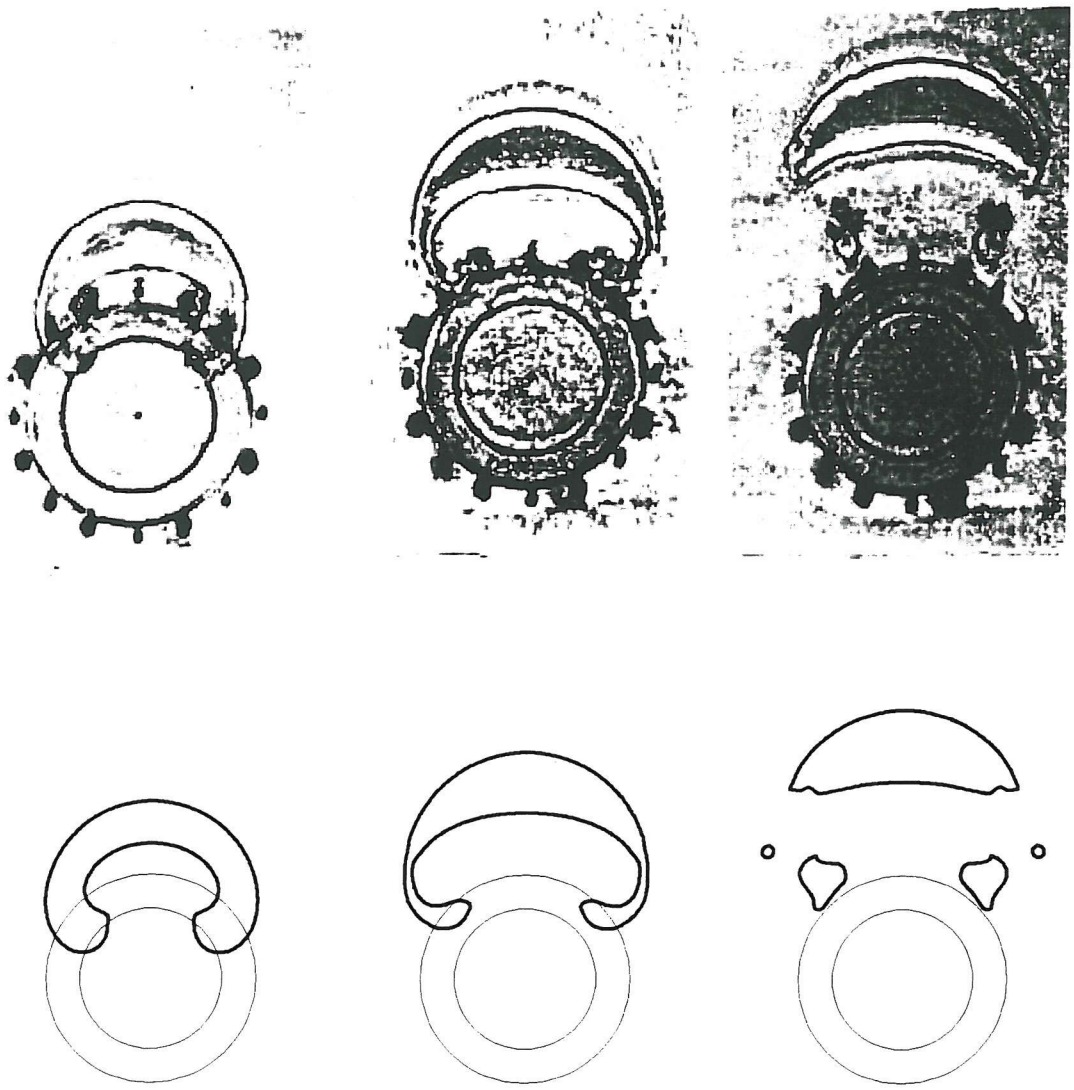

Figure 4.4: Same conditions of figure 4.3. t=0.1625s, 0.2125s, 0.2625s

effects; the top of the bubble moves with a lower velocity respect to the bottom, so the bubble is compressed along its vertical axis. Later on, both viscosity and surface tension contribute to preserve the cylindrical bubble form. Here the attention is focused on the effects of the surface tension. If it is small the curvature of the bubble can reduce and eventually change its sign at the bottom part. In figures 4.3 and 4.4 the present results for the evolution of the air-water interface are given in the bottom plots at the same time instants as the corresponding experimental results. The agreement between experiments and numerics is rather satisfactory up to the time instant when the central jet impacts on the lateral walls of the bubble at $t = 0.22s$. Small detectable differences can be explained by the

meniscus effects on the glass that alter the image perceived at the side of the glass. Another cause of differences can be due to the initial conditions. The tube with the air inside is withdrawn in a finite time and this can influence the initial shape of the bubble. After the internal tongue of water merges with the wall of the bubble, the differences could be due to numerical errors or to differences between the initial conditions used in the test and in the numerical simulation. For example, the nature of the gas inside the physical bubble and its pressure is not declared by Walters & Davidson (1962). The problem they proposed is characterized by the following non dimensional numbers:
$Re = g^{1/2}R^{1/2}\rho_w/\mu_w = 1.1 \cdot 10^6$ and $We = We_{exp} = (gR)^2\rho_w/\sigma = 837$.

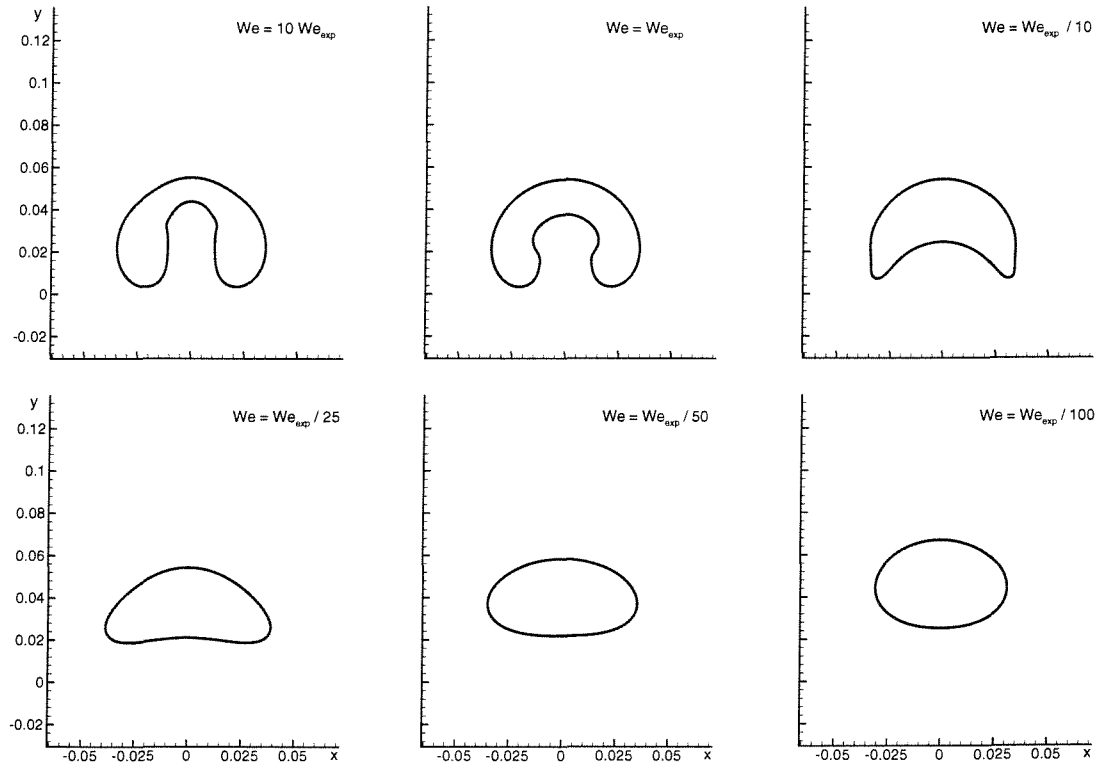

Figure 4.5: Deformation of an initially circular bubble of 1inch diameter at different Weber numbers. The Weber number $We_{exp} = (gR)^2\rho_w/\sigma = 837$ is used in the experiments by Walters & Davidson, (1962). The Reynolds number is constant and equal to $Re = 1.1 \cdot 10^6$. The initial position of the bubble centre is (0.,0.).

The effects of the surface tension are further investigated numerically. The higher the surface tension is, the more restrictive become the related limits on the time step needed to avoid instabilities. The bubbles used in the experiments by

Walters & Davidson (1962) are characterized by a rather large Weber number. To verify the handling of the surface tension by the present solver the Weber number has been varied within a wide range. Figure 4.5 shows the deformation of the free surface at t=0.125s in cases where the Weber number is set equal to $10We_{exp}$, We_{exp}, $We_{exp}/10$, $We_{exp}/25$, $We_{exp}/50$ and $We_{exp}/100$ respectively from left to right and from top to bottom.

As the surface tension increases, the deformation of the bubbles is smaller, so that the deformation of its central part does not cause the splitting of the bubble in smaller bubbles. In this case the corresponding threshold Weber number is equal to 80.

The different profiles of the top part of the bubble, at different Weber numbers, cause also a change of the added mass of the rising bubble. As a result, the bubble rises with different velocities.

All cases shown in figure 4.5 have been performed with a time step $\Delta t = 1 \cdot 10^{-4} s$ that is almost ten times larger than the maximum Δt allowed by the stability constraints in the Brackbill's solution.

4.3 Interaction of a vortex pair with a free surface

The problem of the vortex pair rising toward the free surface has been used to verify the capability of modelling the interaction of the vorticity with the interface. For this problem, the Reynolds number $Re = \Gamma\rho/2\pi\mu$ is defined in term of the circulation and the kinematic viscosity, and the Froude number is defined as $Fn = \Gamma/2\pi(ga^3)^{1/2}$, where a is the initial distance between the vortices. The case of $Re = 100$, $Fn = 0.8$ and infinite Weber number is studied. The flow features that develop are analyzed numerically and compared with those obtained by Ohring & Lugt (1991). Their method, a Lagrangian approach, differs from the one presented here in respect of the discretization of the Navier-Stokes equations. Moreover they do not handle the evolution of the gaseous phase.

Both results are presented in figures 4.6 and 4.7, where the same initial mesh has been used. The agreement is rather good even though some minor differences can be noted at the formation of an anticlockwise vorticity (dashed contour lines) close to the free surface. In this case the present method suffers from the presence of a locally coarser mesh, while the Lagrangian mesh tends naturally to

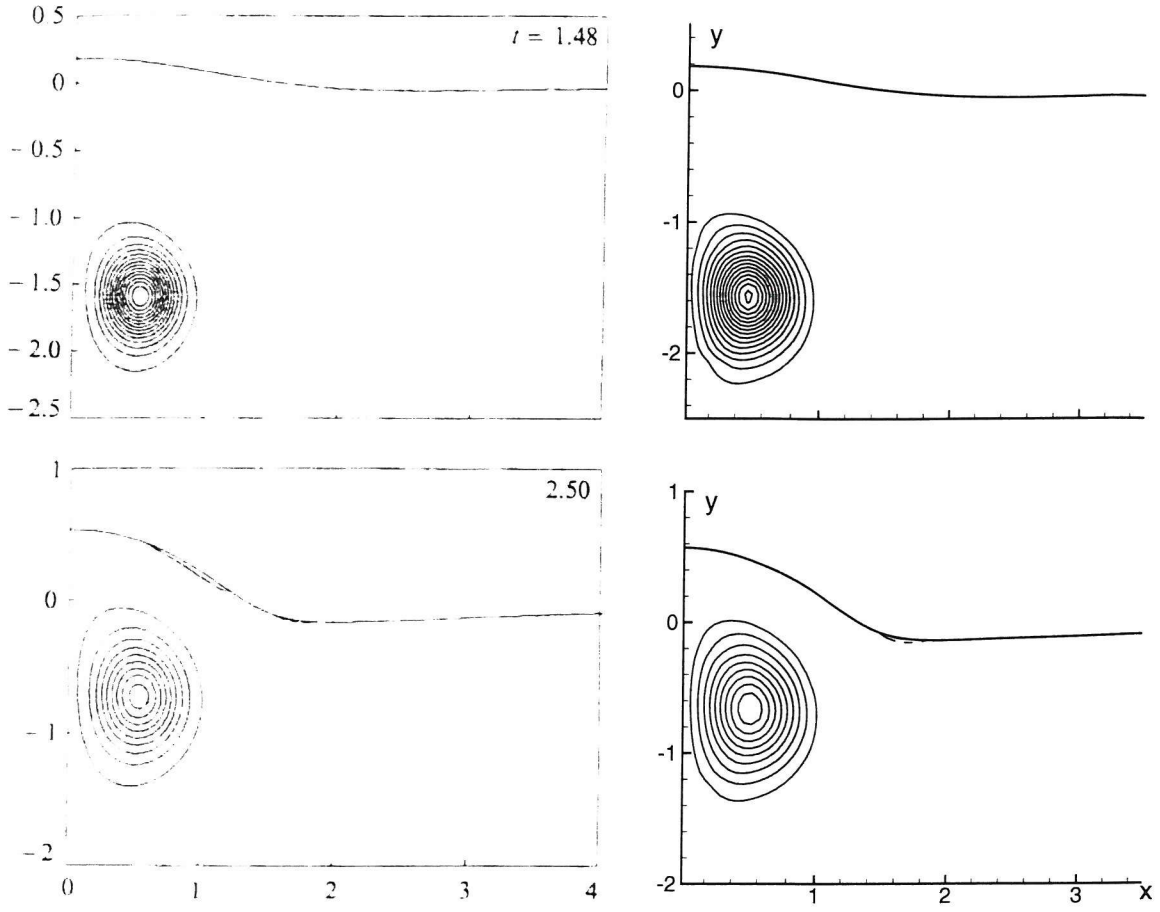

Figure 4.6: Evolution of a vortex pair rising towards the free surface. Left: numerical results from Ohring & Lugt, (1991); right: present results. The continuous contours represent the clockwise rotating vorticity and the dashed contours the anticlockwise rotation. The vorticity contours are spaced by $\Delta\omega = 2$ (for both the computations the $\Delta x = 0.058a$).

concentrate more points in that region. On the other hand, due to this intrinsic feature of the Lagrangian technique, the simulation by Ohring & Lugt (1991) is forced to stop at t=3.45s, while the present calculation can follow the break up of the water surface above the vorticity region, as shown in figure 4.8.

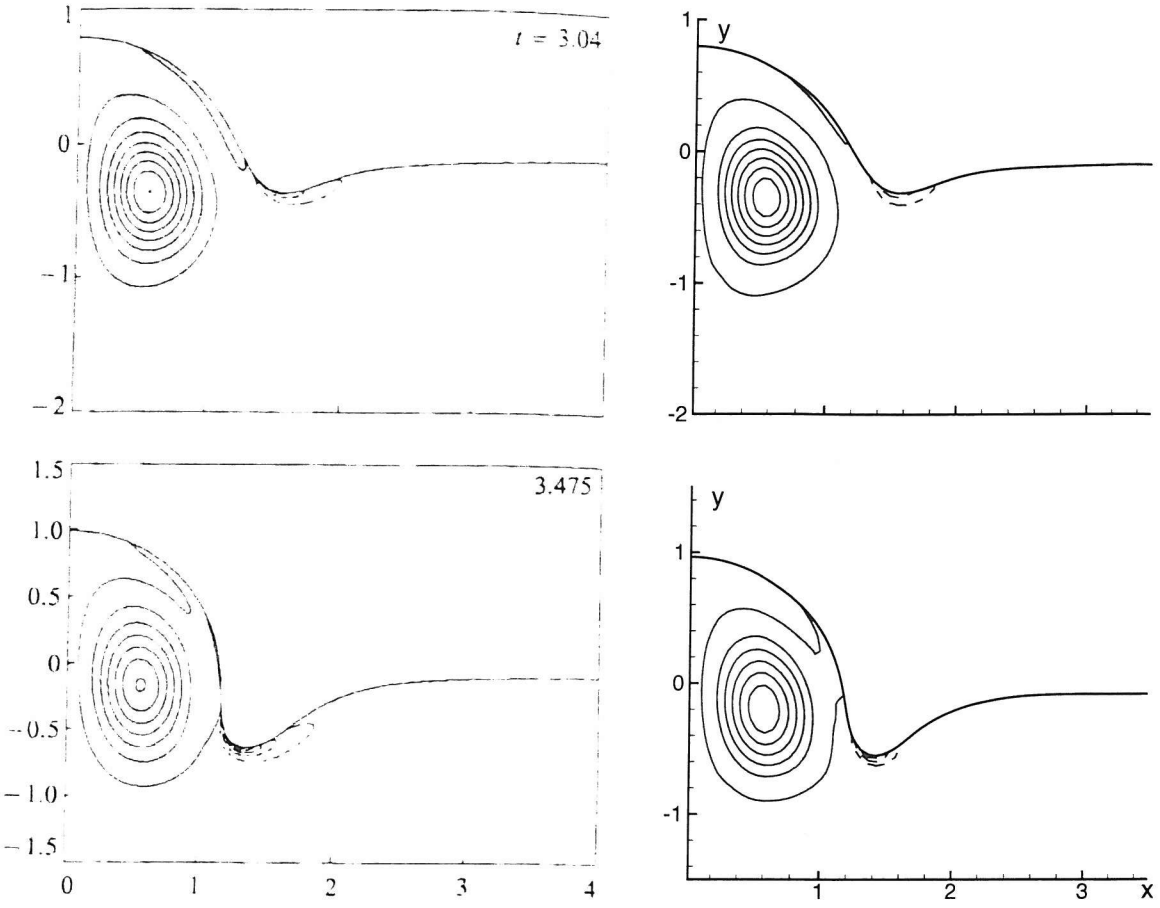

Figure 4.7: Evolution of a vortex pair rising towards the free surface. Left: numerical results from Ohring & Lugt, (1991); right: present results. The continuous contours represent the clockwise rotating vorticity and the dashed contours the anticlockwise rotation.

4.4 Dam break *plus* impact problem

The last test case refers to the dam break *plus* impact problem. The flow that develops after the dam break provides a way of evaluating the smoothing errors that are caused by the reinitialization procedure in the level set technique, as the involved time scale is quite large. The subsequent impact of the stream with a downstream structure and the resulting flow are relevant to the verification of air entrainment by the level-set.

The classical dam-break problem is schematically represented as an initially rectangular column of fluid, length L and height H, supported by a horizontal

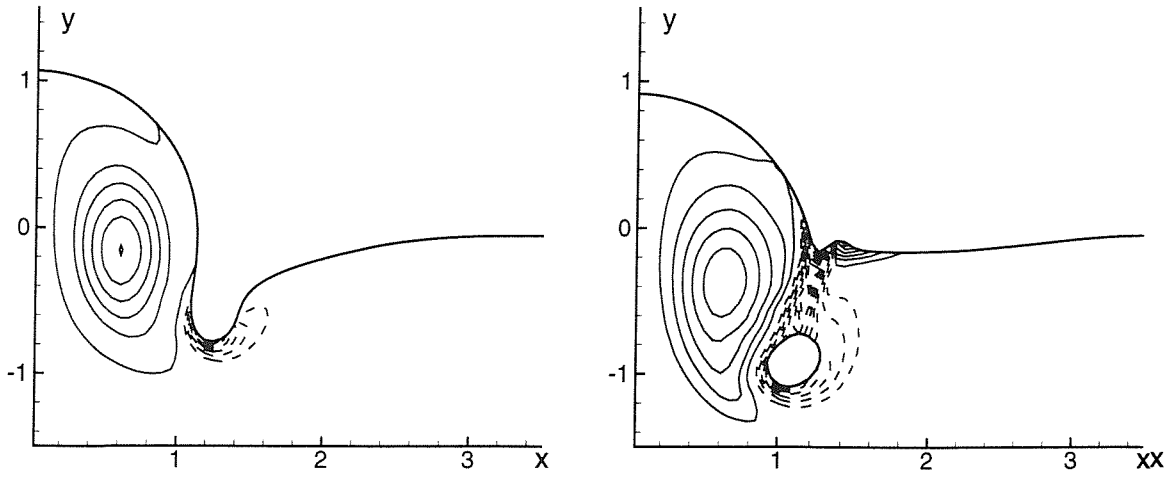

Figure 4.8: Evolution of a vortex pair rising towards the free surface. Break up of the water above the vortex and formation of a region of high anticlockwise vorticity. Left: t=4.0s. Right: t=4.8s.

bottom (deck), limited by a wall on one side and free to collapse after $t = 0$ on the other one, see figure 4.9.

The resulting flow develops a tongue of liquid quickly spreading along the horizontal boundary, without any free-surface breaking. This problem has been widely investigated both numerically and experimentally. Besides its practical applications, it is a simply-defined test case to verify and validate methods handling large deformations of the free surface. The flow that develops after the impact of the tongue of liquid with an obstacle placed downstream of the broken dam is more challenging and less well studied. In this case, overturning and breaking of the free surface are observed, leading also to air entrapment.

Present results for the dam break problem have been compared with results of two other numerical methods with quite different features: the Boundary Element Method with mixed Eulerian Lagrangian scheme (BEM, Greco, 2001) and the Smoothed Particles Hydrodynamics method (SPH, Colagrossi & Landrini, 2003). Both these two methods are based on a Lagrangian flow description. Where possible the results have also been compared with experimental data available in the literature.

The first case considered reproduces an experiment by Martin & Moyce (1952), and corresponds to $L = H = 5.7$ cm. The following non-dimensional variables have been used: $x = X/H$, $y = Y/H$, $p = P/(\rho g H)$, $f = f/(\rho g H L)$, $\tau = t\sqrt{g/H}$,

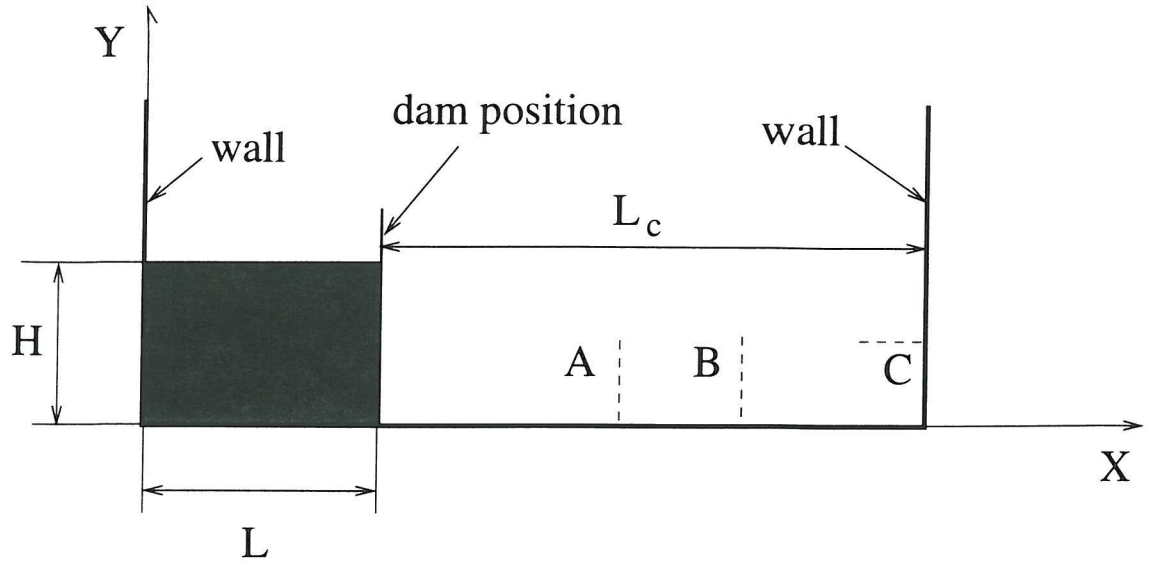

Figure 4.9: Variables definition for the dam-break problem. The shaded area represents the initial configuration of the water domain ($(X/H)_A = 3.721$, $(X/H)_B = 4.542$, $(Y/H)_C = 0.27$).

respectively for the horizontal and vertical coordinates, the pressure, the force and the time. In the experiments, the water was initially contained within the solid boundary of a water flume and a piece of wax paper, clamped between two metallic frames. The intense current produced by a short circuit was used to melt the wax and quickly release the paper diaphragm, leaving the water free to flow along the flume.

Figure 4.10 gives the propagation in time τ of the toe of the water-front, x_{max}, after the dam break.

All the numerical results are in reasonable agreement, and show a fluid smoothly accelerating and reaching an almost constant velocity on a longer time scale. The latter coincides with the analytical water-front velocity given in Ritter (1892) under the assumption of shallow-water conditions. The numerical results have a behaviour similar to the experimental data but the related water fronts are quicker. While the BEM and SPH results are inviscid, the level-set calculations have been carried out with both free slip conditions and inviscid fluid, and with non-slip conditions[1] the proper air and water viscosity. In the latter case, the

[1]The non-slip conditions used here are implemented as described in appendix E, but the grid size used for this case is not sufficiently fine to model correctly the boundary layer effects. However it can be considered indicative of the general behaviour.

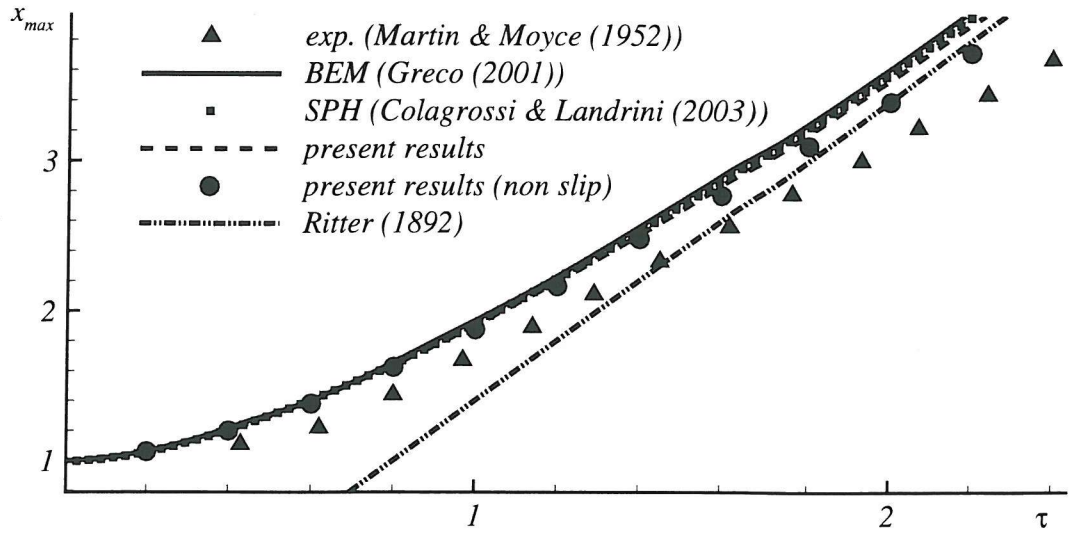

Figure 4.10: Dam-break problem. Time evolution of the water-front toe. $\tau = 0$ is the time instant for dam break and x_{max} is the instantaneous position of the water front. The analytical solution in Ritter (1982) gives the asymptotic velocity of the water front by a shallow-water theory.

water-front is slower, but not as much as in the experiments.

Several sources of uncertainties hamper a clearer comparison with the tests due to the experimental scale and to the lack of full information for the test set-up. None of the codes modelled surface-tension effects. In the experiments, two different scales ($L = 5.7$ and $L = 11.4$ cm) were considered in order to rule out significant surface-tension effects, though in both cases the radius of curvature at the water front is still rather small. Greco (2001) showed that the agreement between large-scale experiments (Dressler, 1954) and BEM is better than in the present case. Another source of uncertainty is related to the bottom roughness, which alters the propagation velocity and triggers the development of turbulence near the water front (not modelled here).

The overall free-surface profiles obtained by the three numerical methods coincided to within plotting accuracy. Differences can be detected only by a closer inspection of the water-front region, as in figure 4.11. The present method, indicated as LS in the figure (dashed lines) predicts a blunter shape, with a more rounded and slower tip. This is due to numerical errors introduced in the reinitialization process of the distance function. In fact, in this case a distance function symmetric with respect to the bottom is assumed.

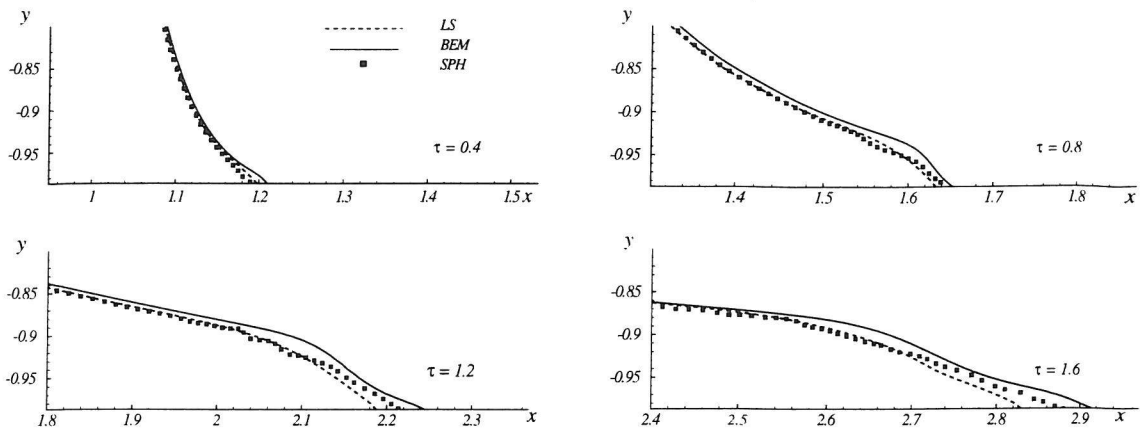

Figure 4.11: Dam-break problem. Details of the water front: free-surface configurations. Time increases from left to right and from top to bottom.

Therefore, unless the slope of the front at the bottom is vertical, the tip resembles a spike, with discontinuities of the gradient function in both the coordinate directions. Such discontinuities are smoothed by the numerical procedure, and the guessed zero level can be shifted from its correct location. However the numerical improvements, both for the discretization of the distance function and for the Navier-Stokes solver have reduced the involved errors so that the difference between the different methods after 320 steps of present simulation is still $O(\Delta x = 0.018L)$.

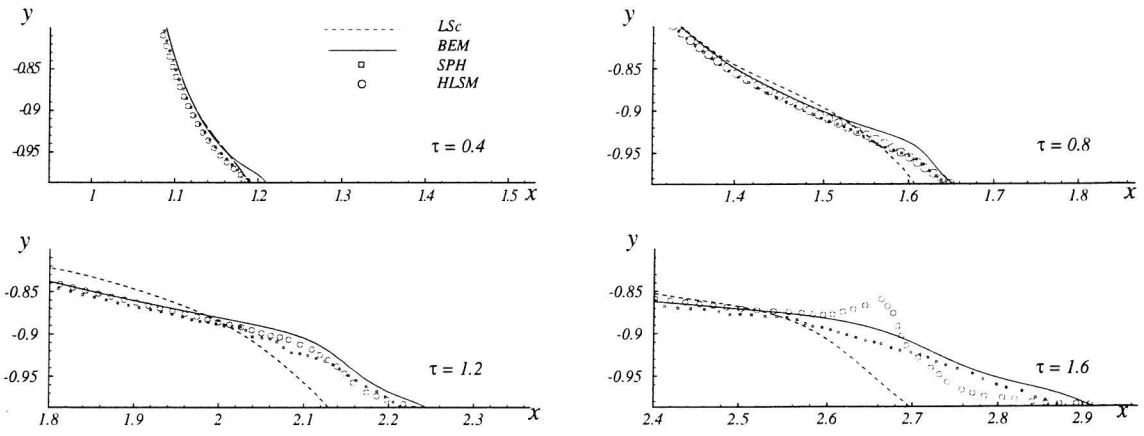

Figure 4.12: Dam-break problem. Details of the water front: free-surface configurations, with a classical Level-Set solver (LSc) and with a modified HLSM method.

To overcome some of the difficulties encountered at the front tip due to the errors in the distance function, a tracking technique has been implemented based

on the use of Lagrangian markers (HLSM method) distributed across the interface (Enright *et al.*, 2002). In this case, after the Lagrangian convection has been performed, the value of the level-set function on the grid points is updated by using the value of ϕ carried by the particles. The solution of the Navier-Stokes Equations is then performed as in the classical LS case.

Related results are presented in figure 4.12 and compared with those of the classical Level-Set solver (LSc), the BEM and the SPH methods. HLSM results agree remarkably well with the BEM and the SPH data at the initial time but the free-surface evolution shows a large deviation from the reference solutions for the last configuration (right-bottom plot in figure 4.12). This is due to some errors in the interpolation of the velocity in a region where the velocity gradients are very high.

4.4.1 Dam-break flow: impact with a vertical wall

In many practical circumstances, the water hits obstacles (break-waters, ship superstructures, etc..) causing important structural loads. This situation is represented by the presence of the wall shown in figure 4.19. Figure 4.13 shows the water induced forces f_b and f_w acting respectively on the bottom and on a downstream vertical wall placed at a distance $L_c = 1.1H$ downstream the dam. The flow is originated by the release of a reservoir of water with $L = H$.

The agreement between the present solver and the other numerical methods is very good, disregarding the rather small oscillations in the SPH computation. Even the jumps in the force that are related to the impact of the fluid onto the downstream vertical wall are in reasonable agreement. The slightly smaller velocity of the Level-Set front has not strongly influenced the dynamic behaviour at the impact on the wall. In fact, the forces acting both on the bottom and on the vertical wall are very similar to those obtained by the other two methods.

The substantial difference among the three numerical solvers is in the slope of the force acting on the vertical wall during the initial stage of the impact of the water toe on it: a high peak of f_w, with short duration, is found by the BEM method. At the impact time, the water front can be approximated by half a wedge with an angle of about $\alpha_1 = 60°$, followed by a free surface with mean slope $\alpha_2 = 25°$. By using a gravity-less similarity solution for the impact of a fluid wedge against the wall (Zhang *et al.*, 1996), the forces reported in figure 4.14 have been found for the angles α_1 and α_2. The results suggest that the higher peak of the

BEM impact force is due to the impact of the blunter portion of the water front, but the oscillations of the SPH are very likely to be the results of some numerical instabilities. The local refinement of the BEM is higher than in the SPH and in the present computations, which do not capture properly the initial rate of change in the horizontal load. The same can be inferred for the Level Set solution. The present solver presents a delay in the increase of the horizontal force due to the delay in the water toe impacting on the vertical wall. However the initial force peak is associated with quite a short time scale and therefore it is likely unimportant from a structural point of view.

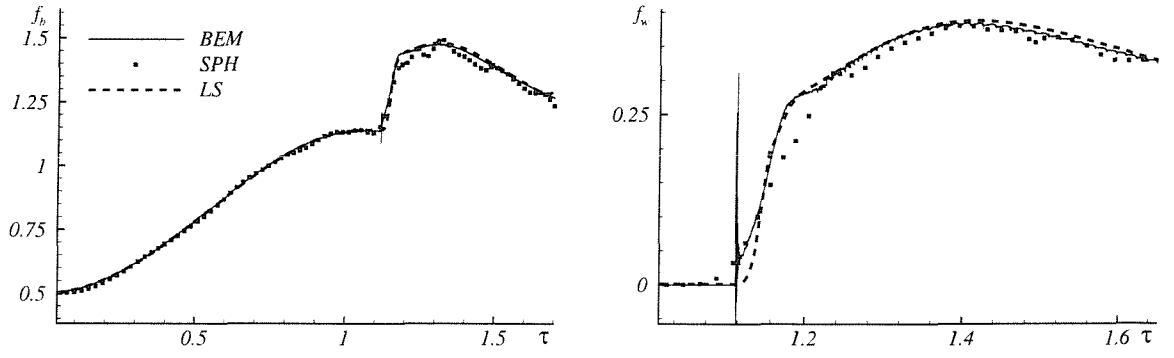

Figure 4.13: Dam-break *plus* impact problem. Left: time evolution of the vertical load on the horizontal deck after the dam break. Right: time evolution of the horizontal load on the vertical downstream wall at $L_c = 1.1H$ from the dam.

In the experiments by Zhou *et al.* (1999), a reservoir of water, with $H = 60$ cm and $L = 2H$ was placed at a distance $L_c = 3.366\,H$ from a vertical obstacle. Wave height measurements were performed at the locations A and B shown in figure 4.9. The pressure evolution was measured at the position C along the vertical wall. The sequence in figure 4.15 shows the global development of the fluid flow as obtained by the numerics. For the SPH only the free-surface particle layer is plotted, and for the present solver the continuous lines represent the zero-level of the distance function ϕ. After the dam is removed, the flow develops along the deck, impacting against the vertical wall, where it is deviated upwards. Formation of spray and surface fragmentation (which cannot be handled by the BEM) may occur. The Level-Set suffers from insufficient resolution and is quite dependent on the numerical discretization adopted. The SPH predicts high particle velocities, and some of them leave the main bulk of the fluid. The accuracy of these details is hard to assess.

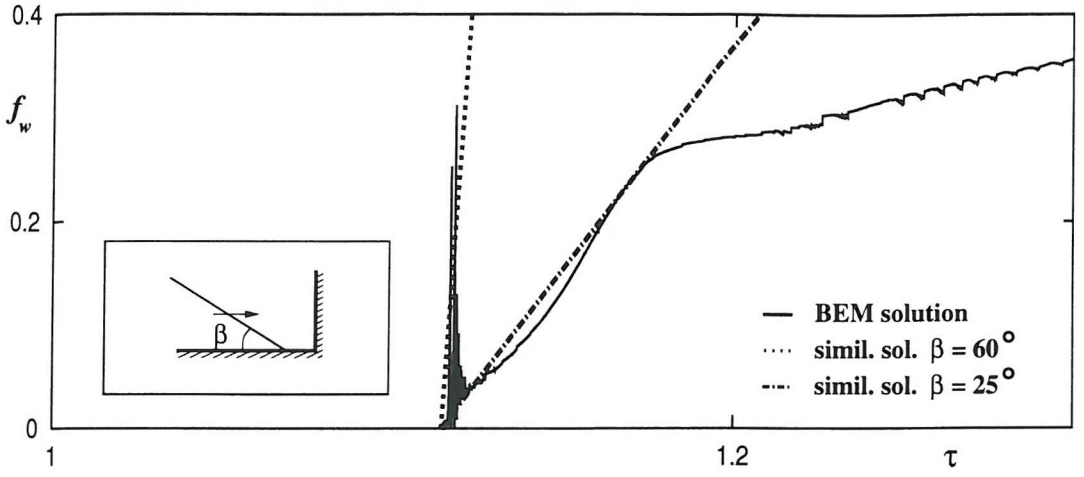

Figure 4.14: Dam-break *plus* impact problem. Time evolution of the impact force on the vertical wall at $L_c = 1.1H$ from the dam. The zero-gravity results are obtained numerically by using the free-surface data following from Zhang *et al.* (1996).

Initially, under the restoring action of gravity, the fluid acceleration decreases and the jet slows down. The motion of the water is reversed in a waterfall, overturning in the form of a wave plunging onto the deck. The three methods agree quite well despite the complexity of the flow field. Though no experimental data are available for the free-surface profile, the agreement is encouraging. Some

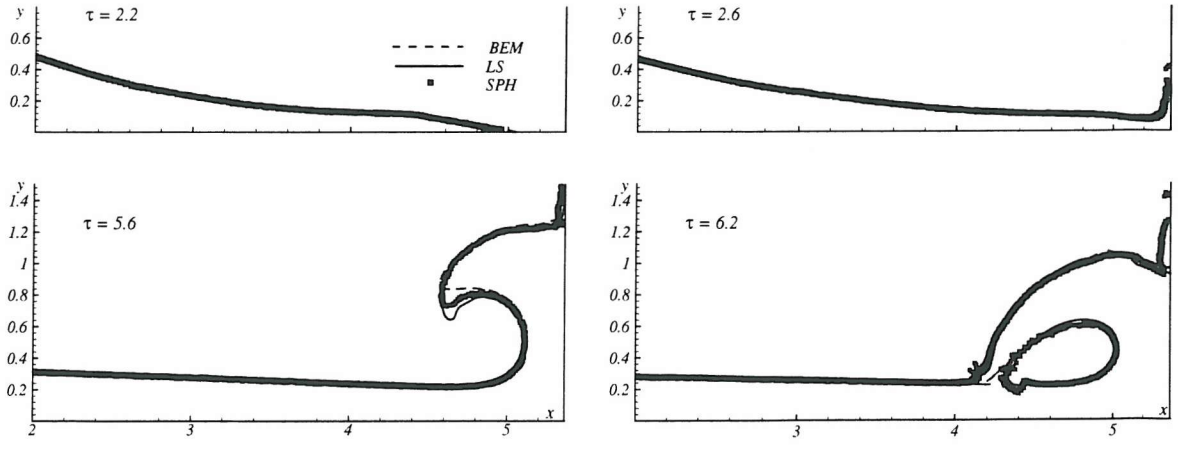

Figure 4.15: Dam-break *plus* impact problem. Free-surface flow and impact against the vertical wall following the breaking of the dam.

difference appears at time $\tau = 5.6$ when both the present solver and the SPH predict a lower jet with respect to the BEM. This is due to the presence of the gaseous phase. The effect of the air escaping out from the cavity created below the jet could contribute to a downwards acceleration of the tip.

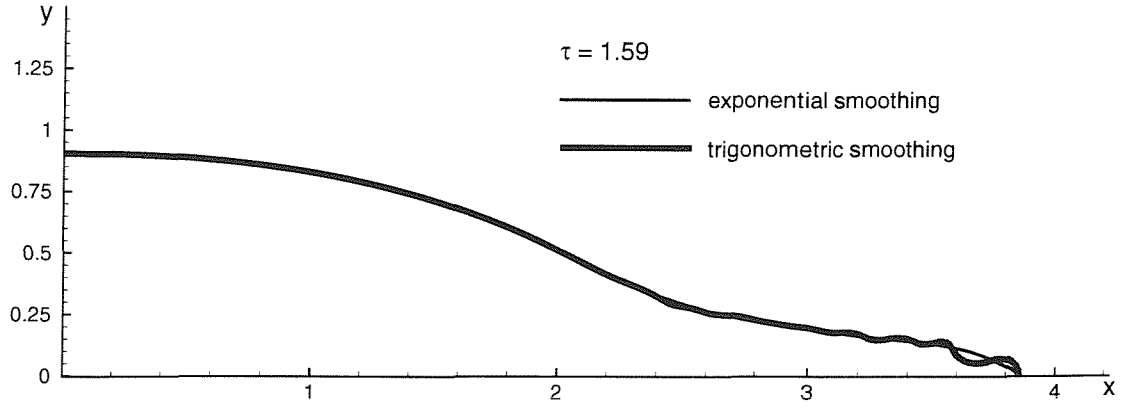

Figure 4.16: Dam-break *plus* impact problem. Effects of the different numerical smoothing at the interface. Dashed line: exponential smoothing, solid line: trigonometric smoothing.

The BEM simulation has to be stopped at the impact of the plunging wave with the underlying water, while both the present method and the SPH are able to continue further on.

The general agreement highlights the successful efforts in the development of the numerical aspects of the present solver. Given the spatial discretization used here ($\Delta x = \Delta y$=0.018H and $\delta_{smoothing\rho} = 1.5\Delta x$), the exponential smoothing of the density described in section 3.14 hamper the growth of instabilities allowing the reduction of the time step to $\Delta\tau = 0.018$. Figure 4.16 shows how substantial oscillations can be introduced in the computation with the same Δt by using instead a trigonometric smoothing of the density across the interface (see section 3.14). The thinner line of the figure represents the air-water interface for the present case if the exponential smoothing is adopted, the thicker line is the equivalent configuration at time $\tau = 1.59$ when a trigonometric smoothing is adopted. Most of the oscillations are concentrated at the toe of the water flow, where shallow water conditions occur and where the water front changes rapidly.

These oscillations can be reduced using a smaller $\Delta\tau$ and enlarging $\delta_{smoothing\rho}$, though the solution is then less accurate and less efficient.

The advantages that are derived from the use of a variable coefficients ENO advective scheme (see section 3.2.2) cannot be achieved with any reduction of $\Delta\tau$. The left plot of figure 4.17 shows the interface calculated by applying the variable coefficients methods and a more commonly used minmod scheme. The SPH interface is also given in the plot. The evolution of the plunging jet obtained by

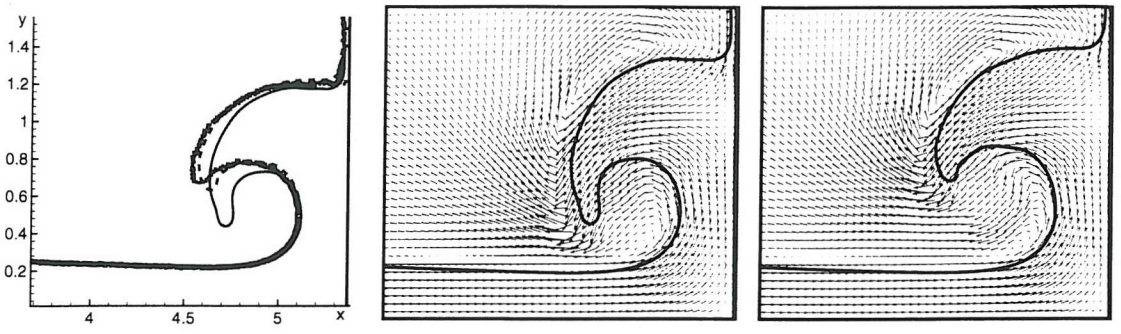

Figure 4.17: Effects of the limiter function on the plunging jet. Left: comparison of the interface location with (dashed line) and without (solid line) using the variable-coefficient limiter function. The SPH solution (dots) is used as a reference. Centre: flow velocity when a minmod limiter is used. Right: flow velocity when a variable coefficient ENO scheme is adopted. $\tau = 5.64$.

the variable coefficient method is closer to the SPH solution. In the central and right plots of figure 4.17 the velocity field is shown for the cases respectively without and with a variable coefficients ENO scheme. In the former, the vortical region present in the air below the plunging jet is diffused to the water domain by the minmod scheme. This results in an unphysical nose down effect. Even though it is closer to the SPH and to BEM solutions, the interface obtained with the new method still presents some residue diffusion effect. This may be related both to a too narrow transition from the superbee to the minmod scheme (see section 3.2.2) and to the variation of the density ρ within a finite layer across the interface. The latter causes the thickening of the vortex sheet concentrated on the interface. So that the vorticity is spread over a region affected by higher numerical diffusion because of the chosen limiter function (see section 3.2.2).

Nevertheless, the evolution of the interface is much improved, and it is possible to proceed to a more quantitative analysis of physical quantities involved in the problem.

Figure 4.18 gives the time evolution of the water height h_w at $(X/H)_{\mathrm{A}} = 3.721$ and $(X/H)_{\mathrm{B}} = 4.542$ along the deck. From the analysis of the numerical

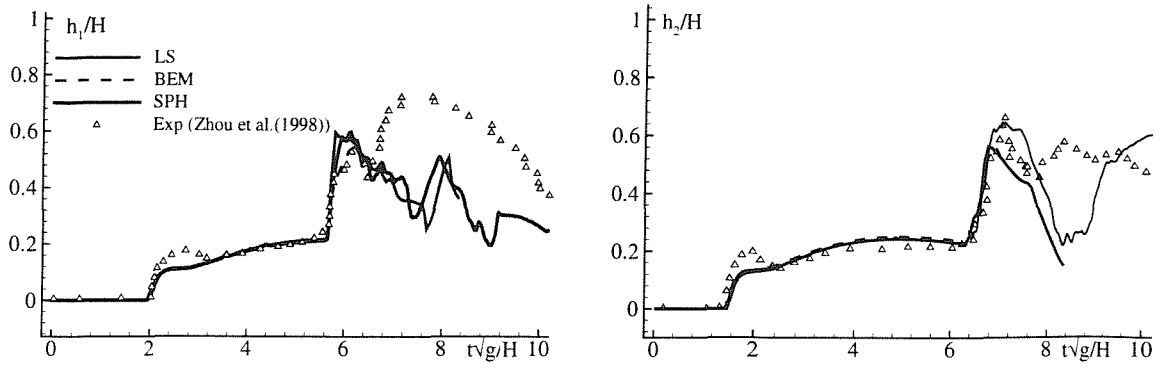

Figure 4.18: Dam-break problem *plus* impact problem. Water height at locations A, left, and B, right, (cf. fig. 4.9). Numerical results and experiments in Zhou *et al.* (1999), with $H = 60$ cm and $L = 2H$.

simulations and of the experiments the three fundamental stages have been identified by Greco (2001):

1. Stage I: ($\tau \simeq 1.6 - 2.0$) is characterized by the sudden rise of the water level h_w, due to the transition from dry-deck conditions to wet-deck conditions. The shape of the water front determines the growth rate of h_w. Some differences can be detected between the numerical solutions and the experimental measurements.

2. Stage II: ($\tau \simeq 2. - 5.6$) is characterized by a much slower growth rate of the water level because of the almost flat free surface above the wave gauges.

3. Stage III: ($\tau \geq 5.6$) shows a new steep increase of h_w. This is due to the overturning water which gives an additional contribution to the water depth measured at the location B. Later on, also the signal recorded by the gauge located in A displays this phenomenon, which cannot be followed further on by the BEM, while it is qualitatively captured by the SPH and by the present solver.

Though the experimental and numerical evolutions are in satisfactory agreement, in figure 4.18 the numerical solutions underpredict the measured data when the water level first rises from zero, and the measured h_w has a maximum which is not present in the numerics. As suggested in Greco (2001), the temporal record can be converted into a spatial free-surface profile and suggests a hump in the experimental free surface close to the contact point. This is not visible in the

dam-breaking free-surface profiles by Dressler (1954) and could be due to the deck not being perfectly dry before the breaking of the dam. This is consistent with other flow visualizations in Stansby *et al.* (1998). Unfortunately, the limited set of data available does not allow a better verification of the reasons of the differences. Similar uncertainties affect the analysis of the post breaking values of the water depth. At this stage, the present solver and the SPH have similar behaviour but results that differ from the measurements.

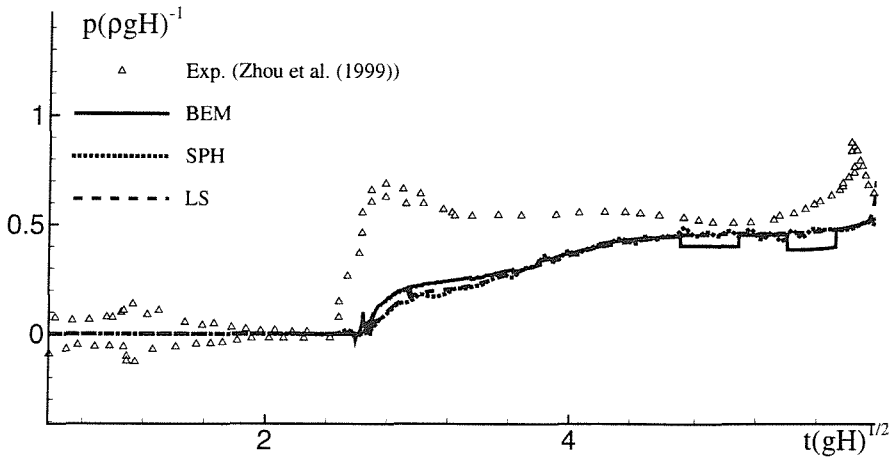

Figure 4.19: Dam-break *plus* impact problem. Pressure measured in Zhou *et al.* (1999) at the circular transducer located at C (see figure 4.9). BEM, SPH, and LS pressure computations at the centre of location C.

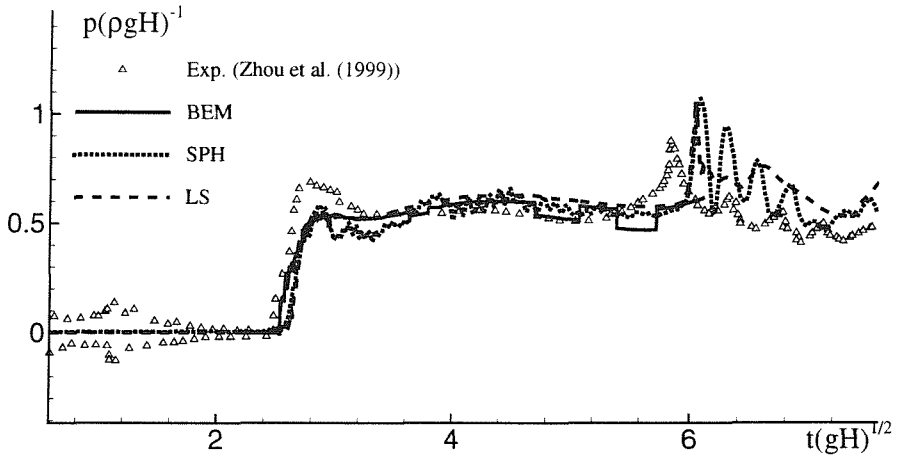

Figure 4.20: Dam-break *plus* impact problem. The numerical pressure evaluated at the bottom boundary of the circular transducer area (Zhou *et al.*, 1999), along the vertical wall.

Figure 4.19 gives the pressure measured (Zhou *et al.*, 1999) on the vertical wall during the impact. In the experiments, a circular shaped gauge of 9 cm diameter

centred at C ($0.27H$ above the deck) was used. In the figure the measurements are compared with the numerical values computed at that location[2]. The agreement between computations and experiments is rather limited. Actually, Zhou *et al.* (1999) also reported difficulties in achieving repeatability of the measurements, so no conclusive statement can be made. The pressure undergoes large variations within the area of the transducer. Indeed the measured pressure time series is closer to the pressure computed at the bottom boundary of the transducer area along the vertical wall, as shown in figure 4.20. All three numerical methods are in a good agreement up to the point of breaking ($\tau = 6.2$), when the BEM is halted.

The present solver and the SPH predict a similar evolution of the pressure after that time. A first peak of pressure just before the closure of the cavity below the jet is present in both solutions at $\tau = 6.18$. This is due to the effect of the entrapped air, and is characterized by a pressure peak just before the closure of the cavity. This is immediately transmitted to the water. The differences in amplitude of the peaks predicted by the two methods can be due to the compressibility of the air, captured by the SPH, and disregarded by the present solver which assumes both air and water to be incompressible. Later, the evolution of the pressure is again similar apart from some oscillations of the SPH pressure due to the numerical semi-compressibility of the water in that technique.

4.4.2 Post-breaking flow evolution

The comparisons with the BEM are necessarily limited to the pre-breaking phase, but the present solver can still compare with the two-phase SPH method. Satisfactory comparisons during the post-breaking phase have already been shown both in water level and pressure (see the previous figures 4.18 and 4.20). Here the evolution of the air-water interface is discussed.

Figure 4.21 shows the interface at the formation of the splash up. Apart from the tip of the jet the results are similar. The two solutions show a similar deformation of the air entrapped inside the water domain and a similar evolution near the right wall. When the thin layer of water sliding on the wall starts to fall down, it creates a cavity that eventually closes. A rather comparable deformation of this cavity is found in the two solutions. Even at this stage, when the interface is extremely deformed, the two methods predict a similar deformation of the

[2]The pressure has been computed as an average value on the whole gauge area, but these results were also not very satisfactory.

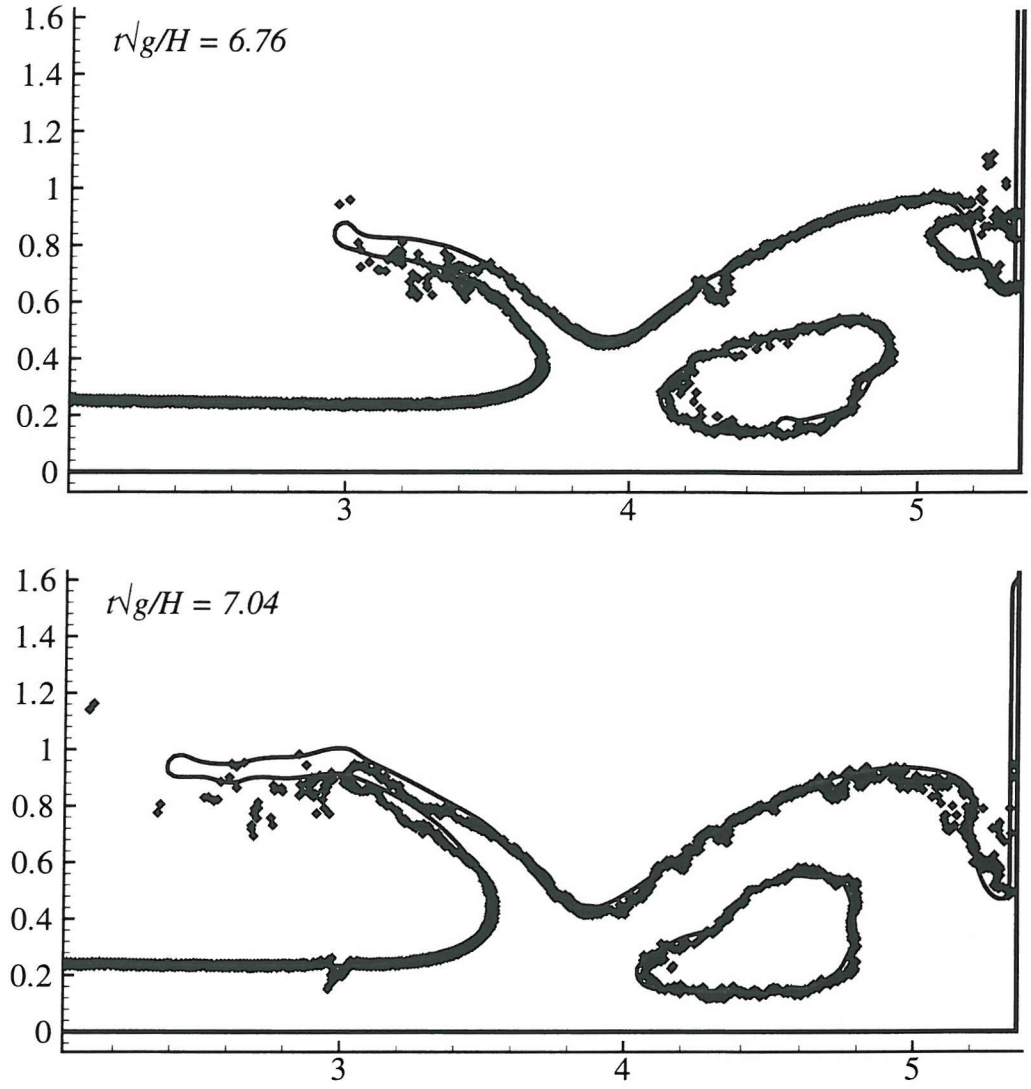

Figure 4.21: Interface evolution after the impact. Solid line: level set, dots: SPH.

entrapped air and of the splash up. This is a quite relevant result, the two solvers being profoundly different. The positive comparison validates the new features introduced in the present numerical solver. Figure 4.22 shows the air-water interface obtained with the reinitialization method by Russo & Smereka (2000) (dashed line), the scheme described in section 3.3 (solid line) and the SPH solution (double dotted line). The use of the present method recovers the presence of the thin layer of water on the right wall that is smoothed out by the other level set scheme. In the absence of this thin layer of water there can be no subsequent cavity in the water further entrapped near the right wall.

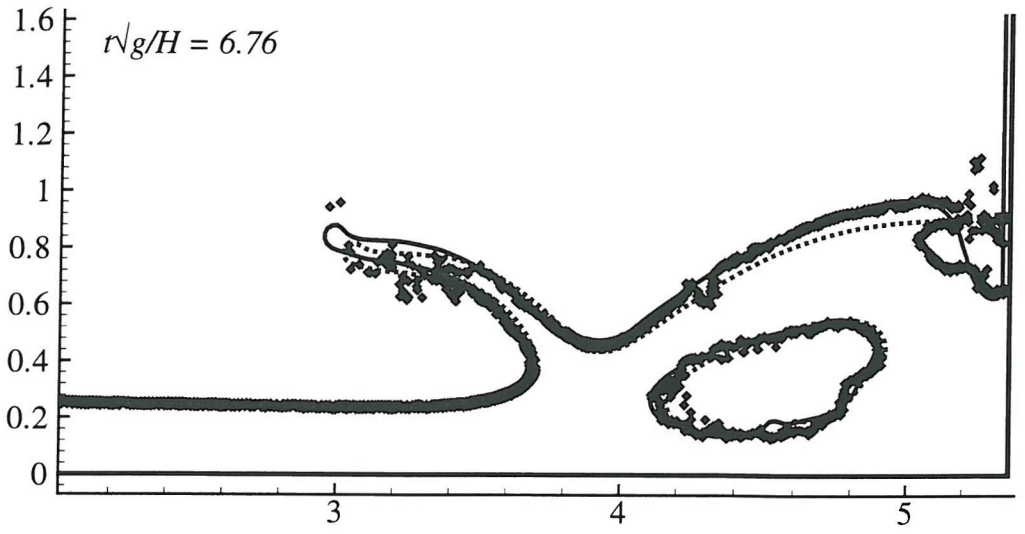

Figure 4.22: Effects of the different reinitialization procedure. Solid line: present correction, dashed line: correction described by Russo & Smereka (2000). Double dots: SPH solution.

4.5 Conclusions

In this chapter the numerical solver developed in chapter 3 has been verified and validated by studying simple prototype problems where phenomena relevant for the hydrodynamics fields are involved.

The single bubble problem has highlighted the accuracy and efficiency of the splitting technique for the Poisson equation in modelling the surface tension effects.

The problem of the vortex pair has shown that the Cartesian grid handles accurately the deformation of the free surface caused by the approaching vorticity.

The dam-break problem has been a valuable source of comparison with experiments and other numerical solvers. Breaking and post-breaking behaviours have been studied and have confirmed the method's capabilities. The long time evolution of the phenomena has allowed the new numerical features introduced in the discretization of the algorithm to be rigorously tested. The corrections by Russo & Smereka (2000) have been applied for the first time to the fluid-dynamic problems, and further corrections have resulted in a considerable gain in the accuracy of the interface evolution. The exponential smoothing of the density resulted in a more efficient algorithm, and the variable coefficients ENO scheme eliminated errors of diffusion across the two fluid domains.

Part II

Surface piercing plate problem: numerical results versus dedicated experiments for two-phase flows

There lies the port; the vessl puffs her sail;
thre gloom the dar, briad seas. My mariners,
souls that have toil'd and wrought, and
thought with me
Ulysses, Alfred Tennyson

Chapter 5

Experimental set up

In the previous chapter the study of simple prototype problems guided the improvement of the numerical method. In the next chapter, the developed solver will be applied for the analysis of a geometrically simple problem involving the coexistence and interaction of the phenomena investigated in the prototype cases individually. This problem is that of a surface piercing plate in forward motion, for which dedicated experiments have been performed. In this chapter the experimental set up is outlined.

5.1 General description of the problem

The experimental images shown in figure 5.1 depict the evolution of the phenomena involved in the motion of a surface piercing plate. A vertical plate initially at rest (top left plot) starts to move from left to right. This causes the water level to rise on that side. Gravity progressively counteracts the water rise up and leads to the formation of a plunging breaker followed by air entrainment. The motion of the plate also causes a drop in the water level on the left. There, the lowered air-water interface approaches the region where vorticity is released at the lower tip of the plate (bubbly region) and interacts with it. The chosen geometry of the body makes the problem easy to analyze both from a numerical and an experimental point of view: 1) no uncertainty derives from the shape of the body, 2) the vorticity is released in a fixed point. This makes the problem fascinating for

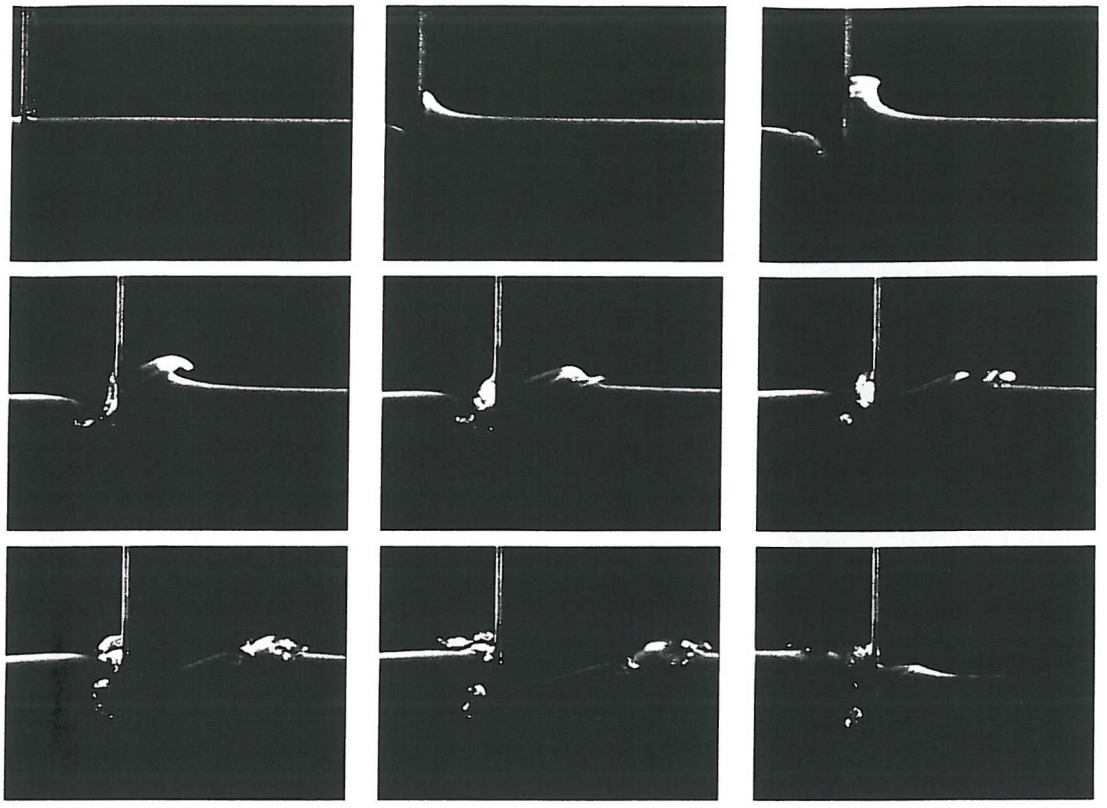

Figure 5.1: Evolution of the flow field after the vertical surface piercing plate starts to move from left to right. The white shaded region represents the air-water interface. Time increases from left to right and from top to bottom.

the validation of numerical codes.

But its validity extends to a wider field. Topologically it resembles the problems of blunt bow forms such as those of shape of cargo ships and of transom sterns. So the phenomena hereafter described give a description of the general processes that take place around three-dimensional blunt bodies.

5.2 Experimental set up

The experimental set up is sketched in figure 5.2. The experiments were performed in a flume 0.420 mm wide, 18 m long and at a water depth larger than 0.6 m so that the effects of the bottom are not significant in all the cases analyzed here. An aluminium plate is towed along the flume and the flow features are captured by a video-camera (to visualize the air-water interface displacement) placed at the side of the flume, and by a Laser Doppler Anemometry (LDA) device (to measure the velocity field).

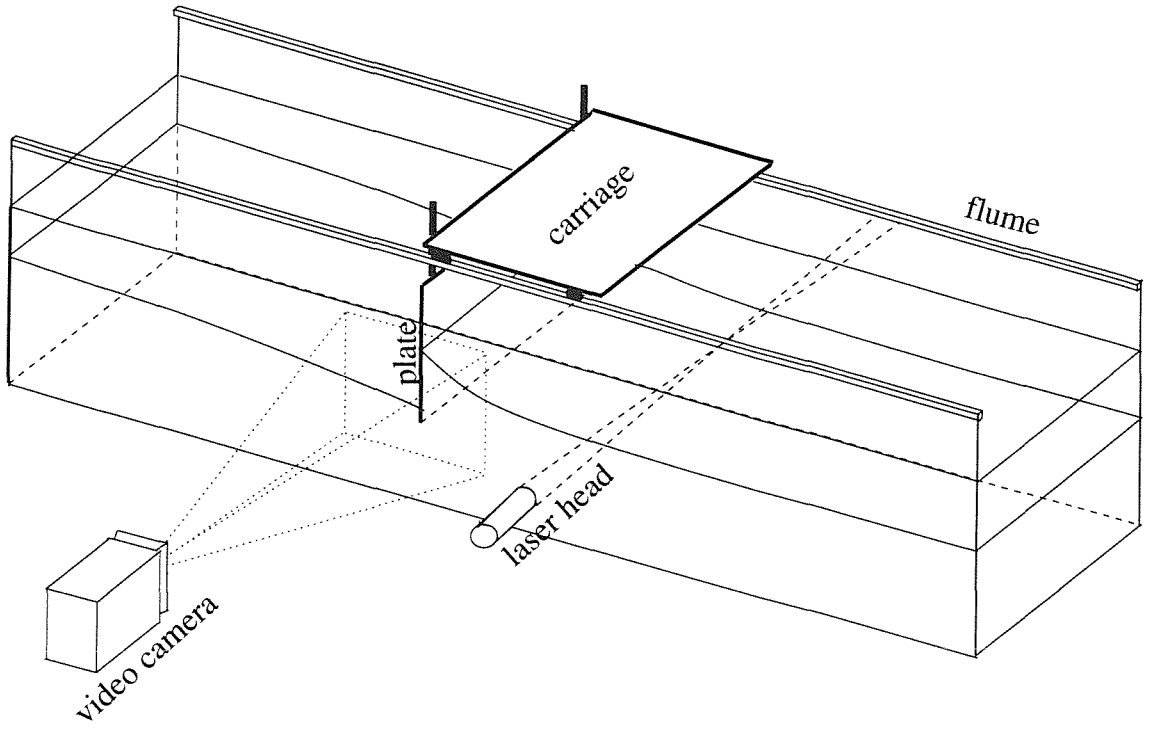

Figure 5.2: Experimental set up.

Two test campaigns have been carried out. The former analyzed the motion of a vertical plate, the latter considered the case of an inclined plate.

The vertical plate is 300mm long, 415mm large and 5mm wide. It is supported by two vertical guides, linked to the carriage. The elevation of the plate on the vertical guides was adjustable.

A soft plastic material was used at the two sides of the plate, thus allowing an almost perfect contact with the walls of the flume; leaks at the two sides of the plate are reduced to a minimum to ensure two-dimensional flow conditions during the tests.

The inclined plate is 500mm long, 415mm wide and 3mm thick (with sharp corners). The distance between the lower edge and the point where the plate is clamped to the rigid support attached to the carriage is 260mm (see figure 5.3). In this case no sealing was used between the plate and glass walls of the flume.

5.3 Measuring devices

Different devices were used to control the flow conditions and to measure the relevant physical quantities. They are described below.

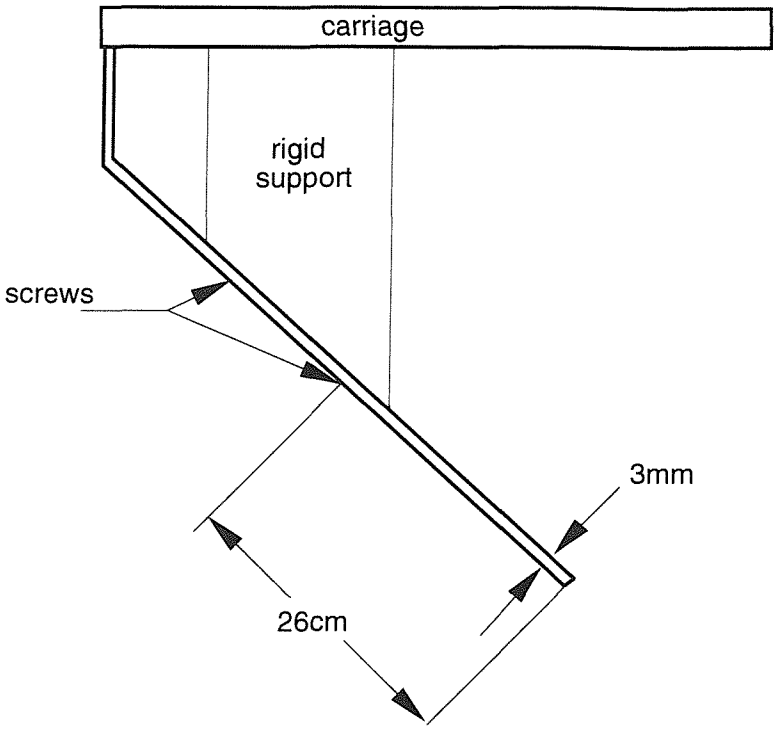

Figure 5.3: Geometry of the inclined plate.

Position transducer An optical encoder mounted on a drive shaft that measures the angular position is used to measure the velocity of the plate and its displacement with a sample rate of 200Hz.

Motion control For low speed tests (velocities up to 0.55m/s), the sketch in figure 5.4 shows the mechanism used. A PC controls the motion of a DC motor connected through a ballscrew to the carriage. An analogic position transducer is connected to this and sends back its information to an Analogical/Digital interface and from this to the PC. This feedback is particularly important in cases where the motion was reversed. The PC sends a signal similar to the black solid line of figure 5.5 to the motor and waits. The displacement of the plate is affected by inertial, frictional and water drag effects, so that the signal back to the PC resembles dotted line in figure 5.5. When the position indicated by the transducer is equal to the limit position imposed by the PC a new signal is given to the motor by the computer for the backward motion.

For higher speeds (up to 0.9ms/s), the carriage was moved simply by hand. Its motion was measured by the position transducer and double checked with the motion filmed by the video camera.

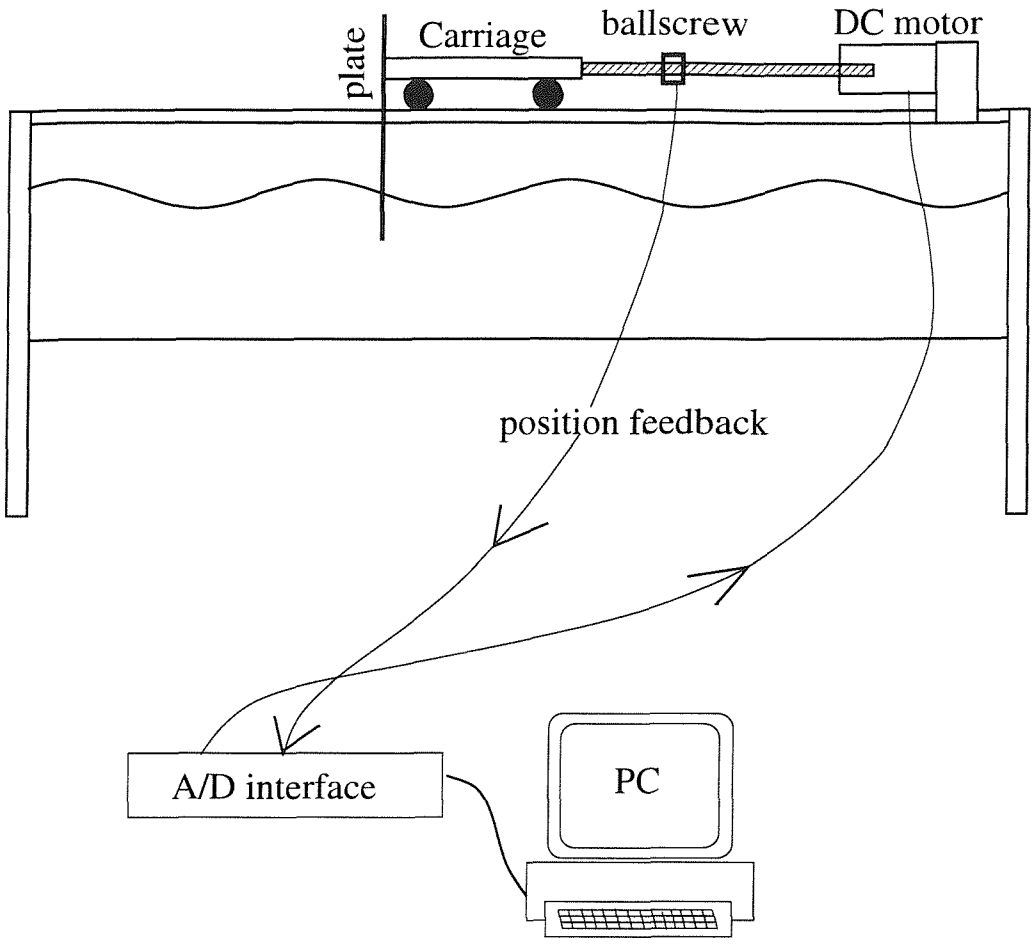

Figure 5.4: Sketch of the feedback mechanism for the control of the plate motion.

Videocamera A PULNiX TM-6710 progressive scan CCD camera was used for the flow visualizations. It is characterized by a high resolution 1/2" progressive scanning interline transfer CCD imager 648(H)x484(V). No shutter was used in this occasion but the camera was run at a data rate of 120 frame/sec. The calibration of the images for the measurements is done using a grid printed on the glass wall of the flume.

For a better definition of the air-water interface a fluorescent dye was dispersed in the water and illuminated by two halogen lamps.

LDA device A TSI 2 components Argon-Ion Laser Doppler anemometer has been used with a frequency counter. The data rate of the measured velocities is 3100 samples per second.

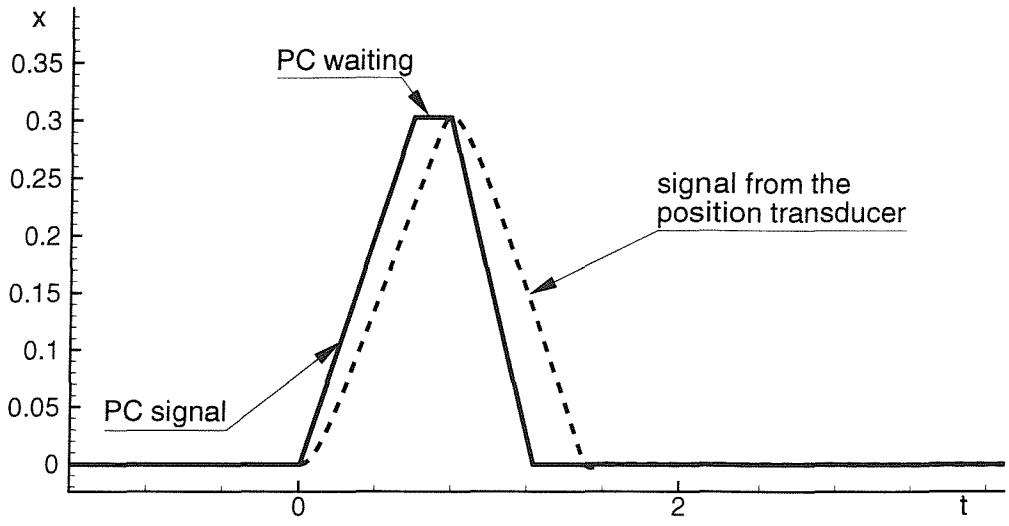

Figure 5.5: Driving signal from the PC (solid line) and position feedback from the position transducer (dashed line).

5.4 Experimental uncertainties and test repeatability

5.4.1 Instrumentation and set up

Uncertainties in the measurements could be associated with both the individual measuring devices and with the global features of the resulting experimental set up potentially responsible for generating uncontrolled phenomena. The limits of the measuring devices are as follows.

- The position transducer ensures a maximum error of $\pm$1millimetre in the measurement of the position on the calibration range of 0.9m.

- The parallax errors of the video images are within the order of a millimetre, but three dimensional effects are difficult to quantify.

- The LDA device was set with a frequency shift equal to 200KHz and with a band pass filter in the range [30KHz,300KHz]. This results in satisfactory measurements in the velocity range [-0.6m/s,0.9m/s], and in a error in the measurement of the velocity in still water condition equal to $\pm$0.02m/s.

The relative position of the plate and the laser head is the cause of a further error in the LDA measurements. An error is potentially generated by the reflections of the laser beams on the plate. The horizontal velocity is measured by two crossing beams in the horizontal plane, and when the plate sweeps into the

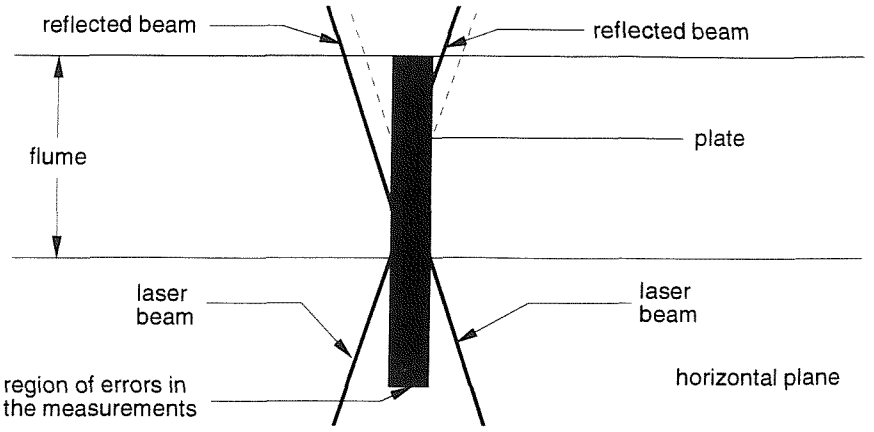

Figure 5.6: Sketch of the horizontal plane where the horizontal component of the velocity is measured. The dimensions are altered to evidence the shaded region where the reflection of the laser beams produce an error in the velocity measurements.

space between the beams it may result in a contaminated measurement of the velocity (see figure 5.6). Usually however, the direct effect is either a lack of points or a constant value of the measured velocity for a small interval of time when the plate crosses the test section.

Other uncertainties are related to the plate system and have an effect on the evolution of the flow. In the case of the vertical plate, the plate rotates slightly around the upper hinge of the carriage owing to the fluid loading on it. Even though it was not possible to measure the amplitude of the oscillations precisely, the video images give a rough idea of what happens when the plate stops: the lower tip of the plate has an oscillation whose amplitude is slightly larger than half a centimetre. In the case of the inclined plate, the uncertainties are introduced by the bending of the plate. The plate used is made of stainless steel and its geometry is described in figure 5.3. Considering it to be rigidly connected to the support, the natural frequency of the plate is given by

$$\omega = 3.52\sqrt{\frac{EI}{\rho l^4}} \simeq 2\pi \times 13Hz \ .$$

The immediate effects of the rotation and of the bending of the plates is on the velocity in proximity of the plate and eventually on the shear layer release at the lower tip of the plate. In fact a frequency similar to the frequency of bending ω calculated above has been observed in the velocity measurements and described in the following chapters.

Another source of uncertainty derives from the water leakage between the sides of the plate and the tank walls. The main effects of this water flow are on the release of vorticity in the direction of the lower tip of the plate.

5.4.2 Test repeatability

The repeatability of the experiments was tested both for the displacement of the plate and for the LDA measurements in the case of the lowest velocity. Different runs were analyzed showing a maximum deviation of the plate position of the order of one millimetre, that is in the error range of the instruments. Wider errors were detected on the velocity measurements with a maximum difference in the LDA measurements of 0.07m/s between successive nominally identical runs.

5.4.3 Initial and boundary conditions

The runs were repeated on average at a time interval of 1 minute. This value has been chosen as a compromise between efficiency in the test campaign and test reliability. With this time interval, the initial conditions can be assumed to be still water. The LDA measurements gave a value of velocity within the error of the instrument, before the movement of the plate.

To reduce the time interval between two successive runs, the reflections from the flume ends were damped out efficiently by a sponge beach at one end of the flume and by a wave-maker used as a wave-absorber on the other end.

5.5 Main phenomena observed in the experiments

Hereafter some of the features observed in the flow visualization are qualitatively described. The phenomena studied experimentally involve small spatial scales. Therefore surface tension effects are not negligible. An example of this is shown in figure 5.7. The jet that develops is characterized by high curvature at its tip, the surface tension causes its rounding and at a later time the extreme of the jet becomes thicker and almost circular (see right plot of the figure 5.7).

Once the breaking of the plunging jet has occurred and the plate has stopped, the water in front of the plate rises again to reach almost the zero level, and the surface becomes wavy. Also this phenomenon may be connected with surface

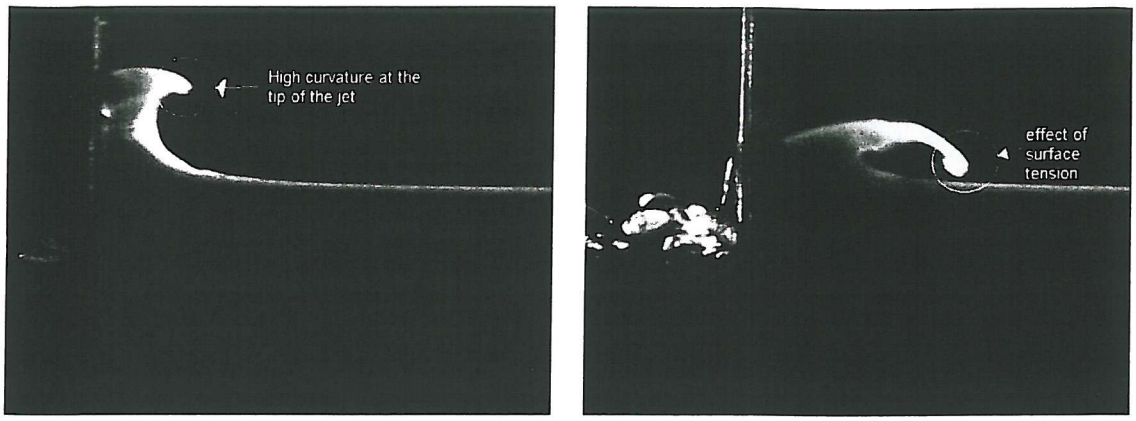

Figure 5.7: Effects of surface tension: the spiky jet is rounded by the surface tension.

tension. The oscillations could also be given by an angular oscillation (pitch) of the plate during the tests. Unfortunately no information is available about this aspect. Three-dimensional effects should be ruled out by the prevention of leakage at the flume sides.

Other effects of surface tension are not easily detectable but they substantially enter the problem. As confirmed by the numerical results, agreement is not satisfactory if surface tension is omitted.

The lights begin to twinkle from the rocks;
the long day wanes; the slow moon clinbs;
the deep moans round with many voices.
Ulysses, Alfred Tennyson

Chapter 6

Flow field around a vertical plate

In this chapter the flow field around a vertical plate is analyzed both from a numerical and an experimental point of view. Two cases have been considered: a) at low speed, high immersion and with an abrupt stop of the plate ($Fn = 0.37$) and b) at high speed, low immersion but with smooth variation of the velocity of the plate ($Fn = 1.0$). This analysis is useful for investigating the effects of the velocity and of the body acceleration on the flow developing around the plate.

6.1 Vertical plate at low speed and high immersion

The characteristic lengths of the problem studied here and the non-dimensional numbers used hereafter are summarized in figure 6.1. For the first set of experiments the maximum velocity of the plate was 0.5m/s and the initial submergence ($h = 0.18m$). These conditions[1] lead to Froude number $Fn = 0.37$, a Reynolds number $Re = 5.9 \cdot 10^4$ and Weber number $We = 388$.

Figure 6.2 shows the evolution of the displacement x_p, of the velocity u_p and of the acceleration a_p of the vertical plate for the case analyzed in this section. Two sets of data are given in figure 6.2: the dots represent the experimental displacement of the plate measured by the position transducer and its derivatives, and the solid lines represent the smoothed curves of the displacement used as

[1]The nominal surface tension value between air and water is used ($\sigma = 0.0728N/m$).

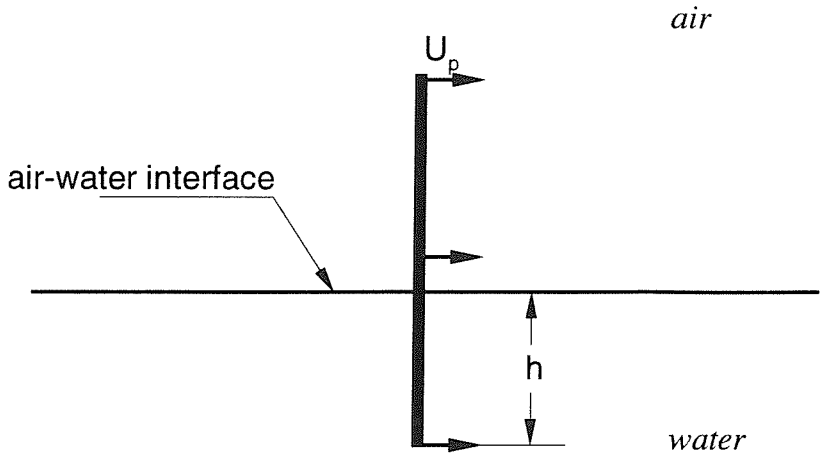

$$Fn = U_p/(gh)^{1/2} \qquad Re = (U_p h \rho_w)/\mu_w \qquad We = (U_p^2 h \rho_w)/\sigma$$

Figure 6.1: Sketch of the characteristic lengths of the problem. The non dimensional numbers are indicated.

input in the numerical calculation[2] and the corresponding velocity and acceleration. This implies that small differences exist between experimental and numerical data when steep gradients are present.

The value of the Froude number used in this test implies a weak interaction between the vorticity released at the lower tip of the plate and the free surface. Moreover, during the first stages of motion, there were no violent deformations of the free surface, nor any fragmentation. However, after the abrupt stop of the plate, much more violent flow occurs.

6.1.1 Evolution of the air-water interface

Figure 6.3 presents a series of experimental pictures referring to the deformation of the free surface, when the plate moves as shown in figure 6.2. The snapshots are

[2]The numerical solution is calculated in a system of reference moving with the plate, this means that the transport acceleration has to be taken into account as an external force. As two successive derivations produce a very noisy signal (see dots in the acceleration plot of figure 6.2), the displacement has been smoothed with a low pass filter before differentiating it.

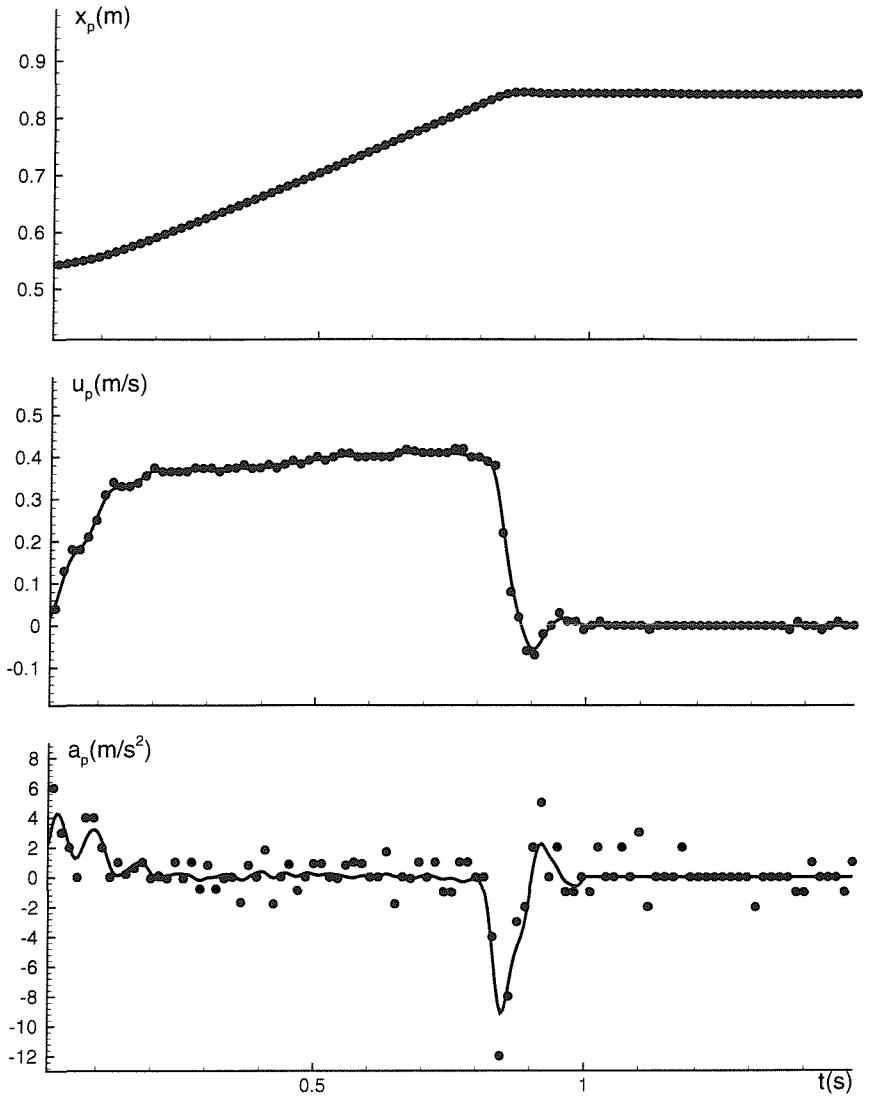

Figure 6.2: Time history of the displacement x_p, velocity v_p and acceleration a_p of the vertical plate. The dots represent the experimental data, the solid lines the values used in the numerical calculation.

ordered from left to right and from top to bottom with the time increasing from 0.128s with an increment Δt=0.128s. The white lines represent the numerical results[3] and they are superimposed on the black and white experimental pictures[4].

[3]A stretched mesh has been used to discretize the flow, close to the plate the mesh is uniform and $\Delta x = \Delta y = h/45$, the time step is $\Delta t = 8 \cdot 10^{-4}$s

[4]The Powerpoint software was used to sumperimpose numerical and experimental pictures. The background of the numerical results was set transparent. The size of the two pictures was changed and the images translated so that a reference segment would result superimposed in the two pictures.

The overall evolution of the free surface is well captured by the numerical results.

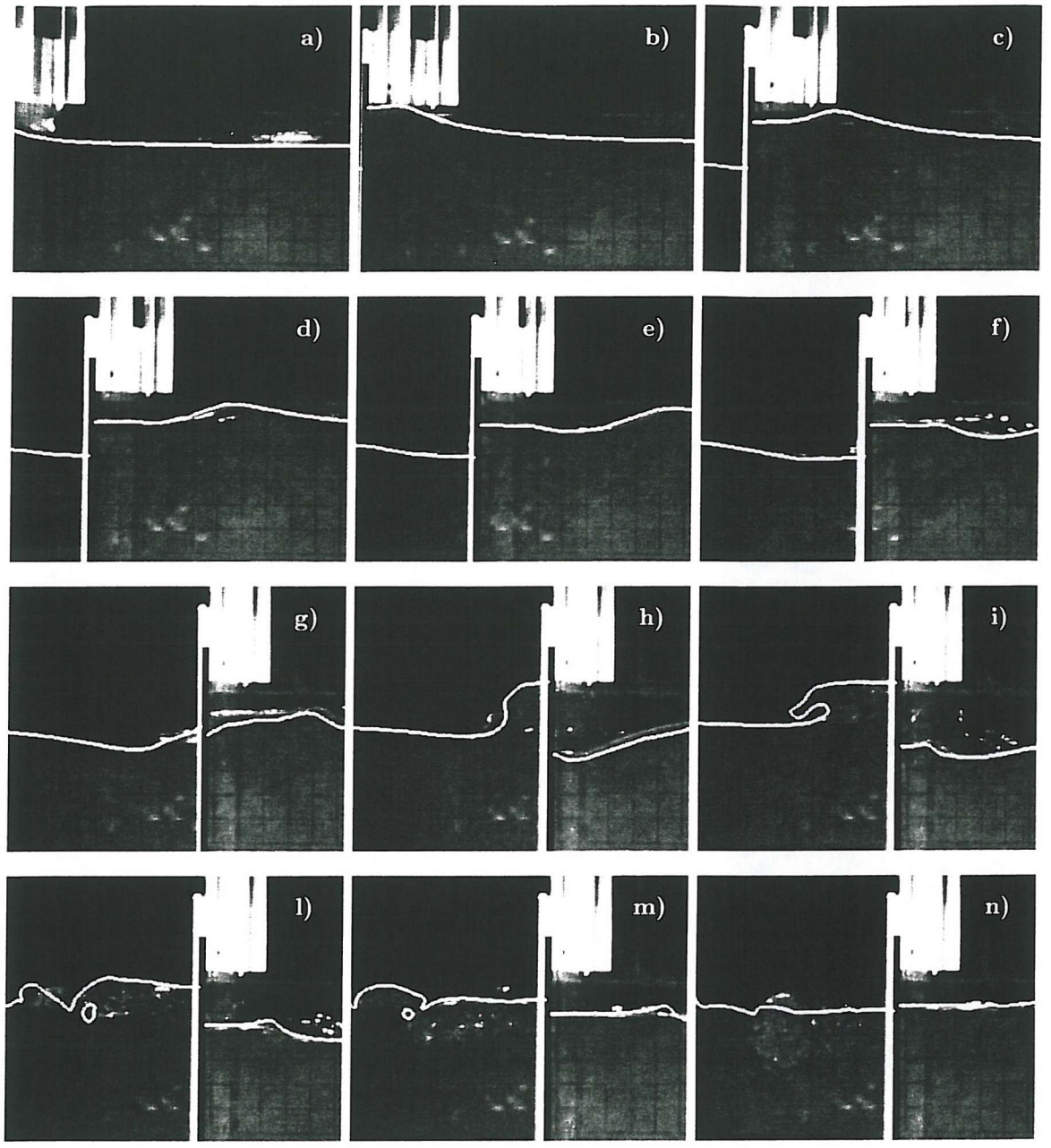

Figure 6.3: Deformation of the free surface: comparison between numerical and experimental results. In each plot, the black and white background is the experimental video-image of the free surface deformation on one of the glass sides of the tank, the white line the numerical free surface. The snapshots refer to the times a) t=0.128s, b) t=0.256s, c) t=0.384s, d) t=0.512s, e) t=0.640s, f) t=0.768s, g) t=0.896s, h) t=1.024s, i) t=1.152s, l) t=1.280s, m) t=1.408s and n) t=1.536s. The grid on the experimental pictures presents a mesh size of 3cm both in the x and y directions.

When the plate starts to move the free surface on the front side deforms more than on the back. On the right side (see figure 6.3), the plate behaves as a wavemaker and causes the formation of a wave that moves from left to right with a velocity $u = 0.55\text{m/s}$ relatively to the plate itself. The development of this wave can be observed from figure 6.3-a to 6.3-e.

On the back of the plate the body motion causes a depression that sucks down the air water interface. The drop of the air-water interface is not sufficient to cause its interaction with the vorticity that is forming at the bottom edge of the plate. And in that case, the vorticity at the bottom of the plate is quite weak because the velocity is slow.

When the plate stops (see figure 6.3-g) some differences between numerical and experimental results appear. The numerical free surface in the front region is quite different from the experimental one, while no difference can be noted at the back of the plate. Figure 6.3-g refers to t=0.896s when the plate is stopping and u_p is reaching its lowest negative value. At this time the numerical velocity is lower than the experimental one as a an unfortunate consequence of the smoothing (see figure 6.2). As already shown for other cases, sufficiently small differences in acceleration and velocity can cause different angles of the water surface leaving the front of the plate. Moreover, it is to be noted that from t=0.87s to t=1.2s the experimental plate rotates slightly around the upper hinge of the carriage (see section 5.4). Apart from the small differences in velocity, these oscillations can be the cause of the disagreement between numerical and experimental results in figure 6.3-g.

The differences decrease as the time goes on.

Both numerical and experimental results show a second wave leaving the right side of the plate in figures 6.3-f and 6.3-g. A third wave forms in the front of the plate after it has stopped (see figure 6.3-i to 6.3-m), and a larger difference between the two data sets is visible here. The crest of the experimental wave is smaller than the numerical one. The detected local discrepancies are probably due to the quite small wave amplitude involved, so that the mesh used in the numerical simulation[5] is not sufficiently fine to capture correctly the wave deformation.

At the time at which the plate stops, there is a large deformation of the interface at the back of the plate. The inertia of the water causes its rise and fall under gravity, forming a plunging breaker (see figure 6.3-h to 6.3-l). The plunging

[5]The mesh used in the numerical calculation is characterized by Δx=Δy=$h/45$, while the $\Delta t = 8 \cdot 10^{-4}\text{s}$

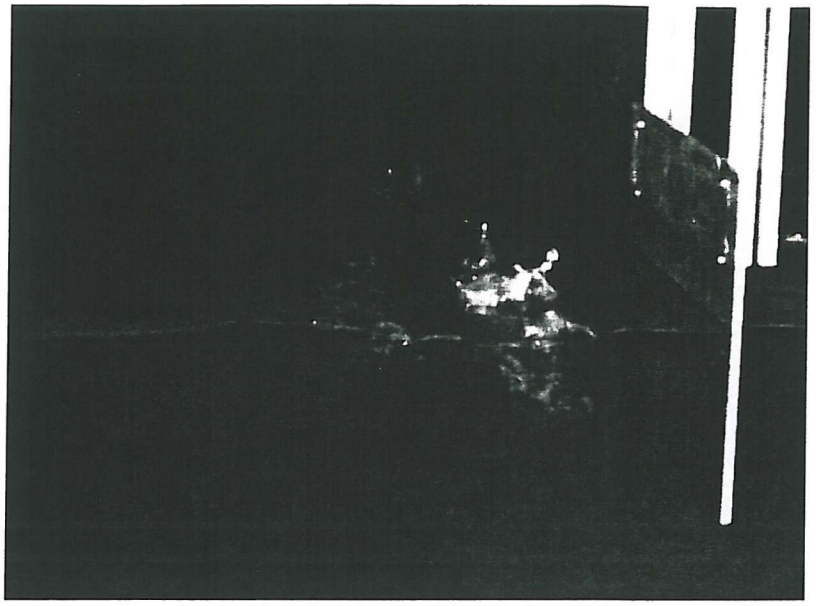

Figure 6.4: Top-side view of the free surface after the wave breaking, t = 1.625s. Three dimensional effects are visible.

jet re-enters the water in figure 6.3-l. The agreement between numerical and experimental results is good both in the formation of the plunging jet and in its breaking. Moreover the numerical and experimental data show a similar behaviour of the splash up. The water first rises and then falls, forming two jets one on the left and one on the right as shown in figure 6.3-m. These two jets form two successive splash-up events (see figure 6.3-n). Some differences between numerical and experimental data are visible in the right splash up. Figure 6.4 shows the water surface at time t=1.625s as captured by a video-camera tilted and moved above the flume. It shows that three dimensional effects develop after the breaking. So the differences referred to in figure 6.3-n are mainly due to these effects.

6.1.2 Evolution of pressure and vorticity after the breaking

In the case analysed no aeration is present at the lower tip of the plate. This prevents the vortical region that develops at that point from being tracked in the video images. Instead, some vorticity (see figure 6.5) is detectable in the breaking region. In particular the two counter-rotating vortices, generated after the backward breaking, form a vortex pair moving downwards and toward the plate. The two vortices are characterized respectively by a clockwise rotation on the left and an anticlockwise rotation on the right. Therefore their mutual action induces a

downward motion. As the right vortex is more intense than the left one, the pair moves also to the right.

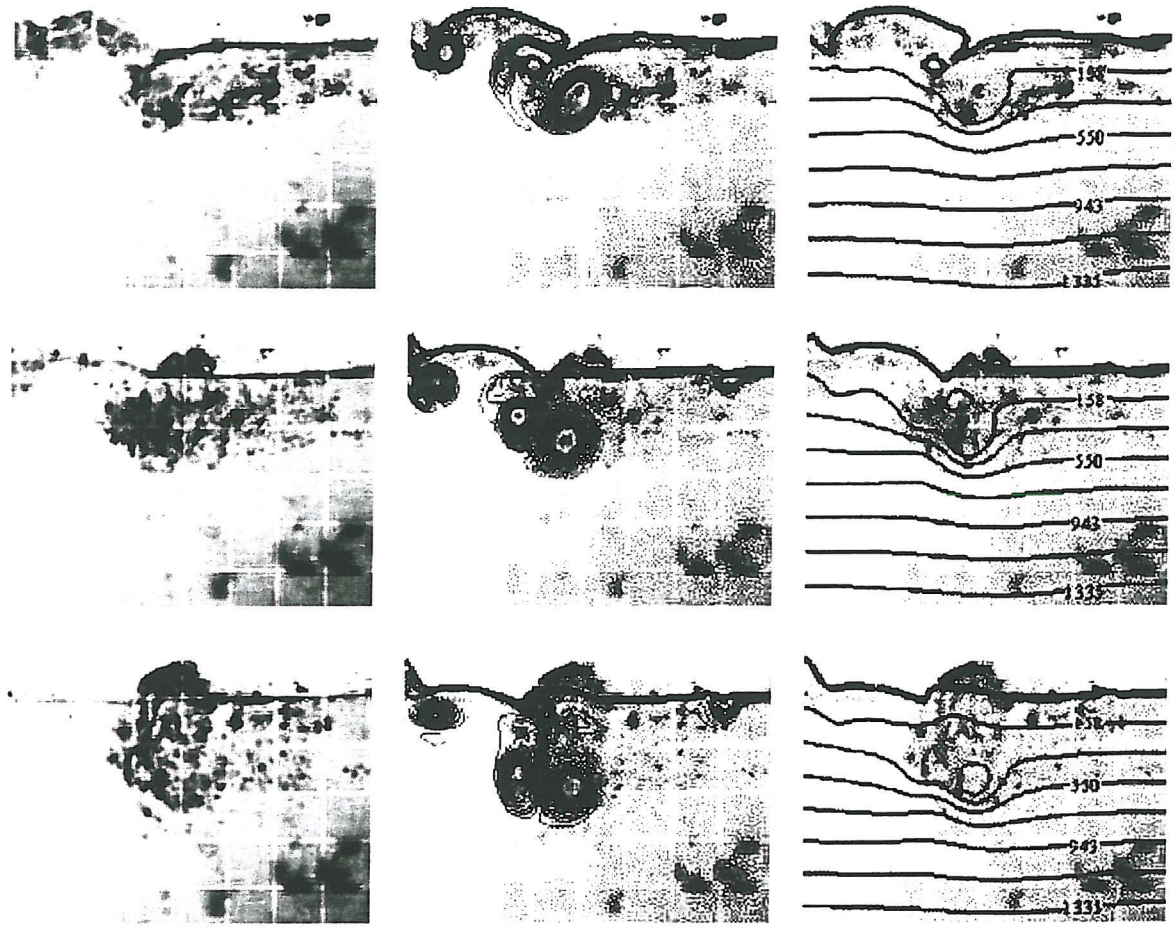

Figure 6.5: Bubbly regions formed where the backward breaking impacts. The bubbles concentrate in the vortical zone. Left: Experimental images; centre: vorticity contours superimposed on the images and right: pressure contours superimposed on the video images. The figures refer to the left side of the plate at the times t=1.408s, 1.472s and 1.536s.

In figures 6.5 and 6.6 the splash up on the left side of the plate and the successive phenomena developing are analyzed. In those figures the vorticity, and pressure contours are superimposed on the experimental images respectively in the centre and on the right. The time increases from top to bottom and the snapshots refer to the times t = 1.408s, 1.472s, 1.536s, 1.60s, 1.664s and 1.728s.

The vortex cores are characterized by low dynamic pressure (see appendix B). In the upper part of the vortices, this causes pressure gradients opposite to the hydrostatic pressure gradients, trapping any bubbles that occur in this region (see

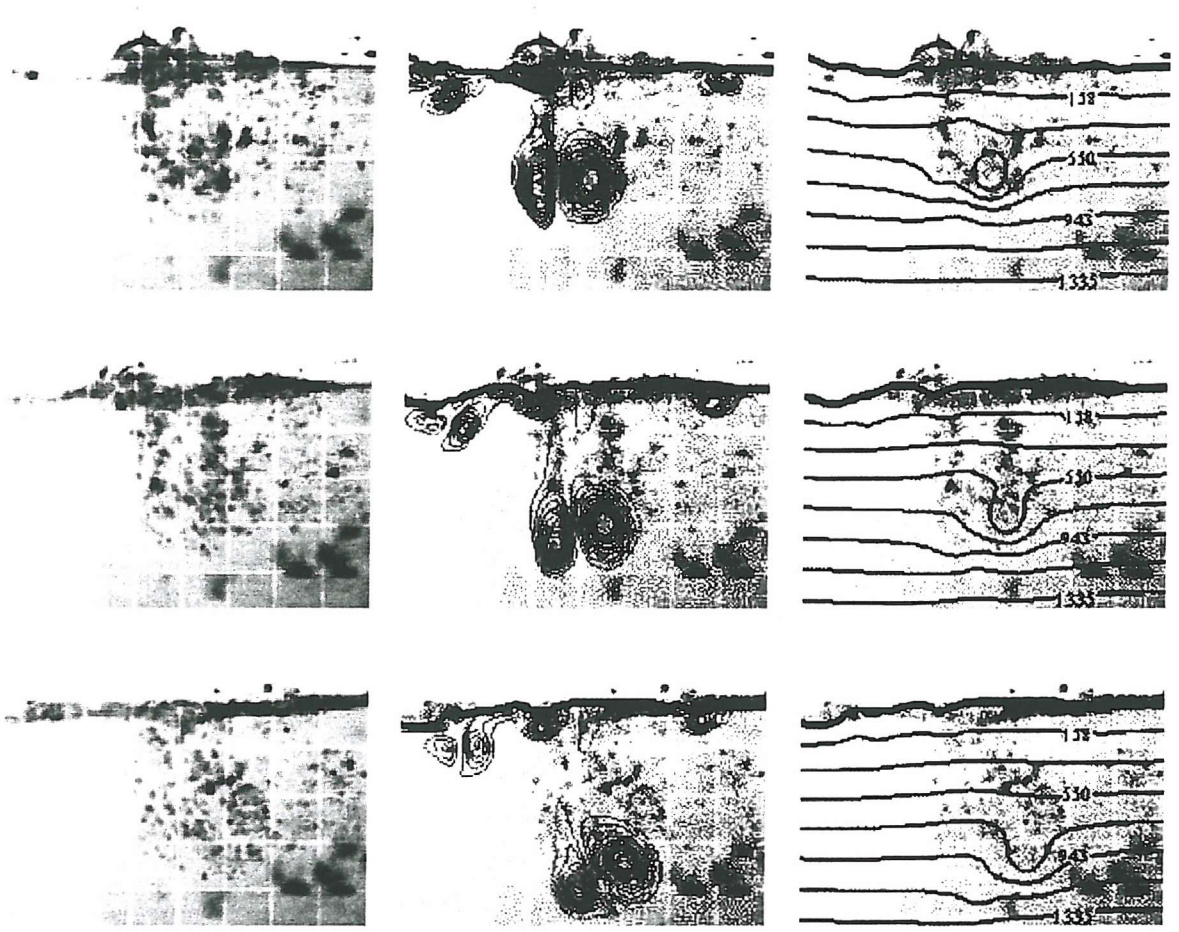

Figure 6.6: As for figure 6.5. t= 1.60s, 1.664s and 1.728s.

Appendix B). Therefore, when the vortex cores that are generated after the splash up move downwards, the low pressure areas associated with them bring the bubbles down as well. In the centre of figures 6.5 and 6.6 the lower boundary of the bubbly region (the bubbles appear as dark dots in water) corresponds roughly to the most curved pressure contours.

As the vorticity is moving downwards it is diffused by viscosity, consequently the regions of low dynamic pressure decrease in size and intensity. As a result the buoyancy plays a more important role for a larger number of bubbles that leave the high vorticity region as a kind of wake behind the vortex centres.

LDA measurements were not performed in this region. However, it is sensible to think that the presence of bubbles would have produced rather scattered values of velocity. So, these measurements would have been of little use in the calculation of the vorticity. PIV (particle image velocimetry) is a much more suitable

technique for the measurement of this quantity. Even this technique is not free from errors of measurements in the bubbly region because of the light scattering. Only recently new PIV techniques have been introduced for multi-phase flows. Namely the DDPIV (defocusing digital particle image velocimetry) detects the presence of bubbles and their velocity (Pereira & Gharib, 2002) in a 3D environment and the PIV with LIF (laser induced fluorescine) (Grunefeld *et al.*, 2000) is able to measure the velocity of a two-phase flow.

6.1.3 The velocity field

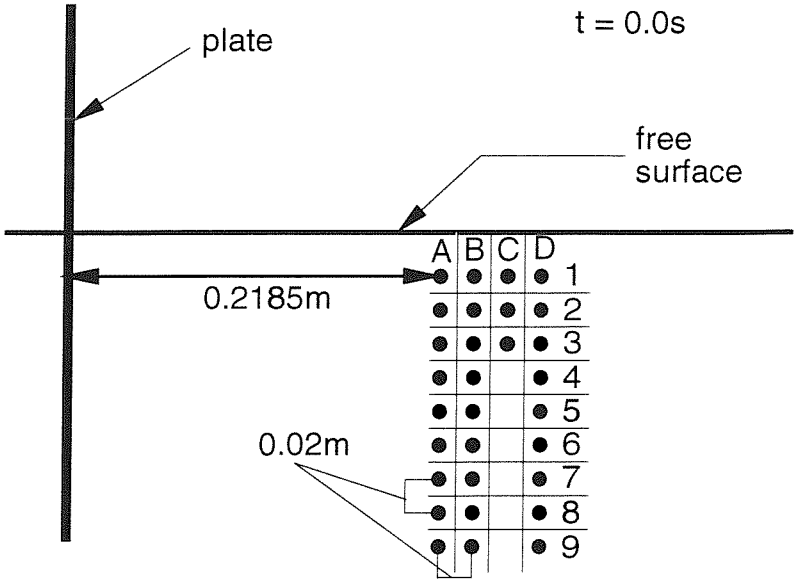

Figure 6.7: Sketch of the arrangement of the LDA measurement points and of their labelling. The capital letter indicates the column, the number refers to the row. At time t=0.0s the most left point is at a distance of 21.85cm from the plate. The spacing between the points both in the vertical and the horizontal direction is constant and is equal to 2cm.

During the experiments velocity measurements were performed by means of LDA. The data are collected at discrete points displaced onto four vertical columns and nine rows (see figure 6.7). In the third column, only the upper three points are shown because practical difficulties prevented reliable measurements elsewhere. The points of measurement are spaced by 0.02m both in the vertical and horizontal directions with the upper point located 0.026m below the free surface and the most left point 0.2185m distant from the initial position of the plate. In

figure 6.7 there is a sketch of the relative arrangement of the points, together with their labelling. Each point is labelled with a capital letter indicating the column and a number referring to the row.

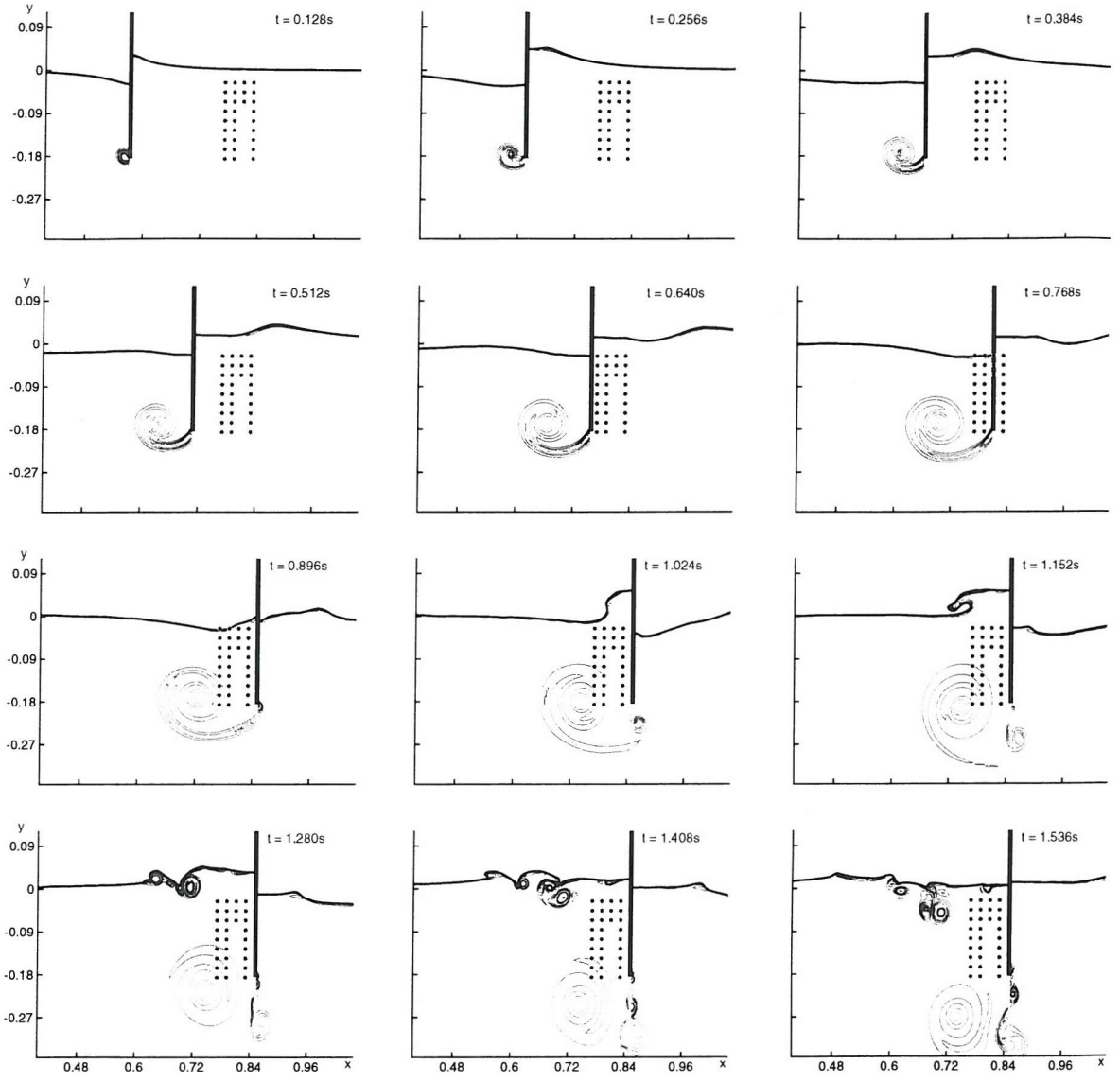

Figure 6.8: Numerical evolution of the free surface and of the vorticity. The dots represent the locations where the velocity is measured experimentally. The still water depth was 0.7m.

The LDA apparatus was fixed in the laboratory, so that the measurements are at points whose distance from the plate varies in time. For a clearer understanding of the development of the velocity, the relative position of the points with respect to the plate is plotted in figure 6.8. There, the evolution of the numerical free surface and of the numerical vortical region are also shown.

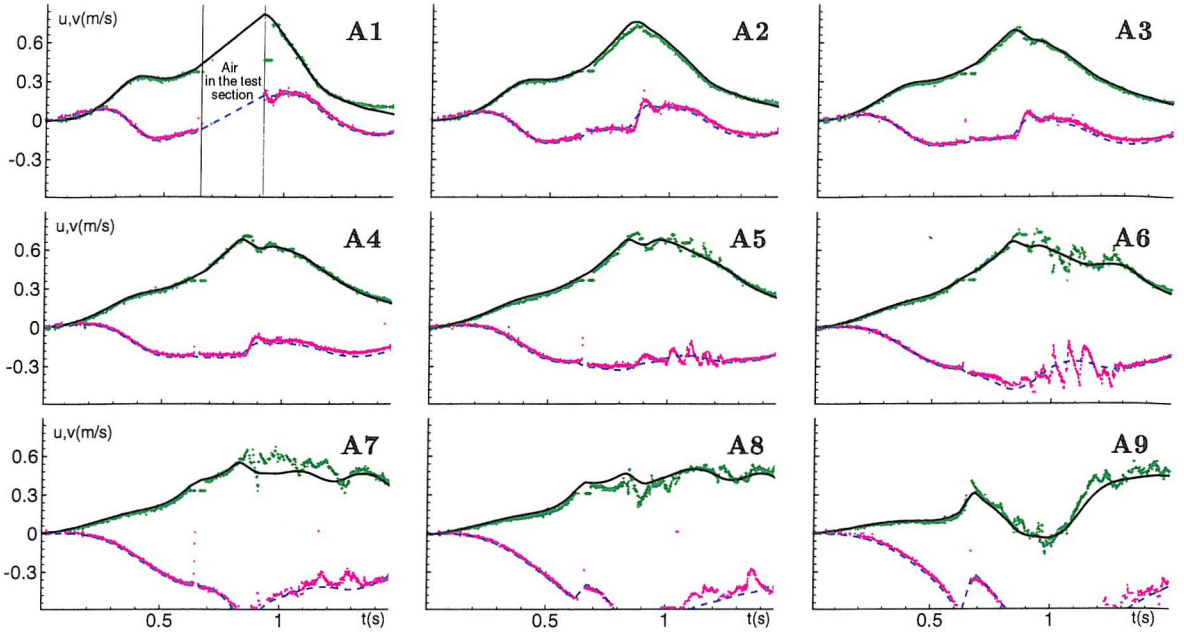

Figure 6.9: Velocity in column A of figure 6.7. The symbols represent the experimental measurements, the solid black lines and the dashed blue lines represent respectively the numerical u and v components of the velocity.

Figures 6.9 shows a comparison between the numerical and experimental velocities for column A. The green and purple symbols represent respectively the horizontal, u, and vertical, v, experimental components of the velocity, while the black solid and blue dashed lines represent their numerical counterparts.

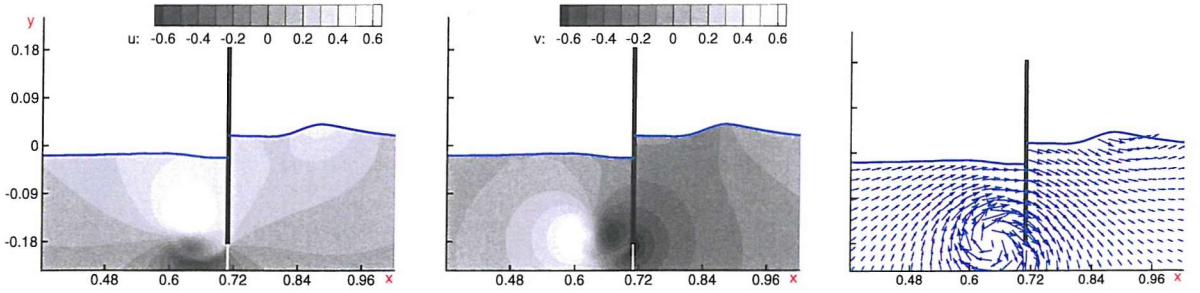

Figure 6.10: Numerical velocity field at t=0.512s. On the left: horizontal velocity contours in water; in the centre: vertical velocity contours; on the right: velocity vector field.

The overall agreement is quite good, with larger discrepancies between the different data when the plate stops ($t \simeq 0.9$s).

The points of measurement in column A are initially at a distance of 21.85cm from the plate; this means that their horizontal velocity smoothly increases from

zero to the velocity of the plate u_p as the latter comes closer.

Concerning the vertical component v, the lower five points of the column (A5-A9) present a negative and decreasing value of v because the fluid at the points is diverted below the plate by its motion. The upper four points (A1-A4), instead, present an initial positive and growing v component. The water at those points is diverted upwards by the plate motion and contributes to the creation of a first wave on the right side of the plate (see figure 6.8). When the first wave detaches from the plate on the right and goes over the measurement points, the upper three rows A1, A2 and A3 present a local maximum in the horizontal component of the velocity and an almost simultaneously zero value of the vertical velocity. The local maximum of u and the zero of v are perfectly synchronized on the crest of the wave but the flow field is disturbed below the free surface, concealing this syncronicity. Because the points are well below the interface, they are affected by a distorted field as shown in figure 6.10.

As the wave passes the measurement points, v assumes negative values. In fact, the measurement points enter the region of influence of the lower tip of the plate. There, most of the fluid is diverted below the plate. The closer the point is to the lower tip, the higher is this effect and, consequently, the larger is the negative value assumed by v. Because of this behaviour, before the plate crosses the test section, the minimum value reached by v decreases from point A1 to point A9.

When the plate crosses the test section A at time $t_{crossing} = 0.64s$, the experimental velocity shows a constant value of u. This value is equal to 0.37m/s and it coincides with the velocity of the plate at the moment it crosses the test section area[6]. It is the result of an error in the measurements generated by the reflections of the laser beam on the plate (see section 5.4).

At the same time, a small jump appears in the vertical velocity, due to the passage of the measurement point from one side of the plate to the other. This jump is not large except that at point A8. Because no major deformation of the free surface alters significantly the flow field at either side of the plate (see figure 6.10), points A1-A7 present small discontinuities of the v component of the velocity (see figure 6.10).

Point A8 is at y=-0.163m. When the plate has just passed the test section, it is very close to the lower tip, where a region of detached flow is present. This causes

[6]This constant value results longer than the time s/u_p (s is the thickness of the plate and is equal to 5mm).

a significantly lower vertical velocity component.

Point A9 presents a behaviour similar to A8 but a larger jump in v. This point is below the lower tip of the plate. And the related velocity jump is due to the passage of the vortex sheet past the measurement point.

A vortex sheet is characterized by a rapid change of velocity across it (Saffman 1992). The discontinuities presented by u and v in point A9 at time t=0.66s occur exactly when the vortex sheet passes. The jump in the v components at those points is about 0.3m/s and is well captured by the numerical results.

After the time of crossing, $t_{crossing}$, the upper seven points A1-A7 present an increase of the horizontal velocity. They are in the upper and right part of the vortex released at the lower tip of the plate (see figure 6.8); this means that a positive velocity contribution due to the vortex is added to the velocity of translation of the plate.

Point A8 presents a different behaviour because it is in the region of detached flow; here no substantial increase in the velocity is detected.

Point A9 presents a cusp in the horizontal velocity due to the vortex sheet; this is captured by the numerics although the numerical results appear more smoothed.

When column A has passed from the right side of the plate to the left, point A1 presents a gap in the data.

The gap is common both to the numerical and to the experimental results and it is due to a local water level lower than $y = -0.023m$.

When the plate stops almost abruptly at t=0.9s, both the vertical and the horizontal components of the velocity show a jump. At t=0.9s column A is on the left side of the plate, where the inertia of the water causes it to flow towards, and impact on the plate. This flow develops into a plunging jet that eventually impacts on the free surface again. The points in column A are too far away to record the effects of the breaking but for a change in the slope of the velocity components. When the plate stops the whole volume of water near the surface on the left of the plate is swept upwards. This causes the formation of a jet along the plate. When the effects of gravity overcome those of the fluid inertia, a plunging jet forms.

The water that is pushed upwards partially feeds the developing plunging wave (see left and centre plots of figure 6.11) and partially falls directly under the action of gravity. When the flow at the measurement points is not involved in the feeding of the jet, a point of maximum curvature is observed in the fluid velocity.

In figure 6.11 this behaviour is analyzed for point A1. This location is crossed

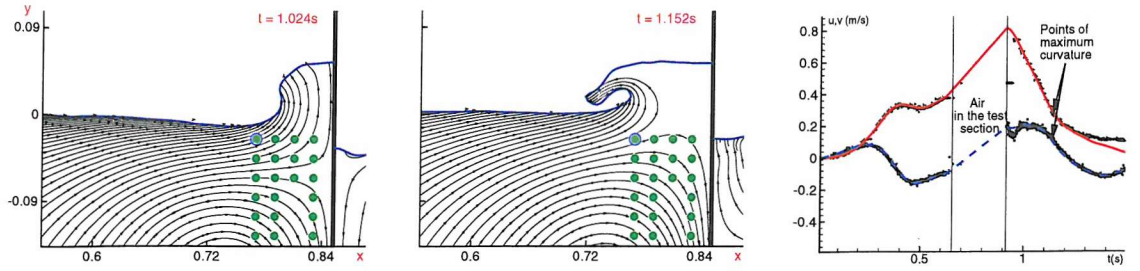

Figure 6.11: Plunging jet formation: numerical streamlines at t=1.024s and t=1.152s and velocity history in A1. At the former time the streamlines, going through A1, A2, B1 and B2, flow into the jet. At the latter time they are flowing downward. This causes a point of maximum curvature in u and v.

by the water going into the jet up to t=1.15s (see the left and central plots of the figure). At that time the streamlines start to be directed towards the lower tip of the plate. As a result, both A1 horizontal and vertical velocity records have a maximum value of curvature, much more evident in the horizontal component (see right plot of figure 6.11). The same happens for point A2.

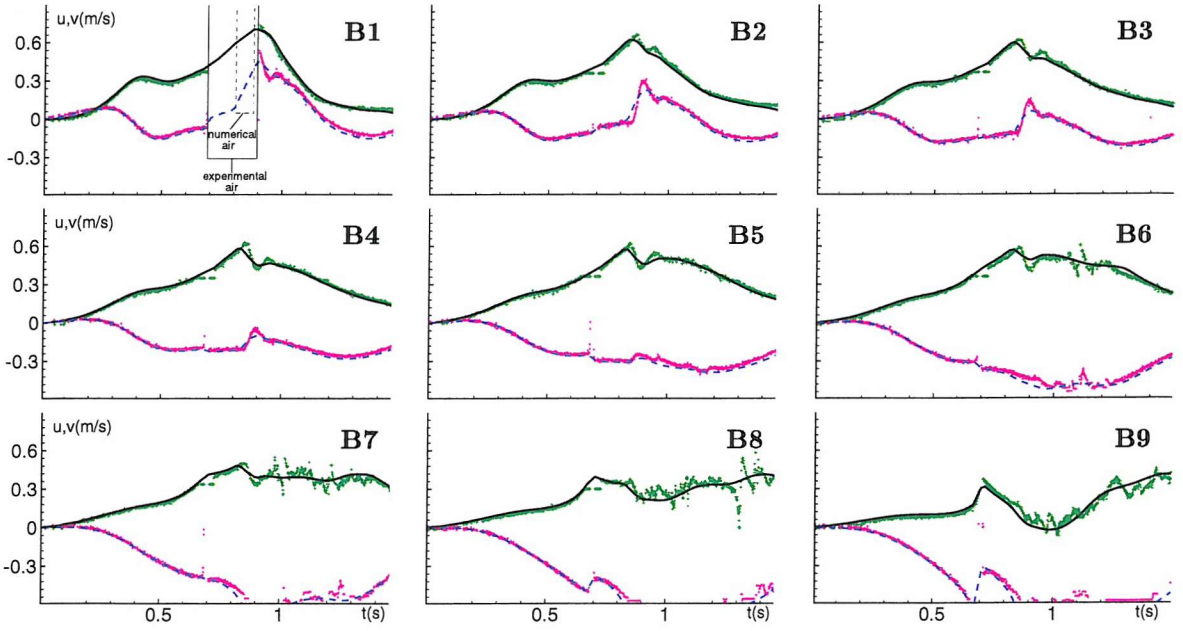

Figure 6.12: Velocity on column B of figure 6.7. The solid line and the dashed lines represent respectively the numerical horizontal and vertical velocity components. The symbols represent the experimental measurements.

After the stop, the points on column A are crossed by the vortex sheet. When this occurs, some oscillations appear in the measured velocities. The link between the passage of the vortex sheet and the oscillations can be deduced from figures

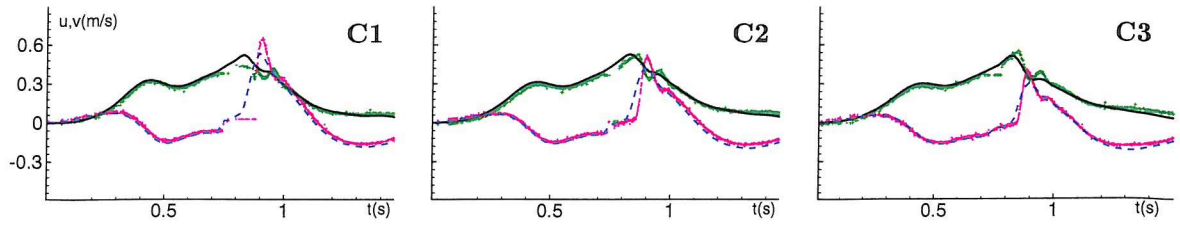

Figure 6.13: Velocity on column C of figure 6.7. The solid line and the dashed lines represent respectively the numerical horizontal and vertical velocity. The symbols represent the experimental measurements.

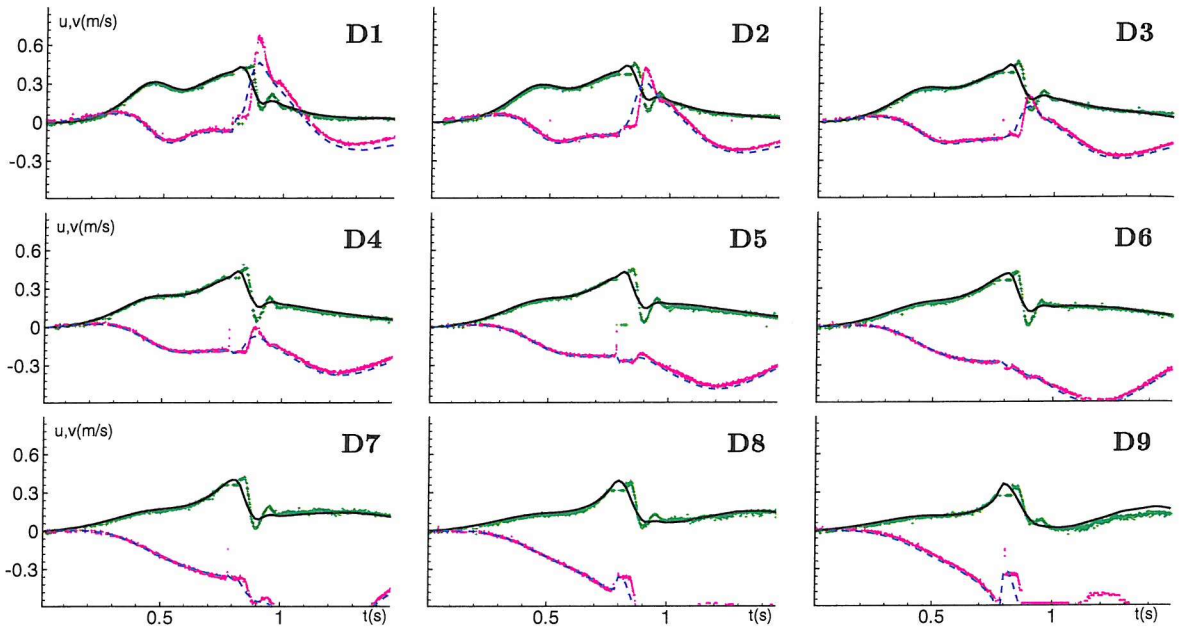

Figure 6.14: Velocity on column D of figure 6.7. The solid line and the dashed lines represent respectively the numerical horizontal and vertical velocity. The symbols represent the experimental measurements.

6.9, 6.12 and 6.8. The oscillations appear at the same time as the contours of strong vorticity arrive at the measurement points. However, these oscillations are not present in the numerical calculation, and the reason for their absence is not clear. Considering that no bubble is present in the flow (at least within the resolution of the video camera), and that the frequency of the oscillation is low enough to exclude effects of turbulence, three possible explanations can be given. First, the vortex sheet is unstable, generating side vortices velocity oscillations. Koumoutsakos & Shiels (1996) show that a plate accelerating in an incompressible fluid can create an unstable vortex sheet. The velocity of the plate analyzed here is subject to a phase of acceleration, potentially responsible for the instabilities in

the vortex sheet. If this is the case, it is likely that the numerical calculations do not capture the oscillations because the mesh is not sufficiently refined around the lower tip of the plate.

A second explanation comes from the comparison between the numerical and the experimental velocity jumps at point A9. The measured vertical velocity jump across the vortex sheet is captured well numerically in figure 6.9-A9, but the corresponding cusp in the horizontal component is smoothed by the numerics. If a similar smoothing occurred in smaller jumps, the numerics would not reproduce the oscillations in the horizontal velocity.

The rotation of the plate around the upper hinge is a further possible explanation. The amplitude of this oscillation is large enough to cause the displacement of the vortex sheet and consequently to cause the abrupt changes in velocity.

There is no means here to state with confidence which one of these possibilities is most likely, and they are probably combined in reality to give the results shown in figures 6.9 and 6.12.

It was not possible to continue the experiments, but a straightforward way to check if the oscillations are related to flow instabilities would be to spread a viscous layer of fluorescine on the plate surface. This would be released gradually during the motion revealing the presence of any instabilities.

All the comparisons between experiments and numerics are carried on up to t=1.5s. Later the experimental points close to the breaking are very much affected by the 3D development of the flow field. This creates major differences between the numerical and experimental measurements.

The phenomena developing in column A are reproduced in a similar way in the other columns B,C and D. The comparison between numerical and experimental velocity in column B are shown in figure 6.12. The overall comparison results are good. One of the main differences between the two sets of data is the duration of the time interval characterized by the presence of air at B1.

The air is present at the point for a time longer in the experiments than in the numerics. At t= 0.768s, when air is observed experimentally and not in the numerical results, figure 6.8 shows that the free surface is very close to the measurement points. Therefore, both errors in the numerical predictions and in the experimental estimation of the position of the point B1 can explain the disagreement.

Other differences appear when the plate stops. The smoothing of the plate velocity u_p used in the simulation causes a smoothing of the steep velocity gradients appearing at t=0.9s. As for column A, oscillations are present in the experimental results when the rolled up vortex sheet crosses the points of measurement,but they are smoothed out by the numerical computations.

Figure 6.13 shows the comparison for the velocities in column C. The agreement is again good but for an underestimation of the velocity jump at the stopping point.

The same considerations are valid for column D (see figure 6.14). No oscillation of the velocity appears in this column. In fact it is not affected by the passage of the vortex sheet but for point D9 (see figure 6.8). After t=0.9s, at D9, the velocity exceeds the range of the LDA device (see section 5.4) and comparisons are not possible in the interval of times [0.9s, 1.7s].

It is interesting to note that the velocity jump after the stopping of the plate has an amplitude larger going from column A to column D. At the time t_{stop}, the points in the last column D are the closest to the plate (see figure 6.8) and are more affected by its change in velocity. In particular, at D1 the jump is $v(t^+_{stop}) - v(t^-_{stop}) = 0.8$m/s. The flow that takes place near the plate at this time can, in a very simple model, be thought of as the sum of the flow that exists before the stop, and an equal and opposite motion, similar to that which would be generated by an impulsive start to 0.4m/s.

In such a case the velocity field would adapt itself immediately to the new conditions, with a larger jump in the velocity at the points closer to the plate. The addition of the flow due to the impulsive start would cause a deviation of the upper part of the fluid upwards and of the lower part downwards to circulate around the lower tip of the plate. This is qualitatively what happens in the case analyzed, leading to the formation of new anticlockwise vorticity in the right of the plate (see figure 6.8).

The first five points of column D show positive velocity jumps $v(t^+_{stop}) - v(t^-_{stop}) > 0$, while the others (D6-D8) are characterized by negative jumps. Using the simplified case of an impulsively started current, this implies that the "stagnation point" is between point D5 and D6 (below $y = -0.106$m), *i.e.* it is at an elevation close to half the submergence depth of the plate at t=0.9s.

6.2 Vertical plate at high speed and low submergence

The second set of experiments refers to a higher maximum speed and lower immersion of the plate. In this case, it was difficult to ensure a satisfactory repeatability of the test, and so the motion imposed on the plate was not exactly the same from run to run. This does not mean that the test results cannot be used within a detailed analysis, since for any run the motion history was measured and is known within experimental accuracy.

The related results characterized by high Froude number Fn have been compared with the numerical ones and the interaction between free surface and vorticity has been investigated.

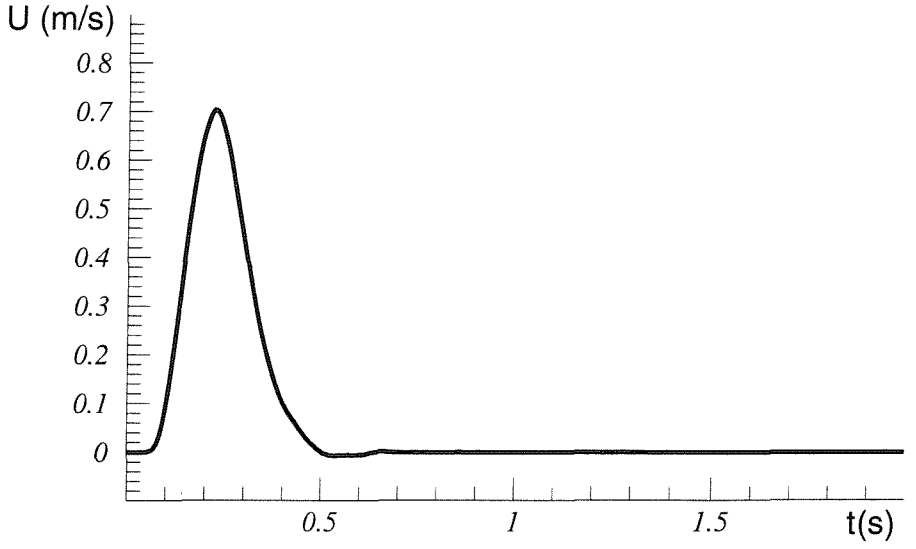

Figure 6.15: Experimental plate: Velocity history, $Fn = 1$.

The test were characterized by an initial submergence h of the plate equal to 0.047m and velocity varying as shown in figure 6.15. The maximum speed of the plate was 0.7m/s and following a smooth variation from the initial rest condition to the final one. These conditions imply a Froude number $Fn = U_{max}/\sqrt{gh} = 1.0$, a Reynolds number $Re \simeq 33000$ and a Weber number $We \simeq 10000$.

The sequence presented in figures 6.16 and 6.17 shows the evolution of the flow field in this experiment. The pictures on the left in these figures are the experimental images, those on the right present the numerical results (a blue line for the air-water interface and coloured contour levels for the vorticity)

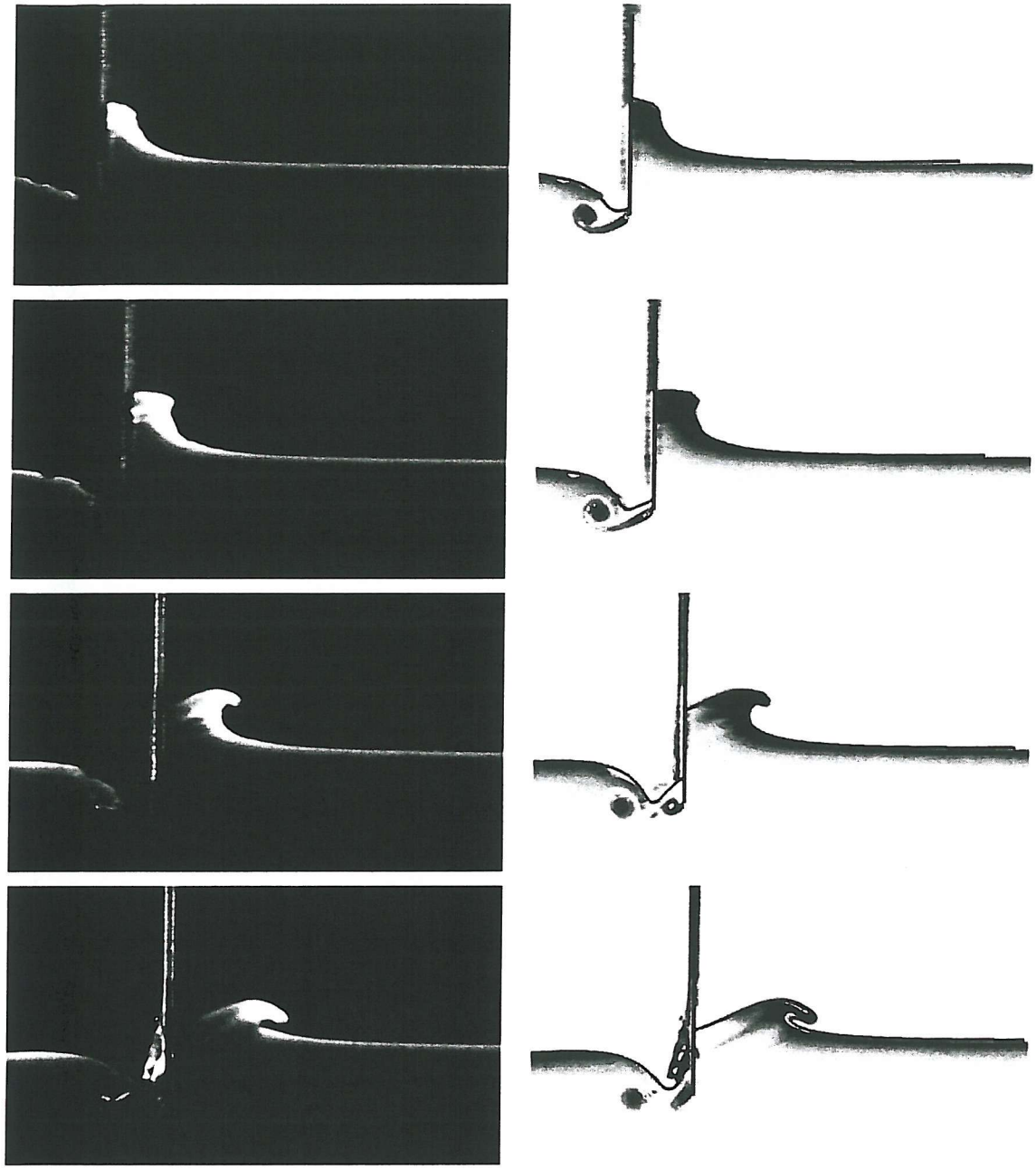

Figure 6.16: Flow field features at $Fn = 1$. On the left: pictures of the experiments. On the right: numerical results (blue line: air-water interface and contour lines: vorticity contours) superimposed on the negative of the experimental images. Times from top to bottom t=0.28s, 0.34s, 0.45s and 0.52s.

superimposed on the negatives of the experimental images. The motion of the plate (from left to right) causes the initial rise of the water level on the right side of the plate and its drop in the left. Here, the velocity of the plate is sufficiently high so that the left part of the air-water interface almost reaches the lower tip of

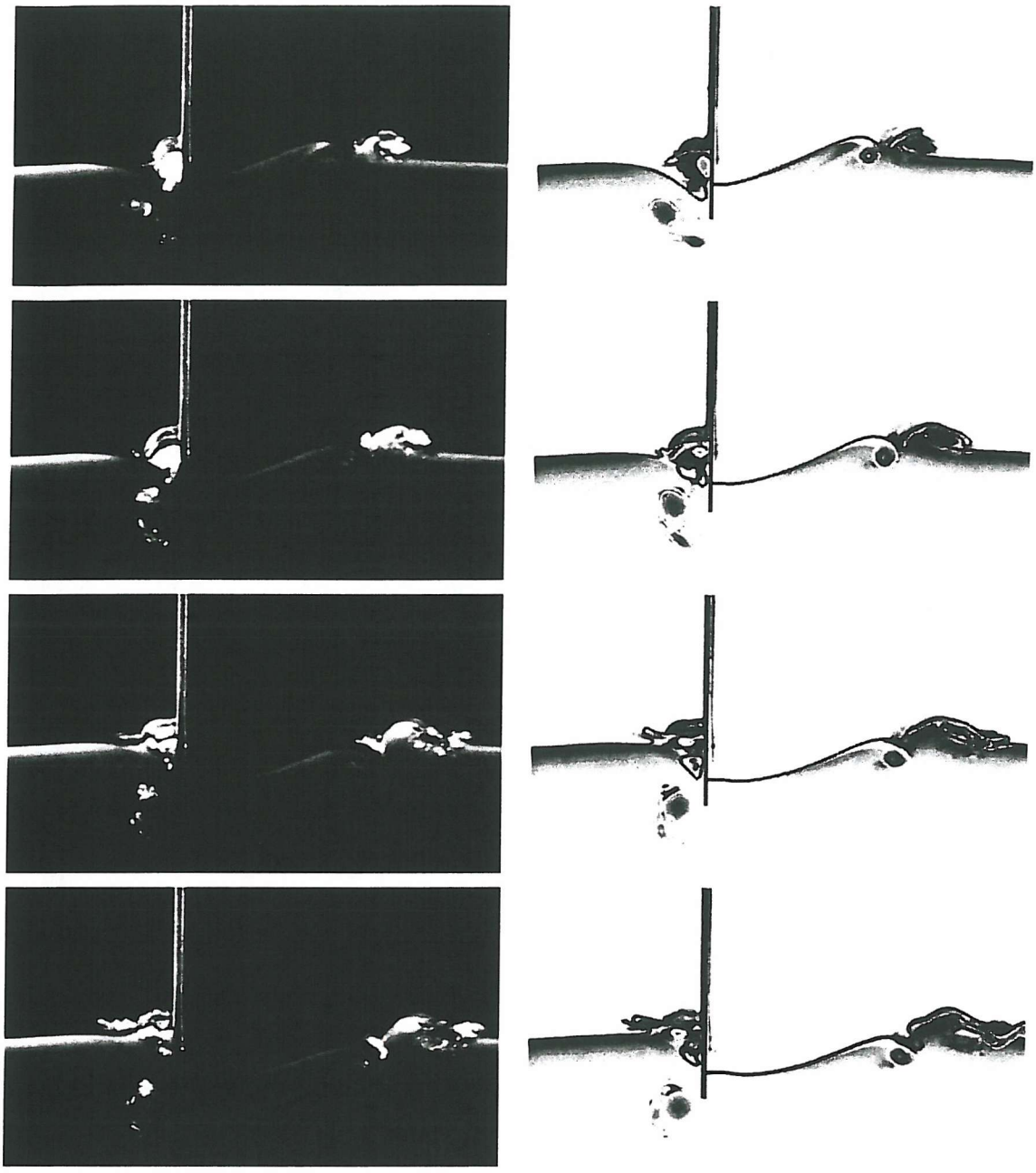

Figure 6.17: Flow field features at $Fn = 1$. On the left: pictures of the experiments. On the right: numerical results (blue line: air-water interface and contour lines: vorticity contours) superimposed on the negative of the experimental images. Times from top to bottom t=0.64s, 0.74s, 0.80s and 0.83s.

the plate (see the first plots of figure 6.16). Meanwhile vorticity is continuously generated at the lower tip and convected downstream. Its presence is highlighted in the experimental pictures by the presence of bubbles entrapped in the vortex cores (see appendix B for a more detailed description of this phenomenon). This

vorticity interacts with the free surface sucking it further down. Simultaneously, on the right hand side of the plate, the effects of gravity limit the water rise and cause the formation of a plunging jet (see the second plots of figure 6.16). At time $t = 0.45$s, a rolling up of the vortex sheet appears together with the formation of a second vortex core, deforming the interface and creating a bump very close to the plate. When the plate stops at $t = 0.5$s the water level on the left hand side rises and forms a second backward plunging, so that at $t = 0.64$s there are two breaking regions, one on each side. That on the right is more energetic than and its first splash up falls down on the underlying air-water interface causing a second splash-up (see the third and fourth plots in figure 6.17).

In the deceleration phase and after the stop, the vorticity is convected towards the plate. It is also pushed downward as shown in section 5.5.

The comparison between numerical and experimental results is satisfactory; the evolution of both the air-water interface and of the vorticity is well captured by the code developed here. The vorticity contour levels are practically superimposed on the bubbly regions. Some difference can be detected between the two sets of data in the deformation of the air-water interface. This could be due to three-dimensional effects developing on the side walls.

6.3 Effects of the stopping phase

The experiments carried out here present three temporal stages. A first phase of start up, a second one of constant velocity and a third phase either of a reverse of the motion or of stopping of the plate. The last phase presents some features that to our knowledge have never been noted before. These are here discussed with reference to sequences in figures 6.18 and 6.19.

The main effects of this stopping are concentrated on the downstream side of the plate (see images of figure 6.18). When the plate stops the flow behind it preserves its forward horizontal velocity. As a result, a certain amount of water impacts against the plate.

The vorticity moves toward the plate also. Depending on the velocity and on the curvature of the velocity time history, the vortices, highlighted by the presence of the bubbles, can be simply convected downstream or interact in a complicated way with the plate.

Image a) of figure 6.18 corresponds to the plate's slowing down phase. Two

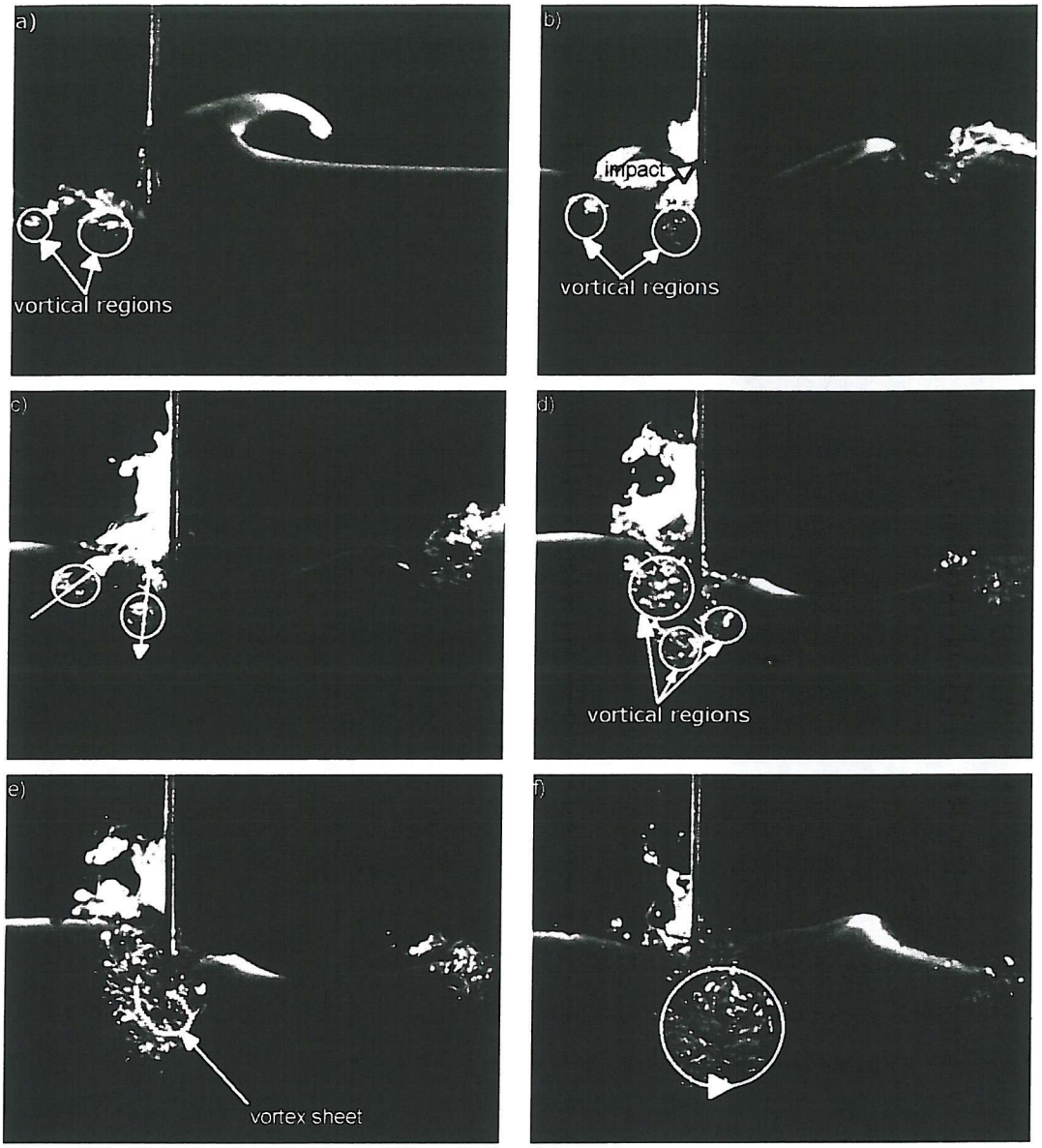

Figure 6.18: Evolution of the downstream vortex regions when the plate stops. The vortex sheet is stretched down and then forward (Fn=1.4).

vortical regions are revealed by the presence of two groups of rotating bubbles. Because of the high Froude number, $Fn \simeq 1.4$, the air-water interface touches the back of the lower tip of the plate and the interface is highly deformed by the vorticity. In image b), the plate has almost completely stopped, the fluid in the right side moves from left to right because of its inertia and impacts against the plate. In part c), after the impact, the vortical regions have different trajectories; the one closer to the plate moves downward, while the other moves forward and upward. In part d), a third vortex is generated, as a result of the water moving

from left to right around the lower tip of the plate. As time goes on, the three vortices, belonging to the vortex sheet highlighted in part e), move around the lower tip of the plate almost in a circular pattern.

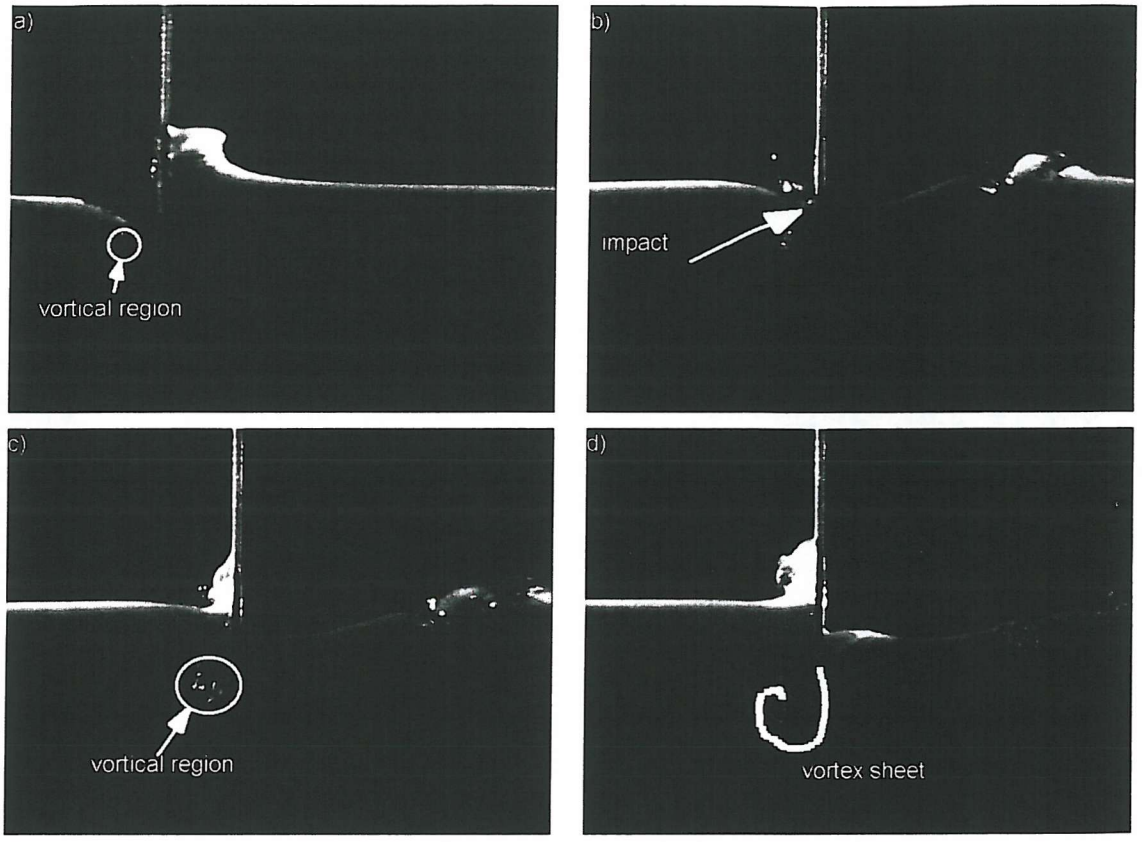

Figure 6.19: Evolution of the downstream vortex regions when the plate stops. The vortex sheet is stretched downward (Fn=0.88).

Figure 6.19 shows the evolution of the free surface for a lower speed, $Fn = 0.88$. In this case the free surface is slightly deformed by the vorticity when the plate stops (see part a) of figure 6.19). At the stopping phase, the downstream flow preserves its horizontal velocity and the rounded side of the free surface impacts against the plate (see part b)). The flow is partially deflected upwards and partially downwards, and the vortex sheet is completely immersed in the fluid moving toward the bottom of the flume (see part c). As time goes on, the velocity discontinuity at the lower tip becomes progressively weaker. This results in a smaller amount of bubbles entrapped and in the impossibility of tracking the vortex sheet in these images. From that instant on, no statement can be inferred about the evolution of the vorticity.

Another effect of the stopping phase is related to the angle at which the

forward jet detaches from the plate.

If the plate slows down well before the water level on the plate has substantially reduced, there is a steep slope at the contact point between the free surface and the plate.

Such behaviour is reproduced in figure 6.20, showing the same time instant for $Fn = 1.23$ and $Fn = 1.4$ respectively on the left and on the right. For the two cases, the same deceleration of the plate motion has been used. Assuming t_{max} as the time instant when the maximum velocity is reached, both plots refer to a time equal to $t_{max} + 0.113U_{MAX}$. The slope of the interface at the contact point is around 30^o, for both Froude number cases.

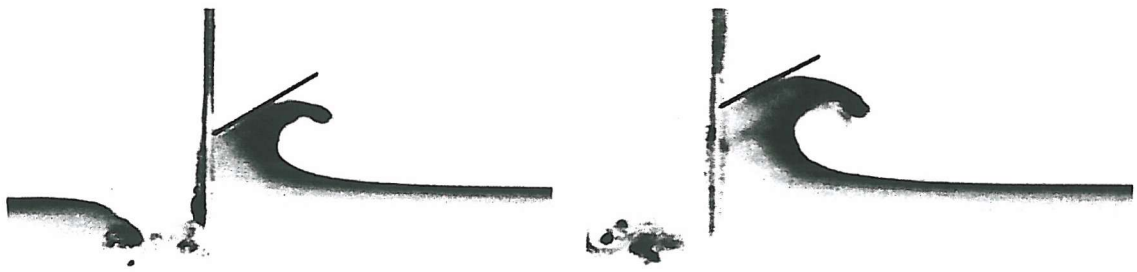

Figure 6.20: Evolution of the interface after the plate has stopped. The tangent at the contact point has a slope of around 30^o. (left Fn=1.25, right Fn=1.4).

6.4 Numerical evolution of the flow field after the impulsive start

Having shown that the comparisons between numerical and experimental results are in good agreement in different conditions, the numerical method is used for a more schematic classification of the problem.

Tsai & Yue (1993) were the first to analyze the problem numerically with an inviscid solver and, using a Kutta condition, to track the vortex sheet emanating from the sharp immersed edge of the plate following a truly impulsive start. Tsai *et al.* accounted for vorticity free shear layers and boundary layer and solved for the potential flow outside the boundary layer and free shear layer. They identified the presence of three regimes for the interaction between the free surface and the

vortex sheet: a *subcritical* regime, $Fn < 0.7$, where no significant interaction between a single branched spiral vortex and the interface occurs before breaking occurs; a *transcritical* regime, $0.7 < Fn < 1.0$, where the free surface stretches the vortex sheet, causing its roll up, even though the interaction is limited; a *supercritical* regime, $Fn > 1.0$, where the vorticity significantly affects the free-surface motion.

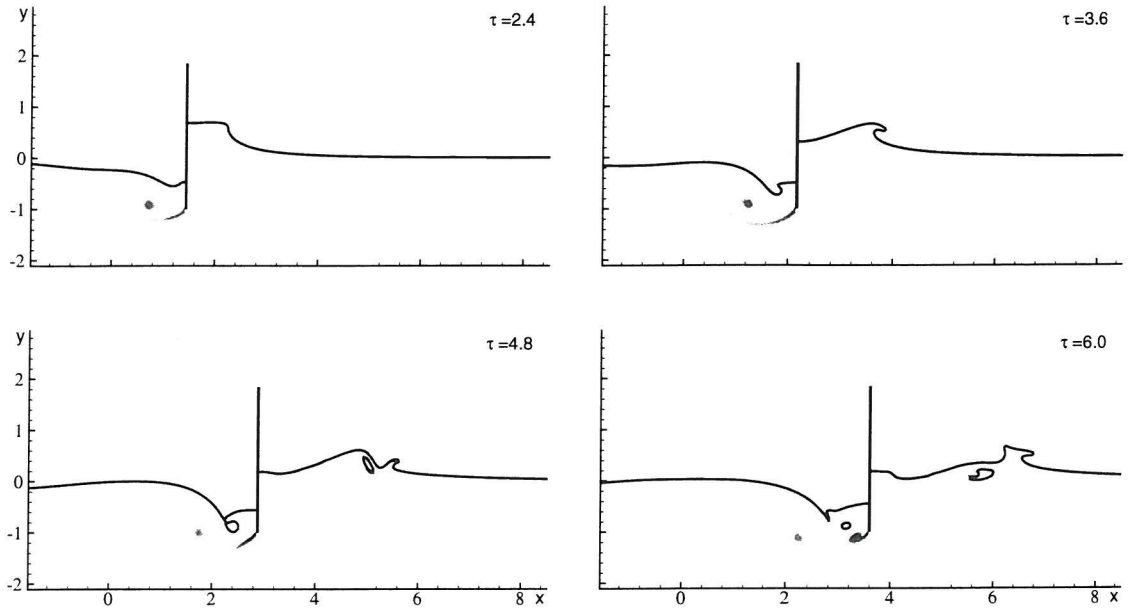

Figure 6.21: Interface and vorticity field in water for Fn= 0.6, $\tau = t/\sqrt{g/h}$.

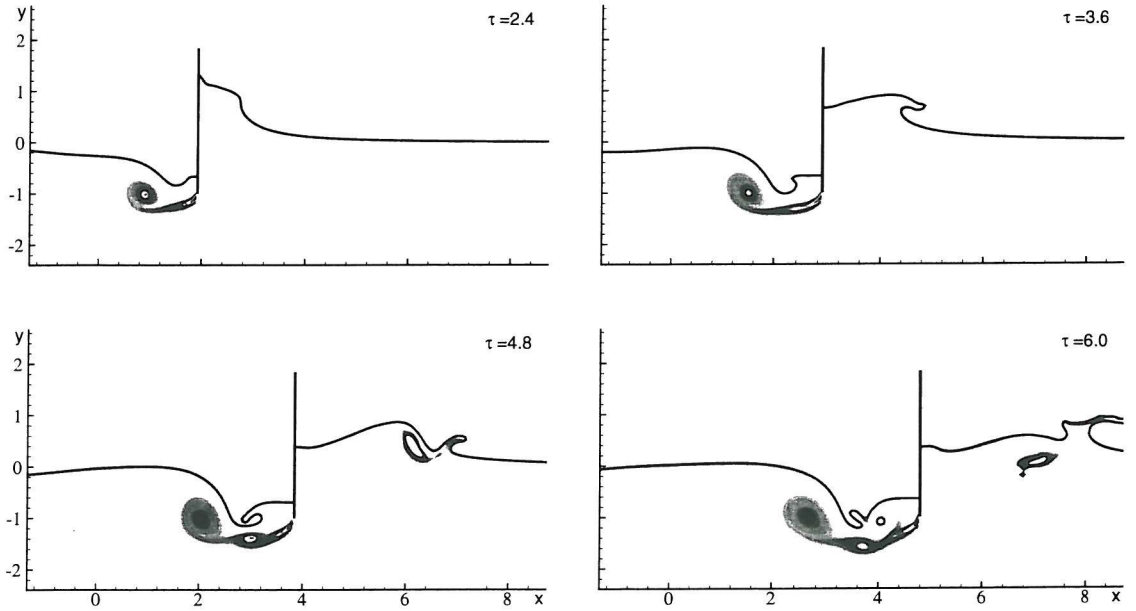

Figure 6.22: Interface and vorticity field in water for Fn= 0.8. (τ = 0.45, 2.7, 4.68, 5.67).

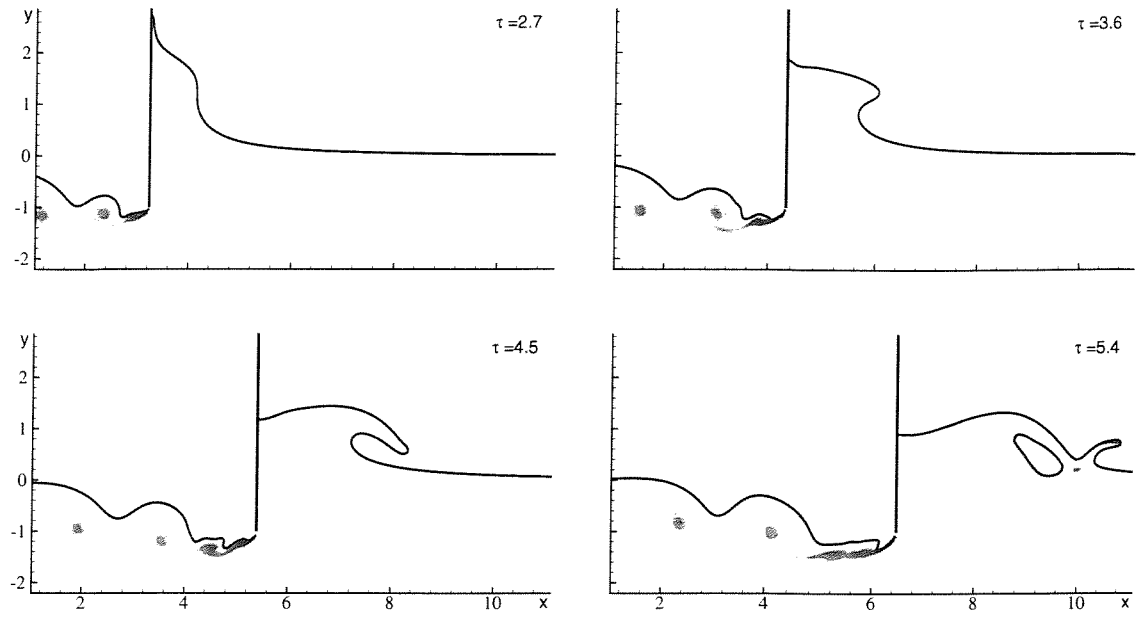

Figure 6.23: Interface and vorticity field in water for Fn= 1.2.

Figures 6.21, 6.22 and 6.23 show the evolution of the free surface and of the vorticity at Froude number respectively 0.6, 0.8, 1.2[7]. They were computed with the present method[8], and represent the evolution of the flow in each of the three regimes described in Tsai & Yue (1993). For the pre-breaking regime, the results shown here are consistent with findings described there. In addition, the present numerical method can be used to investigate further the viscous features of the vorticity-interface interaction and, above all, the post-breaking evolution. Results in figures 6.21 and 6.22 show the stretching and the successive roll up of the vortex sheet, even at low Froude number, after the backward breaking in the right of the plate. In the subcritical regime, the vortex sheet is not single branched any more after the breaking event, even though its influence on the free surface deformation is limited. The threshold Froude number between subcritical and transcritical regimes has to be lowered down to 0.45, where no backward breaking is sufficiently close to the vortex sheet to stretch it.

Practically the critical Froude number corresponds to the limit case when the interface in the lee side of the plate reaches the lower tip. The transcritical regime is characterized by a local drop of the interface to that height.

For the supercritical regime the post-breaking evolution does not alter its lower

[7]An impulsive start is used for the simulations in figures 6.21, 6.22 and 6.23, for a better description of the initial evolution see appendix C

[8]The computations were carried out using a zero viscosity.

Fn limit. It is interesting to note that a single Level set function has been able to model correctly the drop of the water level to the lower tip of the plate. As described in section 3.3, when the interface approaches the lower tip the contour levels circle the plate and create a smooth transition of the density at the critical point of the lower tip.

It may be that the gulfs will wash us down;
It may be we shall touch the Happy Isles,
and see the great Achilles, whom we knew.
Ulysses, Alfred Tennyson

Chapter 7

Inclined plate

Even though it remains a very simply-defined problem, changing the plate geometry reveals some fundamental effects of the shape of the body on the flow developing around it. Studying the inclined plate highlights the influence of the front side of the body on the vorticity developing behind it and the effects of the shape of the body close to the free surface on the motion of interface. These aspects will be discussed in this chapter.

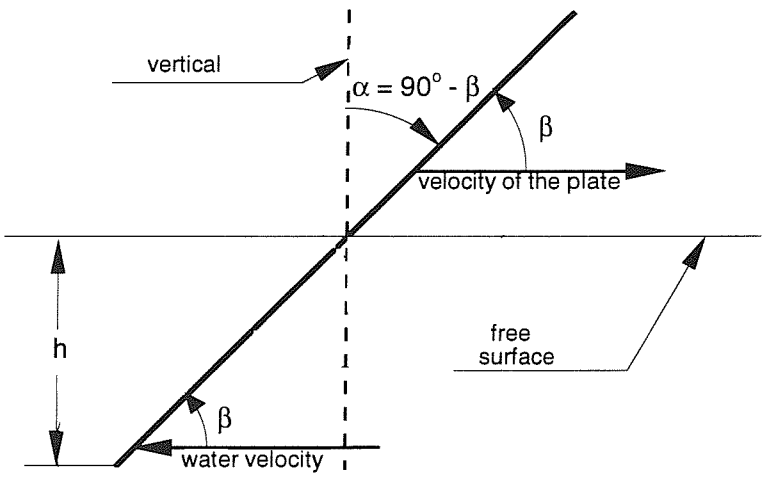

Figure 7.1: Definition of the variables and conventions used for the inclined plate.

Here, the angle β between the velocity of the plate and the plate itself (or equivalently in the frame of reference of the body, between the velocity of the

incoming liquid and the plate) is defined positive as in figure 7.1. The complementary angle α is also positive in this case.

In this chapter, the flow features in the case of a plate with an inclination of $\alpha = \pm 45^o$ are investigated. The initial submergence is h=0.1m. The geometry and the kinetic parameters used here result in the following values of the non-dimensional numbers: Froude number $Fn = 0.46$, Reynolds number $Re = 4 \cdot 10^4$ and Weber number $We = 279$ (see chapter 6 for the definition of these non-dimensional numbers).

In figure 7.2 the displacement x_p, the velocity u_p and the acceleration a_p of the inclined plate are plotted versus time.

plate motion	time interval	u_{max}	extreme acceleration
towards the right	[0.0s,0.76s]	0.45m/s	4.13m/s^2
towards the left	[0.76s,1.66s]	-0.5m/s	-10m/s^2

Table 7.1: Main characteristics of the plate motion.

Initially, the plate was driven for 30cm towards the right of the tank, then it stopped and the motion was reversed. The main features of the plate motion are described in table 7.1.

As for the vertical plate the two sets of data in figure 7.2 represent the experimental measurements (dots) and the numerical input (solid line). Also in this case, the main differences between the two sets are concentrated in the regions with high derivatives of the velocity, that is at the inversion of the motion and at the stopping point. The smoothed displacement, used as input to the numerical calculation, implies a similar filtering in the velocity of the water relative to that in the test. This has to be taken into account when comparing numerics and experiments.

The inversion of the motion represents a difficult process to reproduce numerically, but it was needed to ensure violent motion of the air-water interface. Alternatively the initial submergence could have been drastically reduced but this would have led to a greater dependence on the thickness of the plate and possibly on its oscillations.

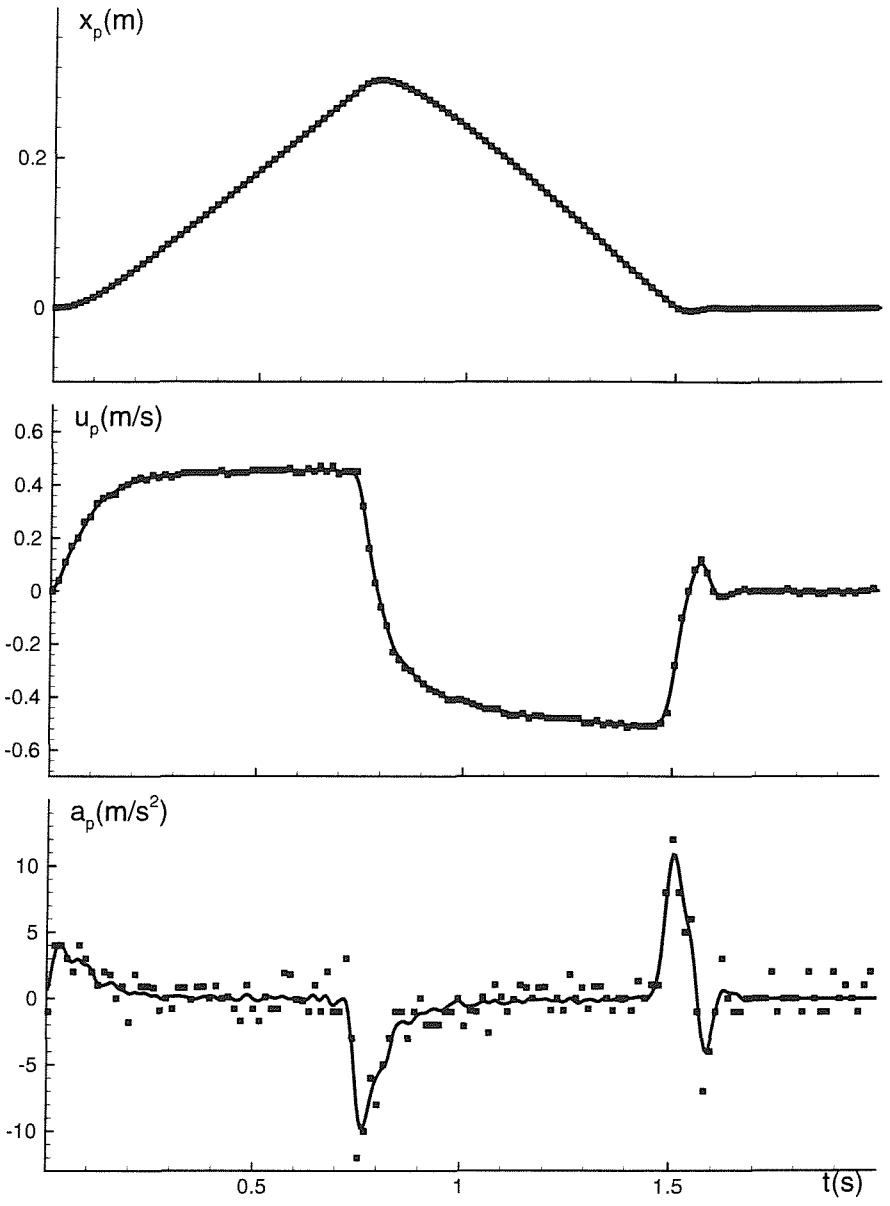

Figure 7.2: Time histories of the horizontal displacement x_p, velocity u_p and acceleration a_p of the plate with an inclination of $\pm 45^o$. The dots represent the experimental data, the solid lines represent the values used in the numerical calculation.

7.1 Evolution of the air-water interface

The velocity given to the plate causes the deformation of the free surface shown in figure 7.3. There, twelve different instants are shown with an interval of 0.128s between two successive pictures, with the first snapshot referring to time t=0.128s. The black and white background of each picture is the actual image captured by

the video camera, the black solid line on it is the numerical free surface, and the white solid line is the corresponding position of the plate in the calculations.

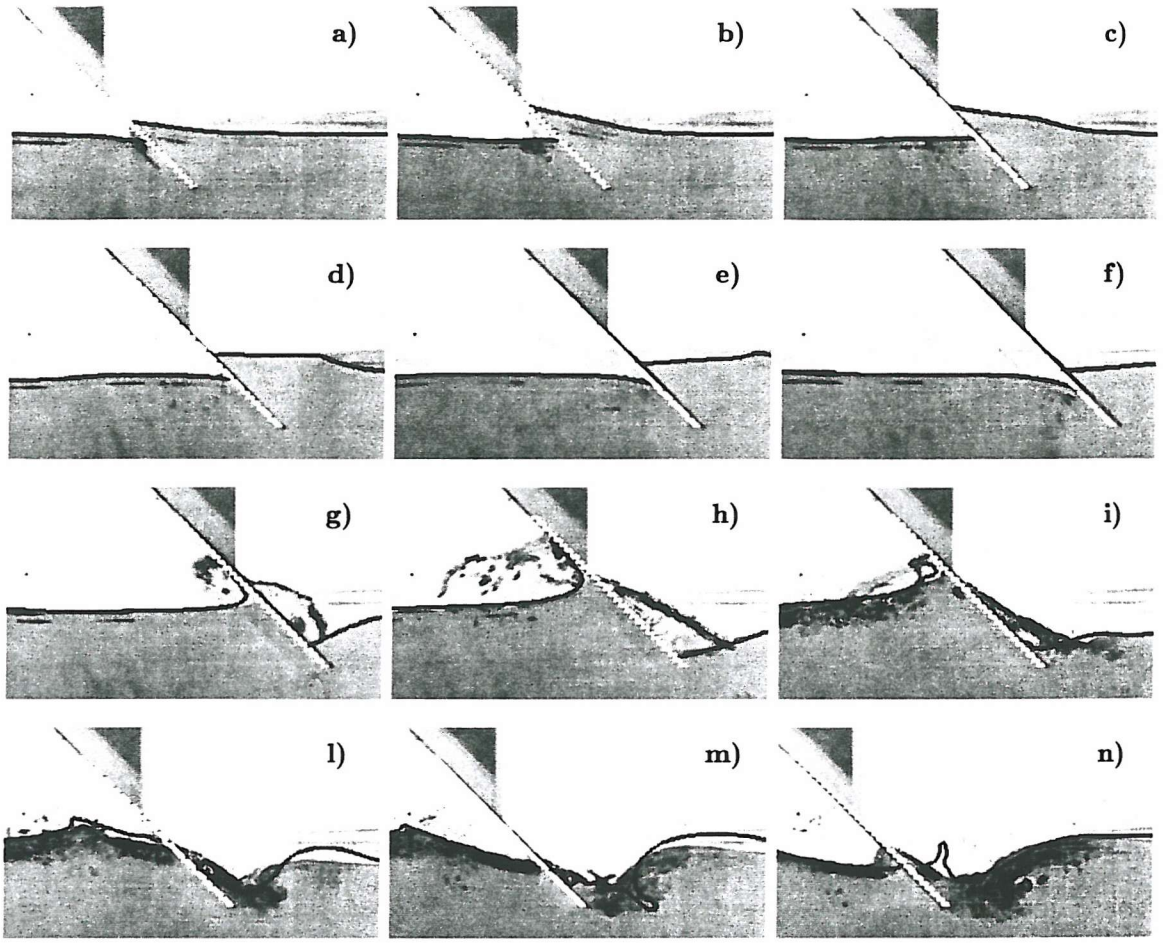

Figure 7.3: Inclined plate (45^o angle): comparison between numerical and experimental results, the black and white background is the experimental video-images, the solid black lines are the numerical free surface. (Times: a) t=.128s, b) t=0.256s, c) t=0.384s, d) t=0.512s, e) t=0.640s, f) t=0.768s, g) t=0.896s, h) t=1.024s, i) t=1.152s, l) t=1.280s, m) t=1.408s and n) t=1.536s. The plate starts to move from left to right and, at t=0.68s, it reverses its motion.)

The agreement between data from the two sources is generally good even though some differences appear after time t=1.152s.

The plate initially moves from left to right, causing an increase in the water level on the right side and a decrease on the left (see figures 7.3a–7.3e).

At time t=0.32s the water level reaches a value equal to 0.054m on the right hand side of the plate. This represents the maximum water height reached on that

side. In fact, soon after t=0.32s a first wave detaches on the right side and travels away from the body with a phase velocity of about 0.9m/s.

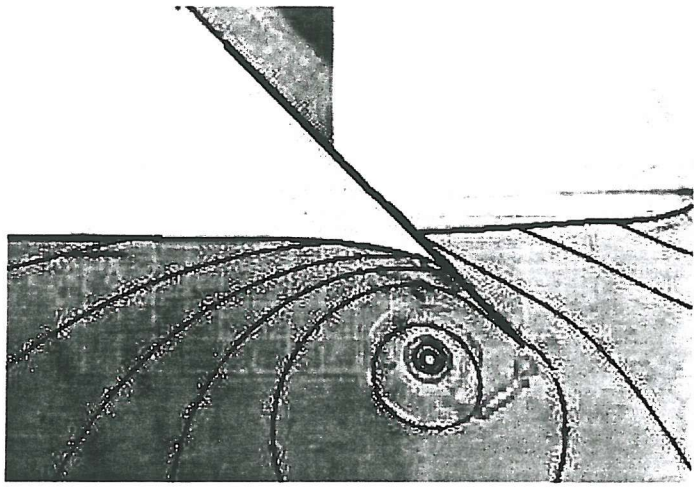

Figure 7.4: Inclined plate (45^o angle): vorticity and free surface (coloured lines) are superimposed on the experimental pictures (black and white background) at t=0.768s. The vorticity at the lower tip of the plate (contour lines) induces downward velocity at the contact point between the interface and the left side of the plate. The velocity field is highlighted through the streamlines.

At the same time, on the left side, the motion of the plate causes a decrease in the water level (see figures 7.3a-7.3e), which is further influenced by the concentration of vorticity at the lower tip coupled with the dynamics of the free surface. Figure 7.4 shows the position of the tip vortex relative to the plate and to the free surface at t=0.768s. It influences directly the deformation of the air-water interface and causes its rounding and draw down along the plate (see figures 7.3e and 7.3f).

It is not possible to follow the decrease of the water level further on, because between t=0.7s and t=0.8s the plate reverses. In figure 7.5, the history of the water induced load normal to the plate is plotted versus time, calculated as the integral of the pressure difference between the right and the left of the plate. This is the force tending to deform the plate itself. Around t=0.76s, corresponding to the maximum deceleration, the load acting on the plate has a sudden change which is likely to cause some bending. In fact, in figures 7.3-f and g, apart from a slight displacement of the plate due to the smoothing of the numerical x_p, the experimental plate does show a different angle of inclination with respect to the numerical non-deformable one, probably for this reason.

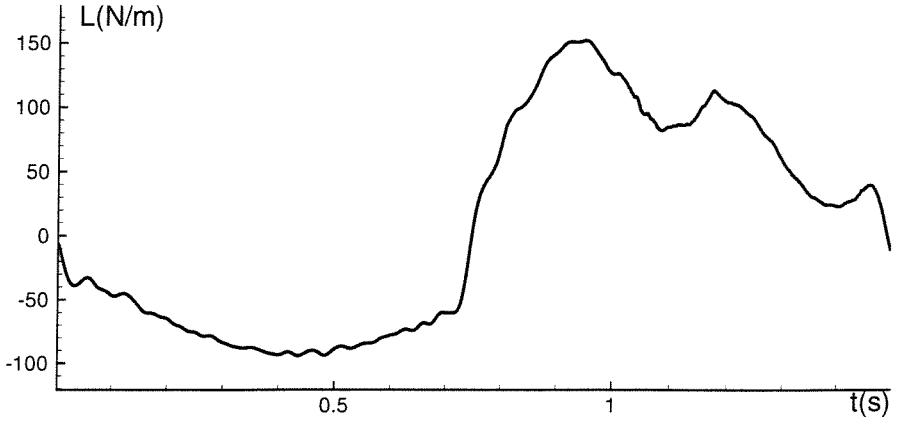

Figure 7.5: Time history of the integral of the pressure difference between the right and the left sides of the plate. The Load (L) is positive if it is represented by a vector pointing upwards and rightwards.

After the plate has reversed its motion, the free surface rises on the left side and decreases on the right (see figure 7.3-g,-h and i). The jet flowing upward now is thinner and reaches higher than the one created before on the right side, and the free surface on the right falls much more quickly than before on the left. This is due to the inclination of the plate relative to the direction of motion. Figure 7.6 shows the position of the stagnation points at the start up of two plates tilted at $\alpha = +45^o$ and -45^o respectively on the left and on the right. The -45° case shows a stagnation point on the left that is higher than the one on the right. Because of this the water level will drop more in the $+45^o$ case (left). The intensity of the downward flow motion is directly connected with the vertical position of the stagnation point along the plate. The lower the position is, the higher the surface moves. After the reverse the relative inclination of the plate α is equal to $+45^o$. The water level on the left reaches a maximum height of 0.14m and on the right side the free surface almost touches the lower tip of the plate.

During this phase, a counter-clockwise vortex is released on the right of the plate. It is closer to the surface than in the case of a vertical plate. So the interaction between the vortex sheet and the free surface is stronger and resembles that expected in the trans-critical regime (Tsai & Yue, 1993), even though the Froude number would be sub-critical for a vertical plate. In particular, the deformation of the free surface is so highly affected by the vorticity that a merging of the bumps created over the two vortical areas is observed, figures 7.3-m and n.

As the vorticity interacts with the free surface, differences appear between the

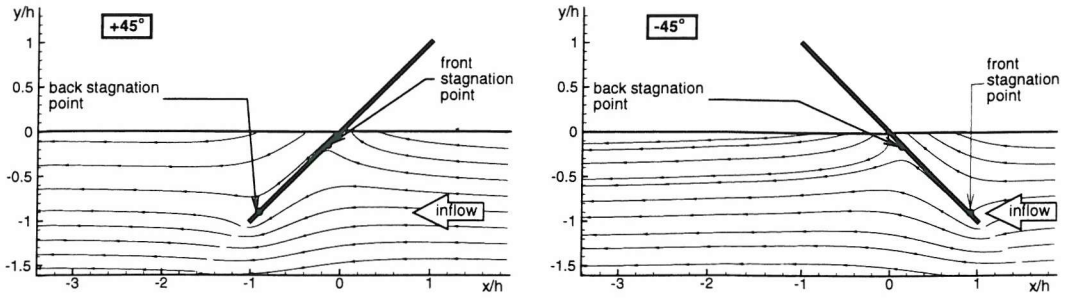

Figure 7.6: Position of the stagnation points for tilted plates (+45^o on the right and -45^o on the left). The flow field is characterized by the inflow condition on the left.

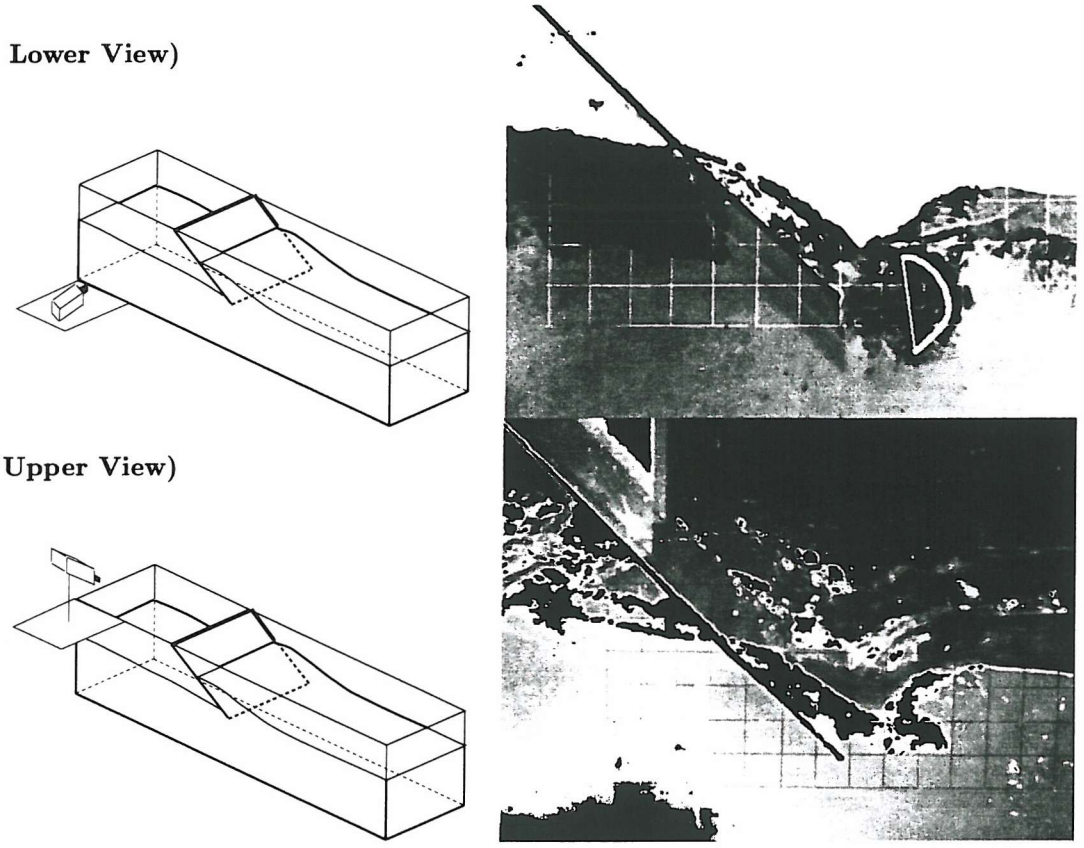

Figure 7.7: Three-dimensional effects in the experimental water flume at t=1.28s. The upper and lower side views show a curved vortex tube (top-right plot) and of a non uniform deformation of the free surface perpendicular to the plane of motion (bottom-right plot). In the middle section a higher bump displaced rightwards is observed, with respect to the sides.

numerical and experimental data. They are due to three-dimensional effects developing in the flume (see chapter 5). In the case of the tilted plate it was not possible to seal the sides of the plate against the vertical glass walls. As a result,

water flowed through the side gaps, generating a non-uniform out-of-plane vorticity.

This problem resembles the release of vorticity for a finite wing (Batchelor 1967). In this case the gap between the plate and walls of the flume could enforce something similar to the release of a horse-shoe vortex along the plate sides. So the vorticity released along the plate would have a maximum in the centre of the flume and would go to smaller values towards the side walls. Reduced vorticity at the side could imply a smaller interaction with the free surface, smaller bumps and a lower velocity of the vortex sheet. The last two aspects could be detected in figure 7.7, even though the three dimensional figures are not easily readable. There, the experimental images of the water flume are shown looking up and down at the side of the tank, at the time t=1.28s. The axis of the vortex is not rectilinear, but more curved towards the right in the centre plane, confirming a stronger vorticity in the central region. The free surface is more deformed in this section due to the larger intensity of the vorticity with respect to the other sections. Obviously the three-dimensional effects downgrade any quantitative comparisons, but qualitatively the numerical and experimental results have the same behaviour.

On the left of the flume, three-dimensional effects are limited. There, the thin upward jet moves forward and falls down onto the lower layer of water with almost no splash up. The presence of this jet is captured quite well by the numerical solution even though it develops when the numerical velocity of the plate is slightly different from the experimental one, and when the plate is slightly deformed. In the left plot of figure 7.8 the area of the jet is enlarged at t=1.152s. The main differences between experimental (black and white background) and numerical data (black solid line) are a thinner layer of water on the wall for the experiments and a shorter jet for the numerical solution. The difference in the length of the jet can be due to three-dimensional effects. A perspective view of the same situation shows a shorter protruding water area in the inner regions of the plate.

Both numerically and experimentally, the tip of the jet follows a parabolic trajectory shown in the right plot of figure 7.8 for the numerical solution.

While rising onto the plate, the water jet transformed all its vertical kinetic energy into potential energy. Just the horizontal component of the velocity is preserved, so the top of the jet is transformed in the free falling point of water described above. Subject to the gravity, the vertex of the jet follows a parabolic trajectory relative to a point with a horizontal velocity equal to the velocity of the

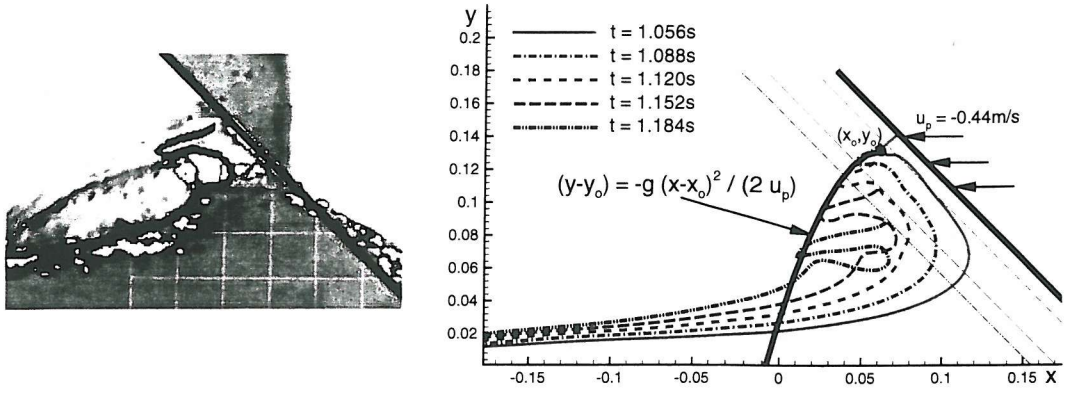

Figure 7.8: Left: enlarged view of the jet forming on the left of the plate at t=1.152s (see figure i-7.3). Right: numerical evolution of the jet. Its tip is in free fall and describes a parabolic trajectory.

plate.

7.2 The velocity field

LDA measurements of the velocity field have been carried out for the case described in the previous section. The velocities were measured at 36 fixed points placed on 6 rows (1 to 6) and 6 columns (A to F). The locations of these points relative to the initial position of the plate are plotted in figure 7.9. The points are spaced by 6cm in the x direction and by 2cm in the y direction; the coordinates of point A1 are (0.1094m,0.005m), where the plate intersects the free surface in the point (0.0m,0.0m). To simplify the reading of the next plots, figure 7.10 shows the relative position of the points of measurement with respect to the moving plate.

The analysis of the results starts here from the column F, the furthest from the plate. Comparisons between related numerical and experimental velocity histories are shown in figure 7.11. In this figure the green and purple symbols stand respectively for the measured horizontal and vertical components of the velocity, and the black solid and blue dashed lines are the numerical equivalents.

Initially the velocity in the column F varies very slowly because all its points are characterized by a distance from the plate larger than 0.30m, while variations in the velocities are appreciable only when the distance from the plate is lower than about 0.20m. Because the distance increases from F6 to F1, the points in the lower rows show a growth of the two velocity components.

When the plate starts to move from left to right, the time derivatives of v are

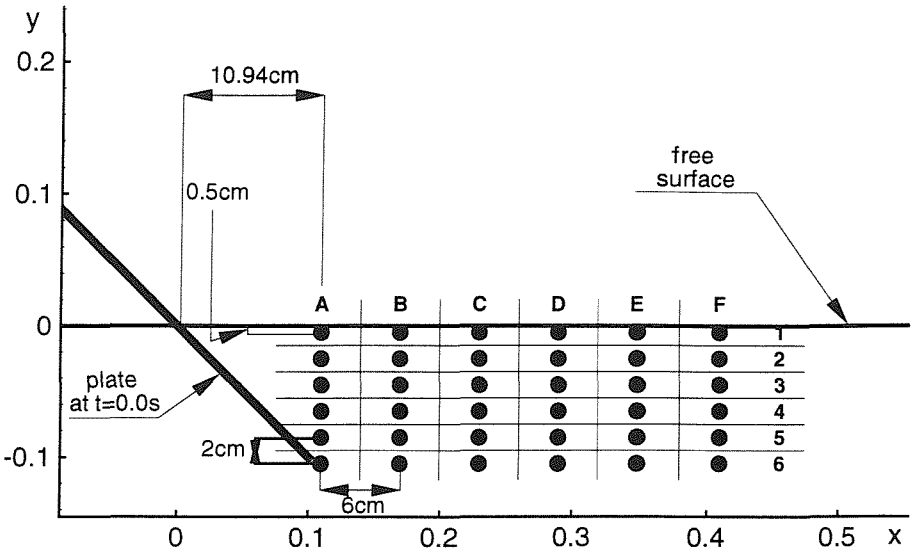

Figure 7.9: Location of the points of where LDA measurements were performed relative to the initial position of the plate. The points are labelled with a letter from A to F to indicate the column and a number from 1 to 6 to indicate the row.

positive for the points F1-F3 and negative for F4-F6. That is, the latter present a decreasing vertical component, the former a positive increasing value of v up to a point of local maximum before the reverse in the motion. This maximum appears very close to the instant when the first wave that leaves the plate reaches column F. In figure 7.12 vertical velocity contours are plotted over the passage of this wave. The front of the wave is characterized by high vertical velocities, which reach a maximum at the point of inflexion on the front face of the wave. Around this point the velocity contours are slightly elongated on the right. This implies that on any vertical line the maximum is reached earlier at lower points. In fact, point F3 has a velocity maximum at $t\simeq 0.45$s, F2 at $t\simeq 0.49$s and F1 at $t\simeq 0.51$s (see figure 7.11). At F4, F5 and F6 the main influence on the vertical velocity is the flow passing around the lower tip of the plate. This hides the occurrence of the local maximum.

Before the reverse, all the points in column F show a positive horizontal velocity, with a monotonic increase at the lower points, F4-F6, and an initial increase followed by a plateau at the upper points, F1-F3. For example, F1 shows an almost constant value of u between t=0.6s and t=0.76s. Figure 7.13 shows the horizontal velocity field at time t=0.576s. While the plate moves towards column F, points F1-F3 cross regions where the variation of the velocity is very small. F4-F6 are closer to the region between the stagnation point and the lower tip, where the gradients of velocity are very high. At those points the velocity of the

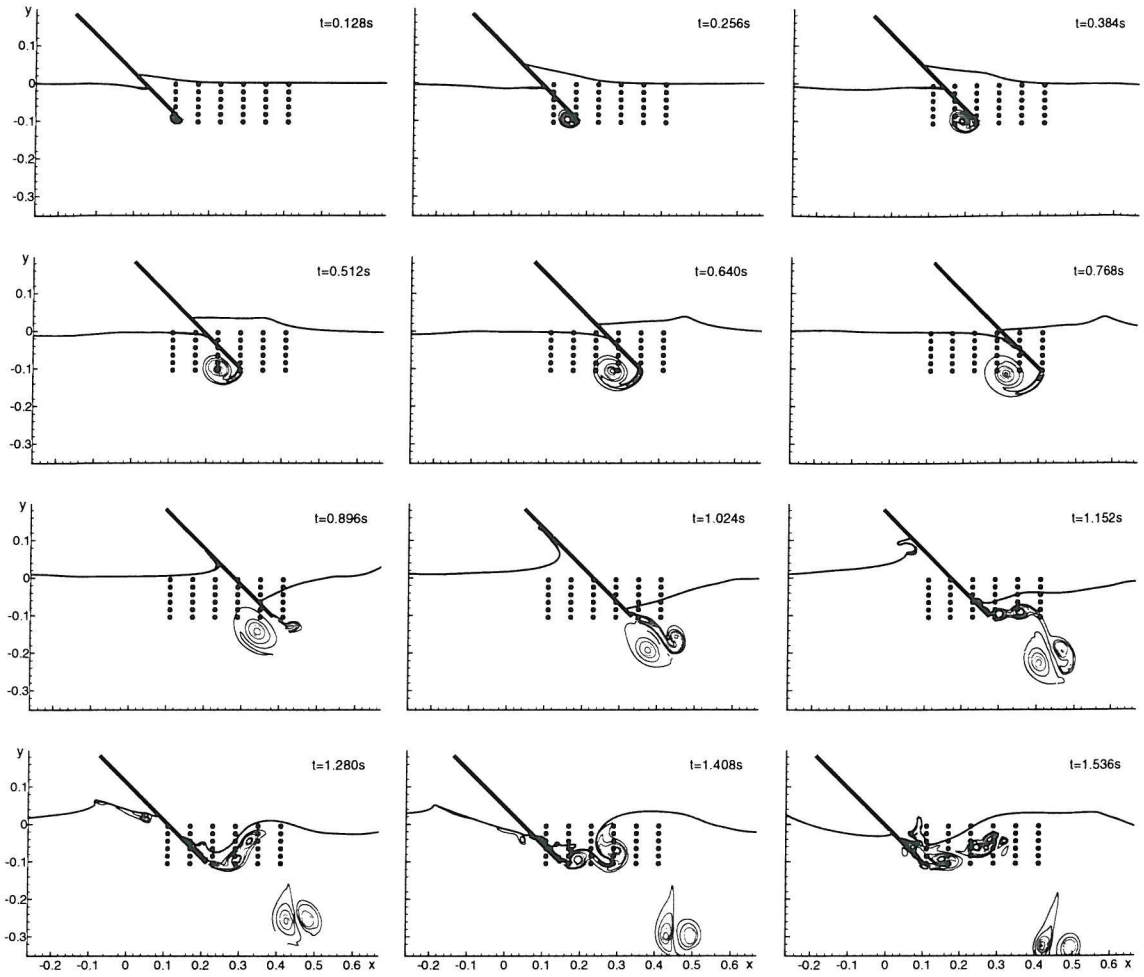

Figure 7.10: Deformation of the interface, evolution of the vorticity and points where the velocity is measured.

flow goes from a value close to that of the plate to zero.

When the plate reverses at t=0.68s it bends, causing spurious oscillations in the velocity measurements that are not present in the numerical results (see figures 7.11-F4, -F5, -F6). This effect is more evident in F5 where the horizontal component of the experimental velocity has a jump as the bent plate crosses into the space between the LDA horizontal beams. It would have been as far as 2cm from this point if the plate were stiff.

After the reverse of the motion, the free surface on the right of the plate falls leaving F1, F2 and F3 in air. The gap due to the presence of the air is well captured by the numerical solution. Differences between the experimental and numerical data appear after time t=1.1s when three-dimensional effects develop as explained in the previous section.

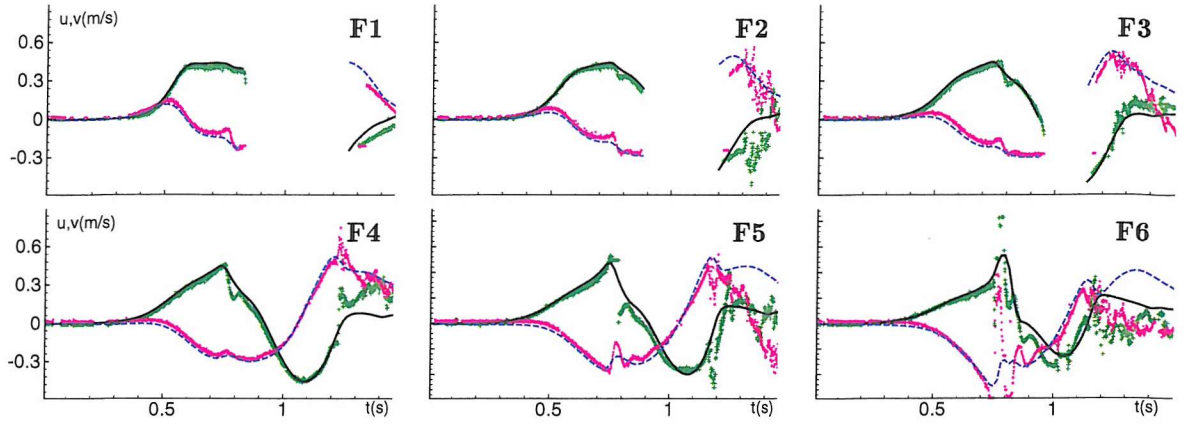

Figure 7.11: Velocity at points on column F of figure 7.9. The symbols represent the measurements. The solid lines represent the numerical u component of the velocity and the dashed lines the numerical v component.

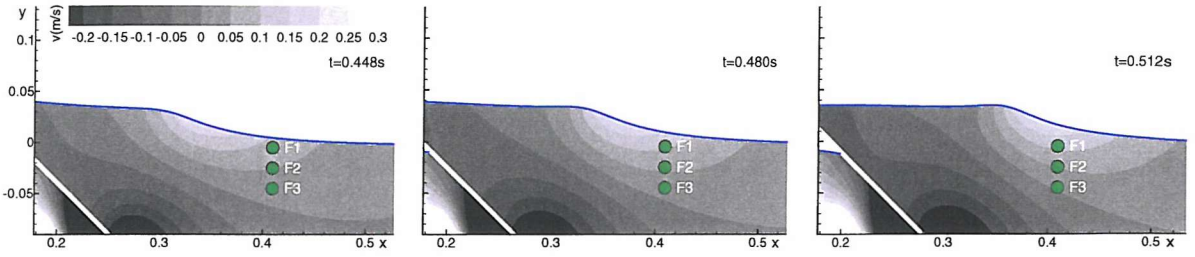

Figure 7.12: Contour levels of the vertical component of the velocity at three time steps. When the wave travelling from left to right arrives close to the column F, v presents a local maximum. The white stripe in the contours represents the position of the plate.

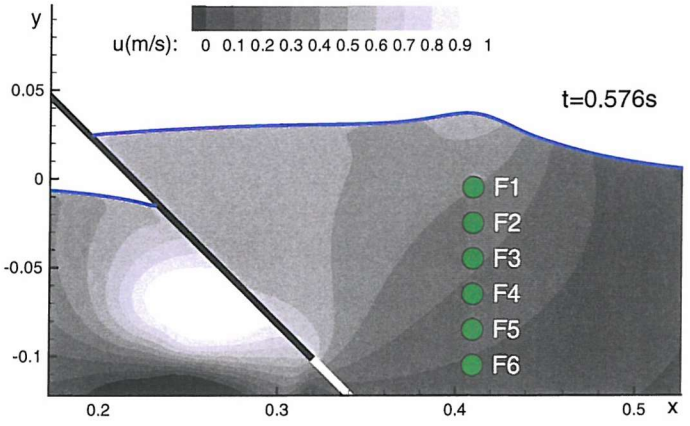

Figure 7.13: Horizontal velocity contours at time t=0.576s. The upper points F1-F3 are close to regions where the variation of the horizontal velocity is very small.

In figure 7.14, the velocity histories at points on column E are presented. The initial behaviour is very similar to that described for the points in column F, with

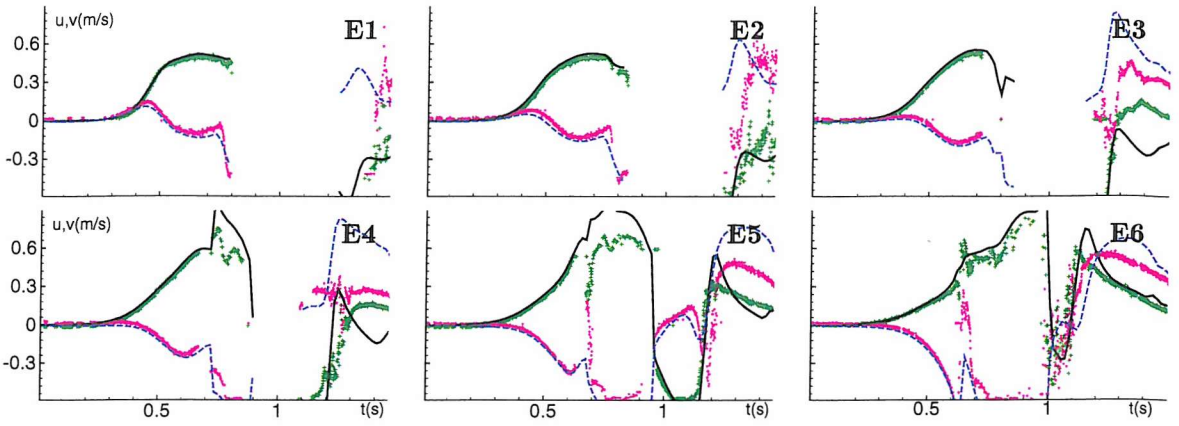

Figure 7.14: Velocity at points on column E of figure 7.9. The symbols represent the measurements. The solid lines represent the numerical u component of the velocity and the dashed lines the numerical v component.

the local maximum of v, the plateau of u, etc... However, column E shows a larger disagreement between numerical and experimental results in the time interval [0.7s,0.9s] at E4 and E5. These points are very close to the plate, so they are more affected by its bending (see section 5.2 for a rough quantification of this phenomenon).

At the time of the reverse of the motion (t=0.76s), there is a steep change in the vertical velocity component at E1 (see figure 7.14). At that time, this point is on the downstream side of the moving plate (see figure 7.10), where the water level drops very quickly. The numerical results reproduce a similar drop, though not as strong. Similar differences in the velocities at all upper points in this column are due to the numerical smoothing of the velocity at the inversion. Column E, like column F, shows a poorer agreement after time t=1.1s when the three-dimensional effect becomes dominant on the right side of the plate.

Figure 7.15 shows a comparison between numerical and experimental velocity components at points in column D. Apart for the phenomena described for column F, there is some disagreement between numerical and experimental results at D4 and D5 similar to those noted for E4 and E5. All these points are located in the region of high vorticity released at the lower tip of the plate. The differences between numerical and experimental results in this region underline the high sensitivity of the flow to the local velocity of the plate.

Another feature is evident in the results for column D; at D6 there is a longer scattering of the velocity components than at any other measurement point. Apart

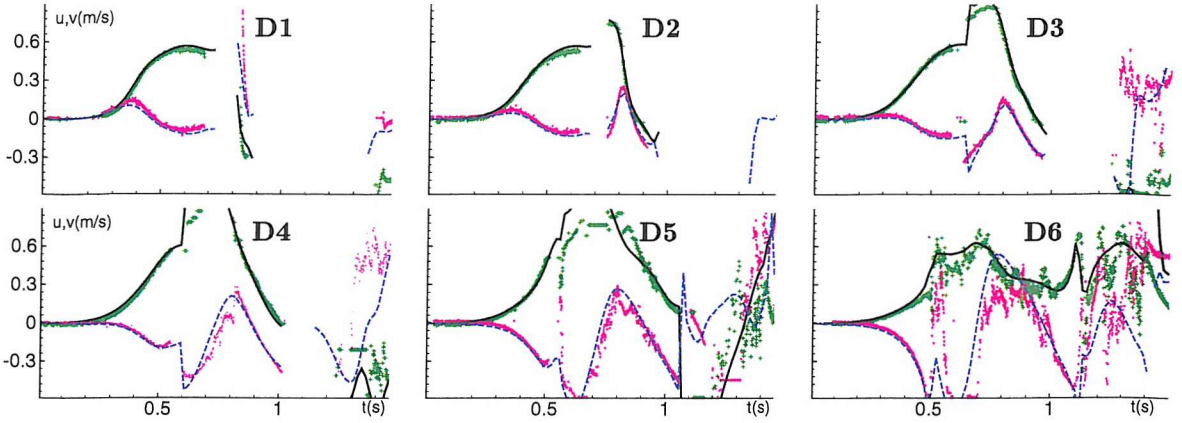

Figure 7.15: Velocity components at points on column D. The symbols represent the measurements. The solid lines represent the numerical u component of the velocity and the dashed lines the v component.

from a short interval [1.s,1.1s], from time t=0.5s to t=1.5s, D6 is always in a region of high vorticity where a large number of bubbles is concentrated. As shown in Mudde *et al.* (1998), the presence of bubbles and of their wake causes local jumps in the velocity measurements. As the bubbles are dispersed along the axis of the flume the scatter becomes even larger.

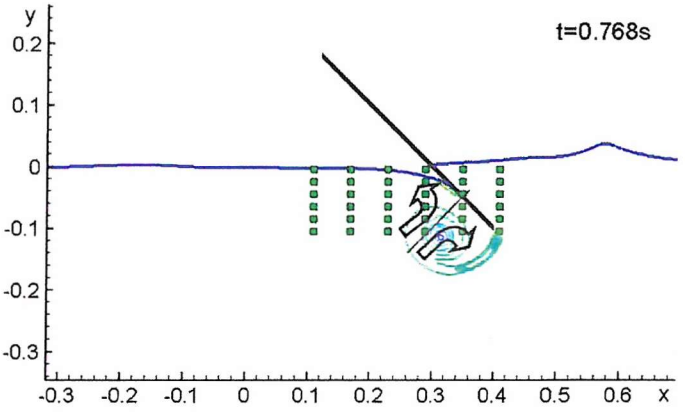

Figure 7.16: Flow directions induced by the inertia effects when the plate inverts its motion.

Just after the reverse of the motion, column D is on the left side of the plate. In the frame of reference of the plate, the stopping and the reverse of the motion are seen as an inflow condition. The water in upper left half of the plate is diverted upwards and the other downwards. This effect is summed to the local flow field (see figure 7.16). D2 and D3 are in the upper region at the time of

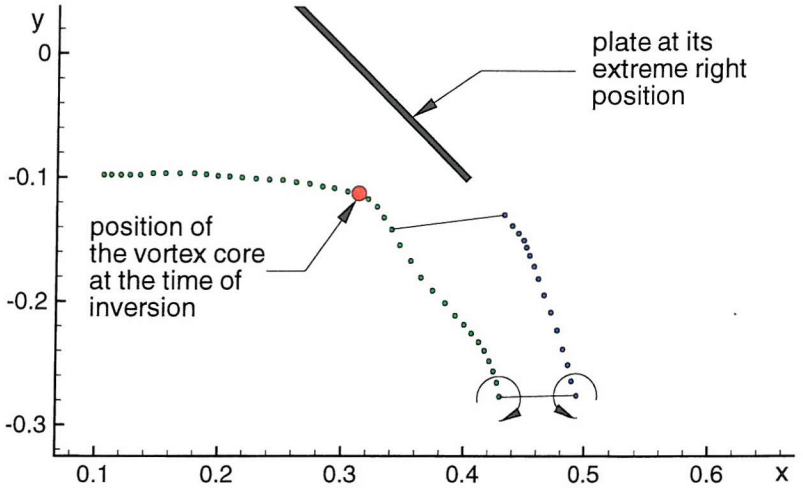

Figure 7.17: Trajectories of vortex cores released on the right and on the left of the plate.

reversing. While the plate moves further on, they come to the region affected by downward motion. The passage between these two regions results in a local maximum of the vertical component of the velocity.

Another effect of the deflection of the flow (see figure 7.16) is the displacement of the vorticity. The trajectory of the clockwise vorticity created initially on the left side of the plate is shown in figure 7.17. When the plate reverses, the trajectory changes direction and becomes aligned with the plate. As it leaves the plate its motion is affected by the presence of the anticlockwise vorticity created on the other side. It is not possible to describe the motion of these two vortices simply as a vortex pair because vorticity is continuously released at the lower tip of the plate, influencing the motion of the existing vortices. Similar behaviour is

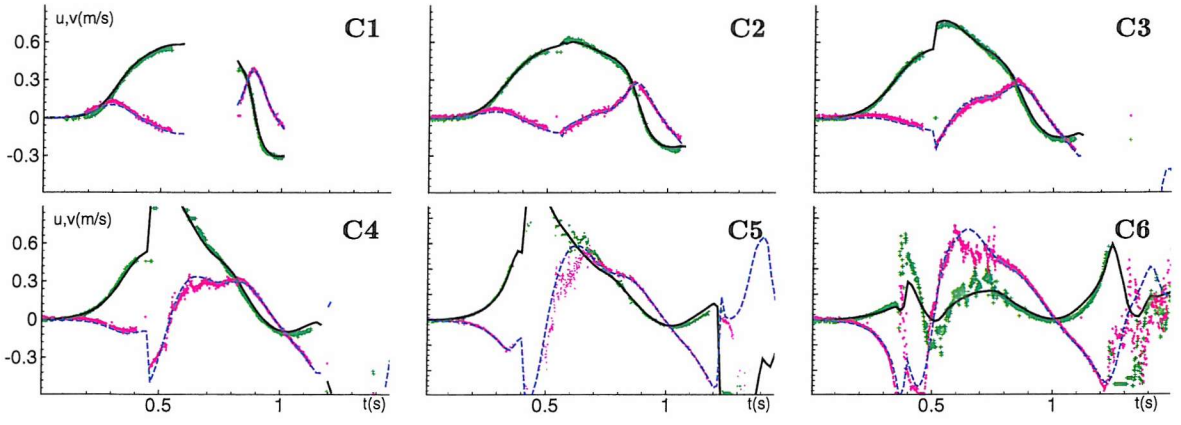

Figure 7.18: Velocity at points on column C of figure 7.9. The symbols represent the experimental measurements. The solid lines represent the numerical u component of the velocity and the dashed lines the numerical v component.

seen in column C. Figure 7.18 presents a comparison between numerical and

experimental results for this column. The vertical velocities at C1-C3 are characterized by local maxima at t=0.88s. It is interesting to note that even at this section, quite far from the plate at the moment of reverse, it is the vertical velocity that is the more sensitive to the motion of the plate. In fact, at C2 and C3 there is a change in dv/dt around the time of reverse. Comparisons between numerical and experimental results are quite satisfactory even at the lower points. The velocity at C6, just below the plate at times t=0.38s and t=1.2s, shows the passage of the vortex sheet soon after those times. The first jump in velocity is captured quite well in the prediction considering the sensitivity of that point to the local flow velocity, to the thickness of the plate and to the exact distance from it. After t=1.2s the point is on the right side of the plate, where three-dimensional effects prevent any further investigation.

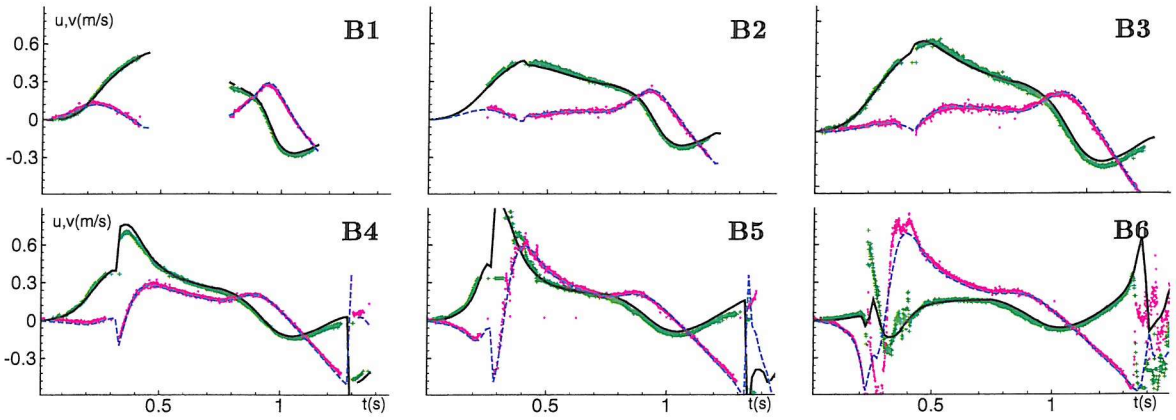

Figure 7.19: Velocity at points along column B of figure 7.9. The symbols represent the experimental measurements. The solid lines represent the numerical u component of the velocity and the dashed lines the numerical v component.

Figure 7.19 shows the comparison between the different data sets in column B. This column sums all the effects previously described: a) the initial local maximum of v at B1-B3 when the front of the first wave travels past, and correspondingly the decrease of the same component of the velocity at B4-B6, b) the drop in the water level at B1 when it passes the left side of the plate, c) the change in the slope of v at t=0.76s, d) the second local maximum of v at B1-B5 after the inversion of the motion, e) three-dimensional effects at B6 after t=1.3s.

A similar behaviour is shown in column A (see figure 7.20).

When the plate starts to move, the lower points in column A are the closest to plate. Their horizontal and vertical velocities are characterized by some

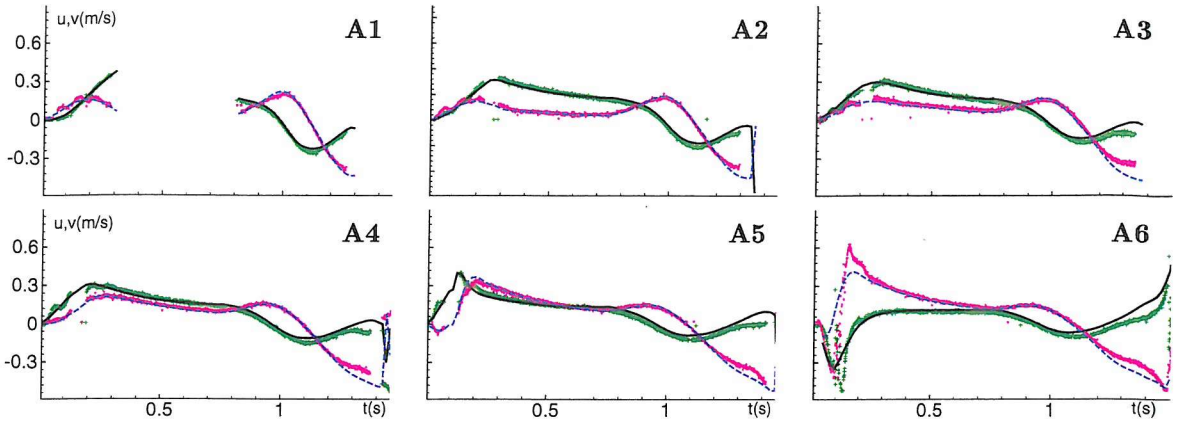

Figure 7.20: Velocity at points along column A of figure 7.9. The symbols represent the experimental measurements. The solid lines represent the numerical u component of the velocity and the dashed lines the numerical v component.

oscillations enlarged in figure 7.21 for point A4.

Those phenomena could be caused by either the oscillations of the carriage or the bending of the plate. From figure 7.21 it is evident that the frequency of the oscillation is about 14Hz. As shown in section 5.4 the first natural frequency of the plate is about 13Hz. Therefore the observed oscillations are probably due to the bending of the plate.

This could also cause instabilities in the vortex sheet. Although no clear proof can be extracted from the tests, such instabilities are suggested by the oscillations detected in the velocity measurements for rows 4,5 and 6.

Measurements from column A show a fairly good agreement between experimental and numerical results for the whole period. Some differences appear only after t=1.3s when the plate approaches the stopping point. The cause of these differences can be due to the bending of the plate and to the smoothing of the velocity in the numerical model.

7.3 Effects of the inclination of the plate

Comparison with experimental results has shown that the numerical method used here is reliable. So the code has been used to proceed with a further analysis of the effects of inclination of the plate at a higher Froude: $Fn = 0.8$. The incident flow is started impulsively and then maintains a constant velocity. This situation is in the transcritical regime for a vertical plate (Tsai & Yue, 1993), so the inclination

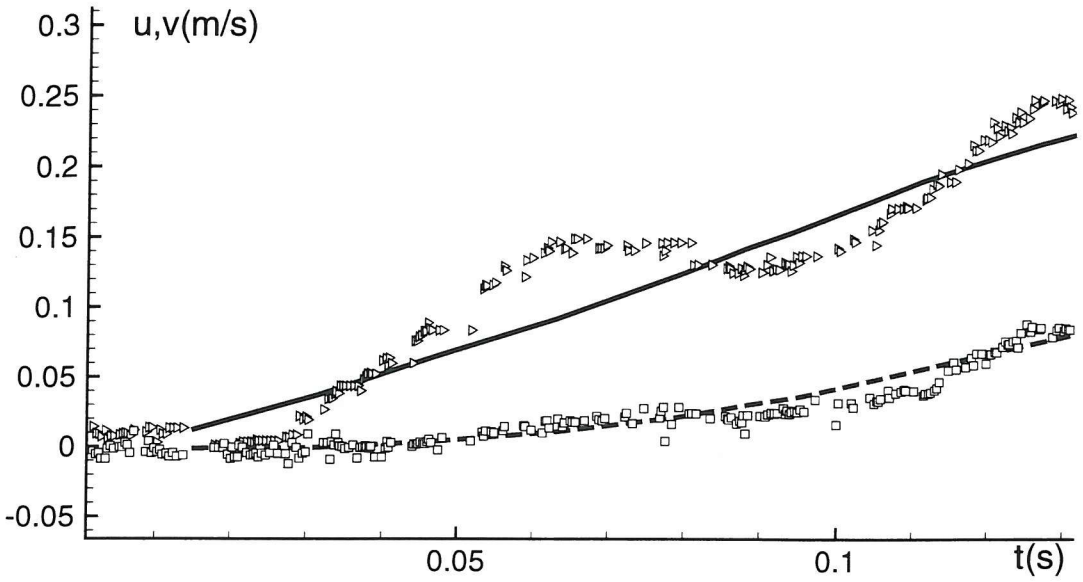

Figure 7.21: Enlarged view of the velocity at the start up at A4. Both the u and v components oscillate with a frequency of about 14Hz.

can be an important factor in changing regime. This numerical calculation was carried out with zero viscosity and no surface tension to avoid the effects they can have on the evolution of the flow.

The plate has been inclined by $\pm 15^o$, $\pm 30^o$ and $\pm 45^o$. Figure 7.22 shows the free surface and the vorticity contours at the time $t\sqrt{g/h} = 3.6s$ for these inclinations.

The vertical plate is has a plunging jet forming in front of it. On the downstream side the interface interacts with the vorticity stretching it, causing it to roll up.

The first effects of the inclination of the plate are related to the intensity and the velocity of the vorticity release at the lower edge. A positive inclination leads to a region of weaker vorticity travelling faster. This is because with a positive inclination there is a smaller change in direction of the flow at the tip and consequently less vorticity and higher velocity. Positively inclined plates preserve the features of the transcritical regime. The deformation of the interface causes the stretching of the vortex sheet and its successive rolling up, even though it is more intense than the vertical case.

On the other hand, the strong vorticity created at the back of the negatively inclined plates influences the free surface as soon as this is immediately above the vortex sheet. The vorticity creates large bumps on the interface and draws it

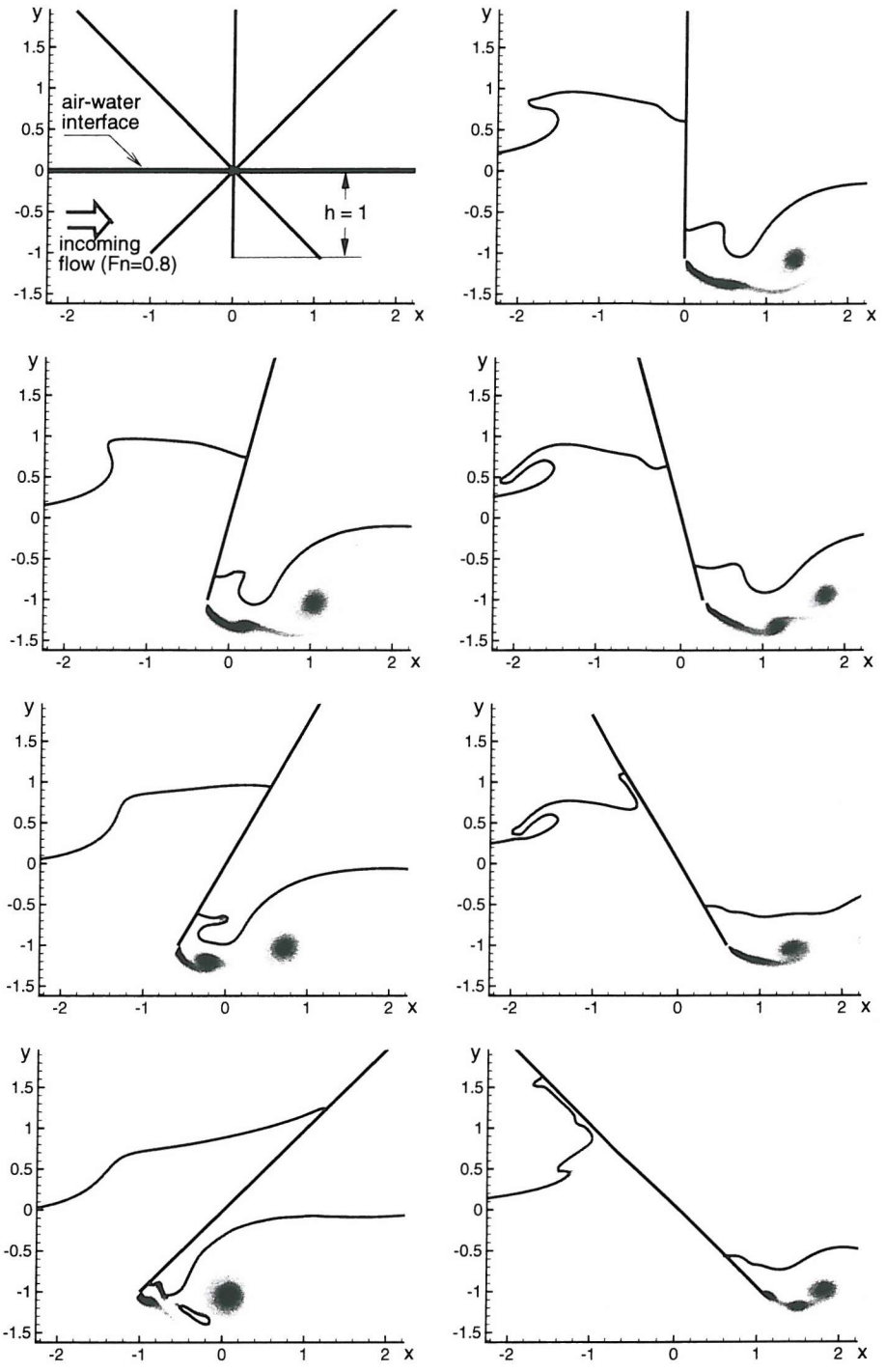

Figure 7.22: Deformation of the free surface and vorticity contours at the non dimensional time $t\sqrt{g/h}$=3.6. The first row shows a schematic representation of the problem and the solution for the vertical plate. The successive rows show the evolution of the flow field for the $\pm 15^o$, $\pm 30^o$ and the $\pm 45^o$ inclined cases (α is positive in the right plots and negative in the left ones).

down. As a result, a large displacement of the free surface is produced. The interface reaches the lower tip of the plate for the case $\alpha = -45^o$. The behaviour is practically supercritical, according to the definition by Tsai & Yue (1993).

On the left side of the plate the negative inclination implies reduced gravitational effects on the water rising along the side of the plate, so if any breaking develops it is delayed with respect to the vertical case. For the positively inclined plates, the jet becomes thinner as the inclination increases. So the breaking becomes less energetic until it almost disappears. Cases $\alpha = +30^o$ and $+45^o$ show the formation of a small jet developing at the top of the water rising along the plate that will fall down with a parabolic trajectory as described earlier.

For a more detailed picture of the flow field developing at the different inclinations, see appendix D.

Higher angles of inclination have not been analyzed here. When the angle increases, the effects of the boundary layer on the developing flow become more important. The analysis of these effects is more complicated and no comment can be inferred from the kind of study carried out here.

7.4 Conclusions

The problem of the inclined plate is more challenging than that with a vertical arrangement. From a numerical point of view the case with $\alpha = +45^o$ is the most difficult to reproduce, because of the presence of both breaking and vortex shedding.

The problem is made even more difficult in the experiments when the motion reverses. Nonetheless the numerical and experimental comparisons are satisfactory.

Besides the interaction between the interface and vorticity, the experiments and the numerical results highlighted the characteristics of the interaction between the flow fields developing on the two sides of the plate. The analysis has revealed the sensitivity of the vorticity to the local velocity of the plate and has shown that the major effects of the reverse of the motion are on the vertical rather than the horizontal component of the velocity.

Encouraged by these results, a parametric analysis has been carried out in terms of the plate inclination. The findings of this analysis show the transition to the supercritical regime for the negatively inclined plate and the disappearance of the front plunging jet for sufficiently large inclinations of either sign.

To strive, to seek, to find, and not to yield.
Ulysses, Alfred Tennyson

Chapter 8

Conclusions

In this thesis a multiphase method has been developed for the study of violent free surface motions. The general application makes use of developments in CFD methods for single fluids and models the two phases as a fluid with varying physical properties. This approach is formally elegant but implies problems in the numerical treatment of the interface. Here particular attention has been paid to overcome these problems. The detection and correction of numerical error sources have been achieved by analyzing in detail canonical problems which involve phenomena relevant for naval architecture, and coastal and offshore engineering research fields.

The improved numerical scheme has also been used to study more realistic problems involving interactions among different physical phenomena. Dedicated experiments were performed for the same test case both to validate the method and to capture the physical features that are beyond the reach of the numerical solution.

8.1 Numerical method

The numerical method applied here can be briefly described as:

- a Finite Difference Eulerian solver for the laminar Navier-Stokes equations
- with an approximate projection method for the pressure problem in incompressible fluids
- and an improved Level-Set model to capture the interface.

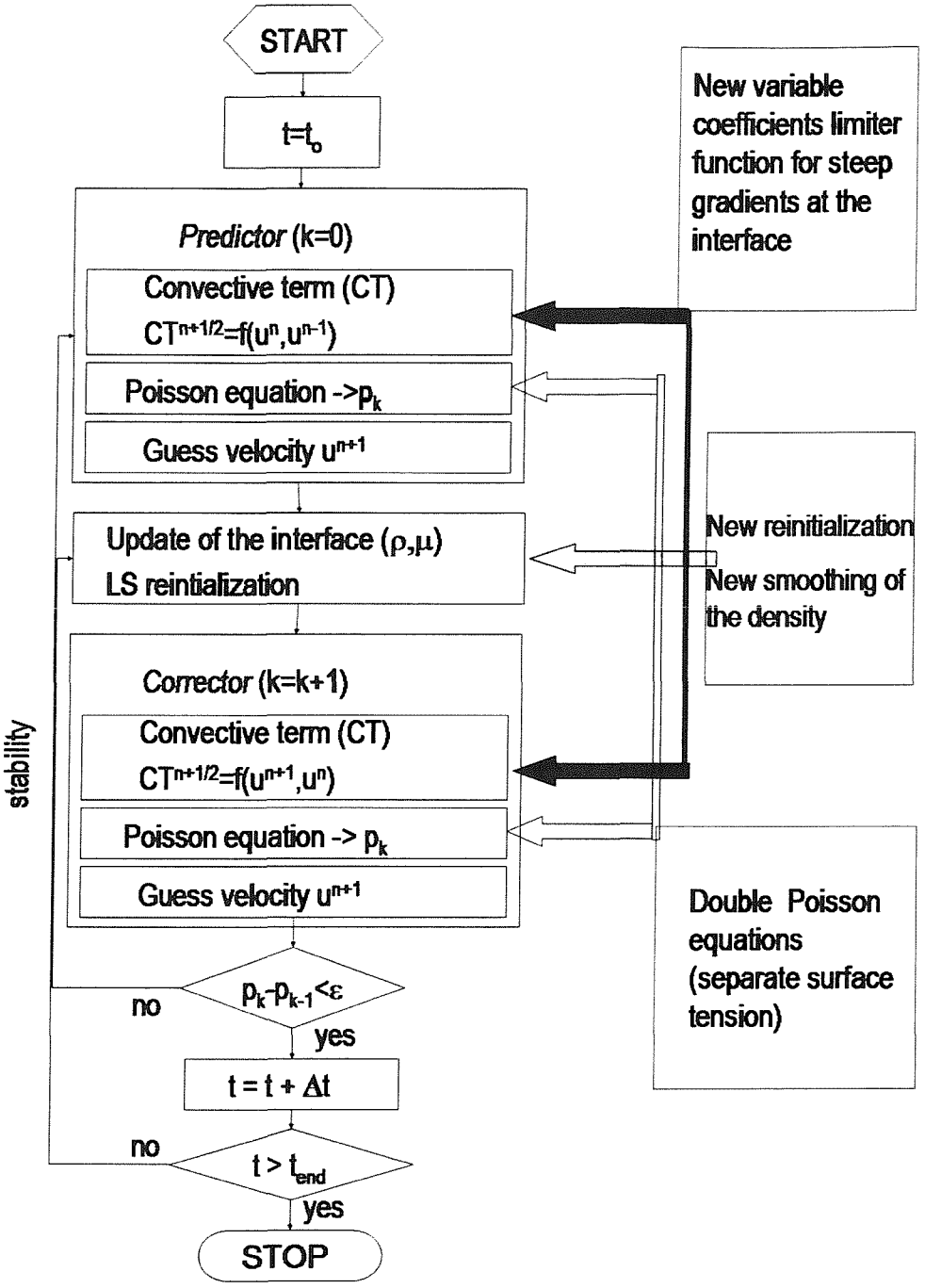

Figure 8.1: Flow diagram of the present numerical scheme and related novel features.

The corresponding flow diagram is shown in figure 8.1. A second order accuracy in time is obtained through a predictor-corrector scheme, stabilized through iterative corrector steps. The same accuracy is used for the spatial discretization inside each fluid but larger errors can be introduced at the interface. The high gradients of the fluid variables at the interface cause large second order derivatives of the quantities

of interest and consequently a drop in the order of approximation. The smoothing of the fluid properties on a finite distance partially reduces the errors. Further corrections have been introduced:

- **A variable coefficient limiter** for the discretization of the convective terms. The resulting ENO scheme is characterized by a minmod limiter inside each fluid, by a superbee scheme at the interface and by a limiter varying from one to the other in the transition region. This type of limiter reduces the diffusion of vorticity from the interface to the two fluid subdomains.

- **Two different Poisson equations** are solved for the projection of the velocity field on a divergent free space. The first one neglects the effects of surface tension, the second one uses a Brackbill *et al.* (1992) approximation for the surface tension and projects the solution on a field independent of the density. This reduces the numerical errors associated with the solution of the system with largely varying coefficients.

- **A specialized numerical discretization of the distance function gradients** has been adopted very close to the interface. This reduces the smoothing errors usually associated with the Level-Set technique.

- **An exponential function smoothes the density** across the interface. This limits the gradients in the solution of the Poisson equation, preserving the mass in a satisfactory way.

8.2 Applications

The developed method has been applied for the solution of different problems, culminating in a detailed numerical analysis of the flow field around a surface piercing plate. This problem is characterized by a simple geometry but captures the major features connected with moving surface piercing bodies. The features of the flow pattern around the plate can be schematically summarized as (see fig.8.2): 1) high deformations of the interface occurs on both sides with eventual breaking and air entrainment, 2) large vorticity is generated at the lower tip of the plate and 3) the vorticity interacts with the interface.

In a preliminary phase, the different phenomena involved have been analyzed individually by means of problems *ad hoc*. The rising of a gas bubble in water has

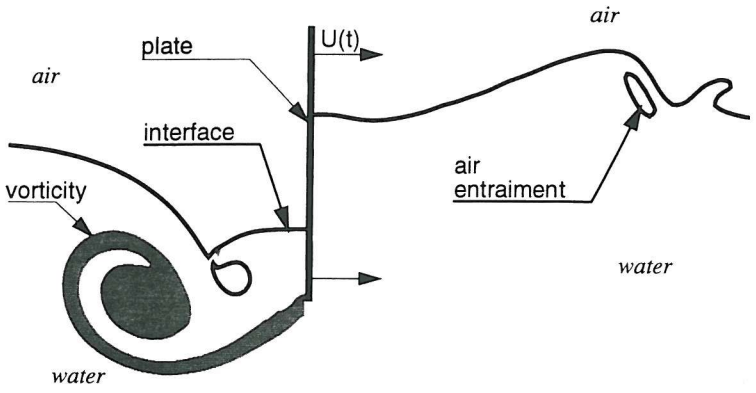

Figure 8.2: Sketch of the flow field features developing around a surface piercing plate.

been used to test the modelling of surface tension, the dam-break *plus* impact problem to study large deformations of interface with air entrainment, the vortex pair rising towards the air-water interface to quantify the interaction between the interface and the vorticity.

The different elements were subsequently studied as simultaneous phenomena mutually influencing each other in the case of the moving surface piercing plate. This problem has been investigated both from a numerical and an experimental point of view. This gives an intrinsic value to the experimental data in the process of validation of numerical codes.

The case analyzed, despite its simplicity, represents a useful benchmark and is strictly linked to many other practical applications such those shown in figure 8.3. It showed that the numerical model produced high quality date in those very challenging circumstances.

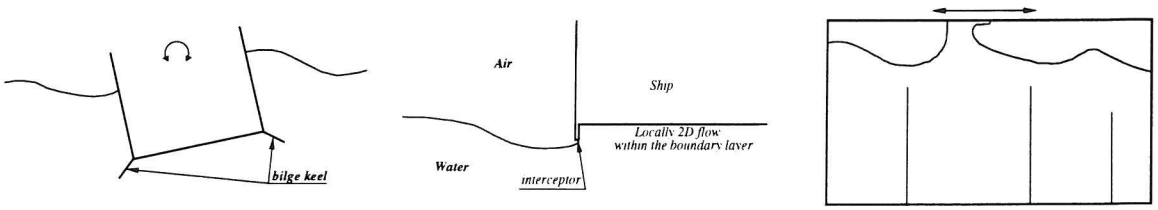

Figure 8.3: Perspectives. Applications to different practical problems: roll of a ship section with bilge keels for the damping; flow after the interceptor; sloshing flow in a tank with buffles.

In the case of the vertical plate, the classification of three different regimes of interaction between free surface and vorticity (Tsai & Yue, 1993) has been recovered. Moreover the cases analyzed here numerically and experimentally have highlighted:

- the effects of the stopping phase of the plate on the deformation of the free surface and on the evolution of the vorticity. New vorticity is created on the back of the plate and it interacts with that created during the forward motion;
- a different limit of transition from the transcritical to the supercritical regime with respect to the analysis of Tsai & Yue (1993);
- some breaking features. The wave breaking events are more affected by high accelerations than by high speeds of the plate;
- the effects of different inclinations of the plate on the deformation of the free surface and on the vorticity. Large inclinations, independently of the sign, reduce the intensity of the breaking. Large positive inclinations decrease the limit of transition to the supercritical regime.
- the occurrence of oscillations of the velocity have been noted in the vortical region of the flow field. The causes of these instabilities are probably associated with the bending of the plate. This implies that a structural analysis is sometimes necessary to characterize correctly the vortical flow field around the bodies.
- three-dimensional effects connected with the test set up. These develop after the breaking phenomena and affect the region close to the air-water interface, in particular the recirculation region around the entrapped air. Larger effects on the flow field are due the three-dimensional effects generated by small gaps in the body. The vorticity release by the body reduces in the region of small gaps deforming the vortical tube downstream the body.

8.3 Recommendations for future work

In this thesis the attention has been focused on the development of a numerical solver effective for the analysis of violent free surface flows. For the problem of the

plate, the phenomena occurring at the interface are largely influenced by the shape of the partially immersed body. So the natural development of this work is a more suitable and efficient modelling of the geometry of the body, in a general way. The preliminary step towards such investigation has already started. Making use of the Level-Set tools the body geometry can be modelled as a zero level of a distance function from the body boundary. A smooth transition from the Navier-Stokes equations to the equations of the solid body is driven by the same function. This method does not need any adjustment of the grid that can be kept Cartesian. More details about the formulation can be found in appendix E, where preliminary results are shown. Figure 8.4 presents the evolution of the wake length downstream of a circular cylinder moving in a single fluid at different Reynolds numbers. The numerical results (solid line) are compared to the experimental data by Honji & Taneda, 1972 (symbol). The regime of laminar flow is well captured by this method. In figure 8.5 the same method is applied to a case closer to the one studied in the thesis. A circular cylinder moves with a constant velocity towards the air-water interface. While the cylinder proceeds in its water-exit phase, the

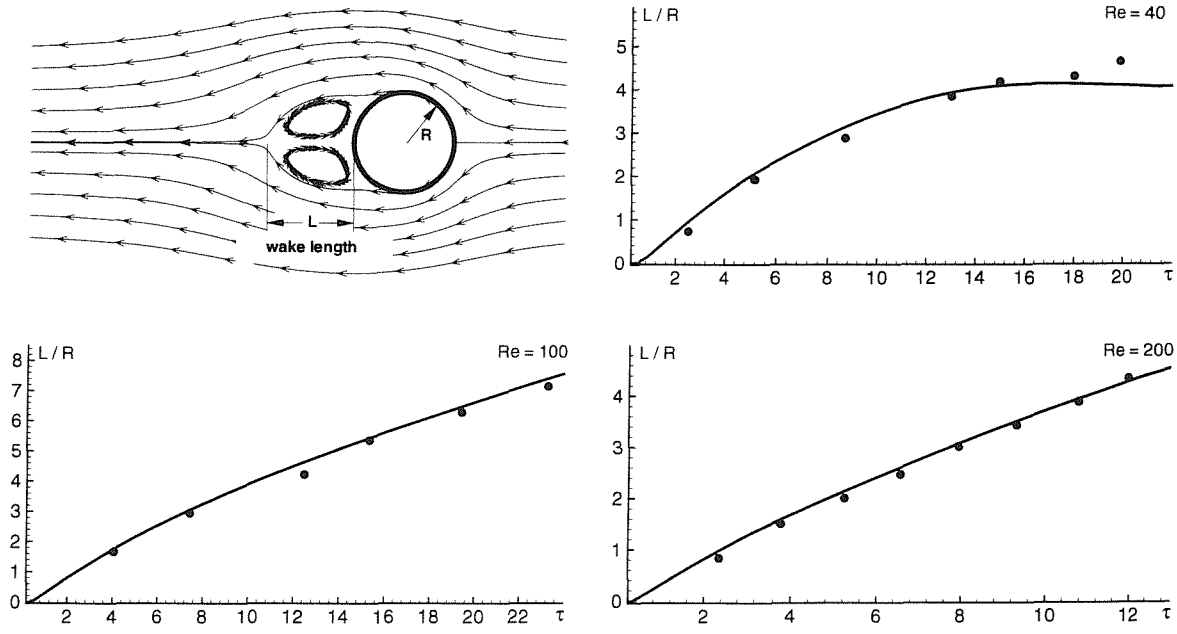

Figure 8.4: Length of the wake downstream a circular cylinder in the horizontal plane. The numerical results (solid line) are compared with the experiments by Honji & Taneda, (1972) (dots).

latter deforms adjusting its shape to the cylinder so that a layer of water is

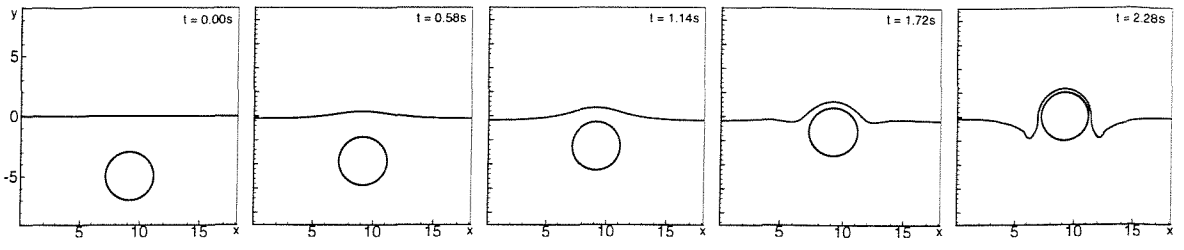

Figure 8.5: General modelling of the body geometry. Application to the flow around a body interacting with the free surface: water exit of a circular cylinder.

captures between the body and the water above.

This first attempt shows the potential of the suggested approach. Further studies are proposed. They should be dedicated to the analysis of the flow field features around the body. Following the philosophy of this thesis, simple prototype problems are recommended. Around simplified geometries, pressure fields and boundary layer features could be the variables to compare quantitatively to other solvers and to experimental data.

Appendix A

Convergence study

The study of the convergence is here discussed in two separate parts. The first concerns the Navier-Stokes solver itself and the second the level-set algorithm adopted for the free surface.

A.1 Navier-Stokes solver

In this thesis the Navier-Stokes equations have been solved to study flows with an interface between air and water. Different methods used to model the transition from one phase to the other can produce different evolutions of the interface. Here the properties of accuracy and convergence of the method used have been analyzed in the case of the dam-break problem described in chapter 4[1]. The analysis has been carried out both for local and global quantities. Given $q(t, \Delta x)$, the parameter analyzed, its integral $Iq(\Delta x)$ in an interval of time $[t_0, t_f]$ is calculated varying the discretization parameter Δx. Three different meshes are considered: $N \times N$, $1.5N \times 1.5N$ and $2N \times 2N$, where $N = H/\Delta x = 50$. The order of accuracy is calculated with the following procedures: (1) if the exact solution $Iq(\Delta x = 0)$ is known, the order of convergence is equal to

$$-\frac{\log \dfrac{Iq(\Delta x_2) - Iq(\Delta x = 0)}{Iq(\Delta x_1) - Iq(\Delta x = 0)}}{\log \dfrac{\Delta x_2}{\Delta x_1}}; \tag{A.1}$$

(2) if the exact solution is not available, the exact solution is calculated from the integrals on three different meshes ($Iq(\Delta x_1)$, $Iq(\Delta x_2)$ and $Iq(\Delta x_3)$) and then

[1]Refer to chapter 4 for the symbols used here.

substituted in formula A.1. More precisely, assuming that the three points $(\Delta x_1, Iq(\Delta x_1))$, $(\Delta x_2, Iq(\Delta x_2))$ and $(\Delta x_3, Iq(\Delta x_3))$ are on the same line the equality

$$-\frac{\log \dfrac{Iq(\Delta x_2) - Iq(\Delta x = 0)}{Iq(\Delta x_1) - Iq(\Delta x = 0)}}{\log \dfrac{\Delta x_2}{\Delta x_1}} - \frac{\log \dfrac{Iq(\Delta x_3) - Iq(\Delta x = 0)}{Iq(\Delta x_2) - Iq(\Delta x = 0)}}{\log \dfrac{\Delta x_3}{\Delta x_2}}$$

holds, and $Iq(\Delta x = 0)$ can be calculated.

A.1.1 Local parameters

The local parameters analyzed here are the position of the water front and the pressure on the vertical wall at point C (see section 4.4). The analysis of the tables A.1 and A.2 gives two different results for these two parameters. A high order of accuracy is obtained for the position of the front and a lower one is obtained for the pressure. Actually the first quantity refers to a time interval when no breaking occurs, while the second one takes into account both the impact against the wall and the breaking. Moreover the pressure calculated at point C can be very highly dependent on the local linear interpolation performed on the cell side.

$N \times N$	$1.5N \times 1.5N$	$2N \times 2N$	order
1.5496	1.5324	1.5283	3.05

Table A.1: Horizontal position of the water front: Iq for different discretizations and order of convergence of the method.

$N \times N$	$1.5N \times 1.5N$	$2N \times 2N$	order
5885.90	5854.85	5824.64	1.4

Table A.2: Pressure: Iq for different discretizations and order of convergence of the method.

A.1.2 Global parameters

Three different global parameters are analyzed here: the force acting on the bottom of the tank, and the variation of mass and energy of the system. The last two

$N \times N$	$1.5N \times 1.5N$	$2N \times 2N$	order
22545.644	22519.404	22508.971	3.0

Table A.3: Force: Iq of the for different discretizations and order of convergence of the method.

$N \times N$	$1.5N \times 1.5N$	order
1.023E-2	5.75E-3	1.42

Table A.4: Energy variation: Iq for different discretizations and order of convergence of the method.

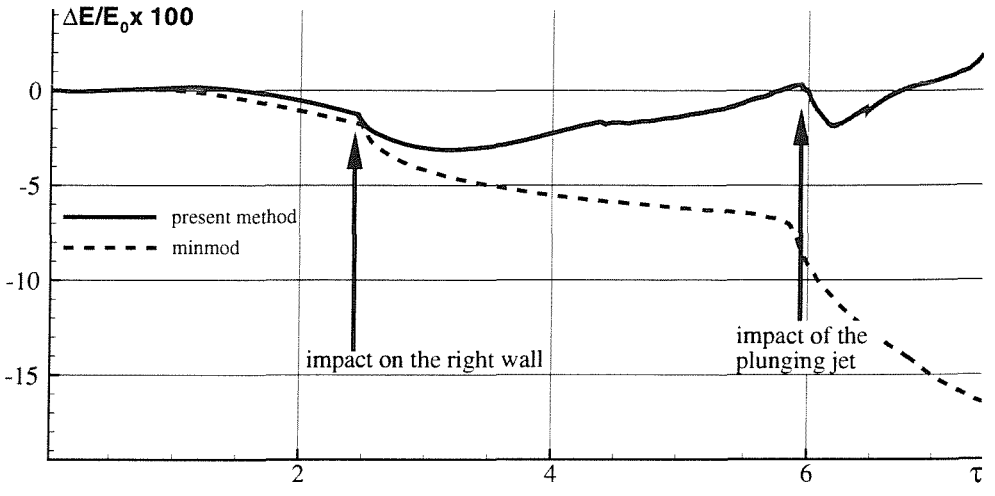

Figure A.1: Variation ΔE of the total energy divided by E_0 (difference between the initial potential energy of the water and the potential energy of the same amount of water uniformly distributed along the horizontal bottom). The present variable coefficient advection scheme is compared with a *minmod* scheme (see section 3.2.2) for a discretization $N \times N$.

$N \times N$	$1.5N \times 1.5N$	order
2.3876E-3	4.746E-4	0.94

Table A.5: Iq of the mass variation for different discretizations and order of convergence of the method.

quantities are used also to evaluate the accuracy of the method. Because, for the last two variables, the exact solution is available and, in particular it is zero, the

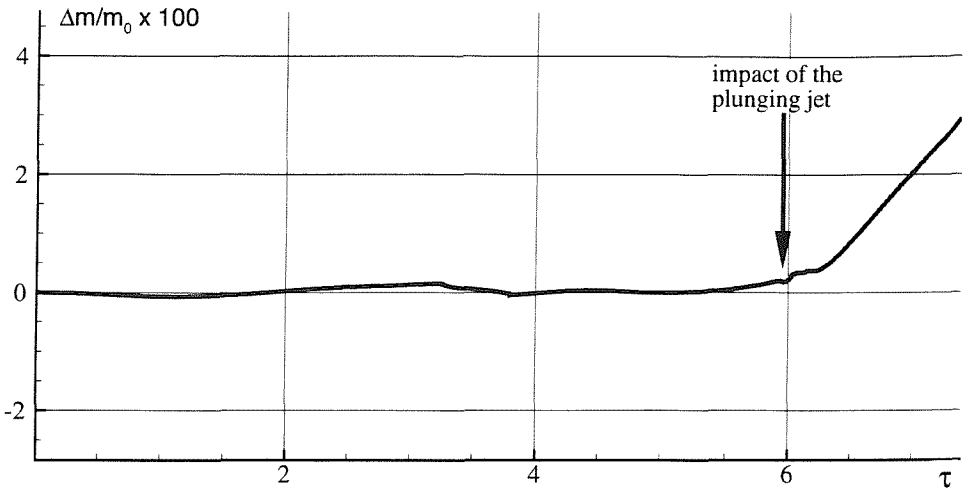

Figure A.2: Variation of the mass Δm divided by the initial mass m_0 for a discretization $N \times N$.

order of convergence can be obtained with procedure 1. The results for the mass are rather poor while a slightly better convergence is obtained for the energy. The reason for such a poor convergence is shown in figures A.1 and A.2. The former shows the behaviour of the variation of total energy. The violent phenomena of impact against a vertical wall and of the breaking cause rapid dissipation of energy. This energy is partially recovered using the variable coefficient advective scheme[2], but still the variation of the total energy is within a wide range of $\pm 3\%$.

As for the mass conservation, after the impact of the plunging jet on to the water below, figure A.2 shows that there is an increase of mass. This is due to the presence of a splash up constituted of a thin layer of water whose advection becomes difficult to model both for the level set function and for the Navier-Stokes solver because of the gradients of density across it.

A.2 Level Set algorithm

For the study of the level set function a classical problem has been chosen: the rotation of the Zalesak disk (Zalesak, 1979). A disk of radius 15 and with a central gap wide 5 and long 25 rotates around a point 20 below its centre. The velocity is

[2]In figure A.1 the energy variation obtained applying a *minmod* advective scheme is compared with the one obtained applying the variable coefficient scheme (see section 3.2.2).

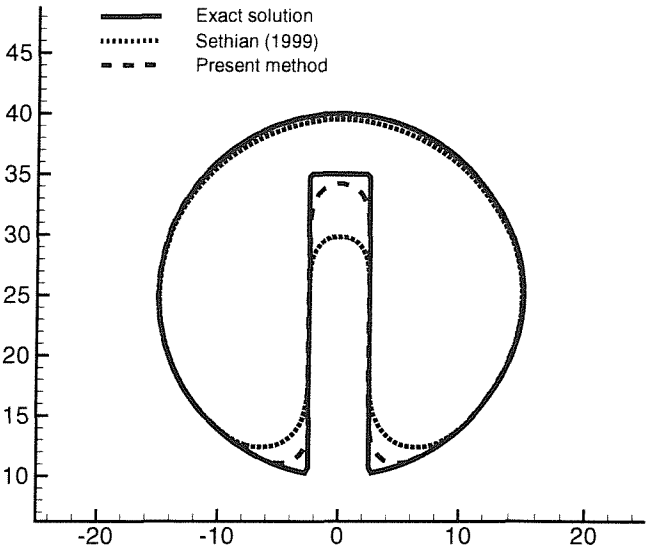

Figure A.3: Verification of the level set solutions after one revolution of the Zalesak circle.

given by

$$\begin{cases} u = -\dfrac{\pi y}{314} \\ v = \dfrac{\pi x}{314} \end{cases}$$

A field 100×100 wide is discretized using $\Delta x = \Delta y = 0.5$ and a $\Delta t = 1$. In figure A.3 the solution of the present method is compared with the one obtained using the level set reinitialization described in Sethian (1999). Even though the angles of the circle is not perfectly preserved the shape of this particular disk are quite well preserved.

Appendix B

Vorticity and pressure: the retention of bubbles at a vortex core

A vortex core is always associated with a fall in pressure. Here the example of the stationary vortical field is analyzed in the polar system (r, θ).
The velocity field is characterized by the following radial and tangential velocities

$$u_r = 0; \quad u_\theta = \frac{1 - e^{(-r^2)}}{r}$$

where the vorticity is equal to

$$\omega = \frac{\frac{1 - e^{(-r^2)}}{r} + r\,(-\frac{1 - e^{(-r^2)}}{r^2} + 2\,e^{(-r^2)})}{2r}$$

The momentum conservation equations read as

$$\begin{aligned} \frac{\partial u_r}{\partial t} &= 0 = \frac{-\left(\frac{\partial p}{\partial r} + u_\theta \frac{\partial u_r}{\partial \theta} - u_\theta^2 + u_r \frac{\partial u_r}{\partial r}\right)}{r} \\ \frac{\partial u_\theta}{\partial t} &= 0 = \frac{r u_r \frac{\partial u_\theta}{\partial r} - \frac{\partial p}{\partial \theta} + u_\theta u_r + u_\theta \frac{\partial u_\theta}{\partial \theta}}{r} \end{aligned}$$

This implies a pressure field equal to

$$p(\theta, r) = -\frac{1}{2}\frac{1}{r^2} + \frac{1}{e^{(r^2)}\,r^2} - \mathrm{Ei}(1,\, r^2) - \frac{1}{2}\frac{1}{(e^{(r^2)})^2\,r^2} + \mathrm{Ei}(1,\, 2\,r^2)\ ,$$

Where Ei is the exponential integral (Abramowitz & Stegun, 1965). Figure B.1 shows the radial distribution of velocity, vorticity and pressure. Where the

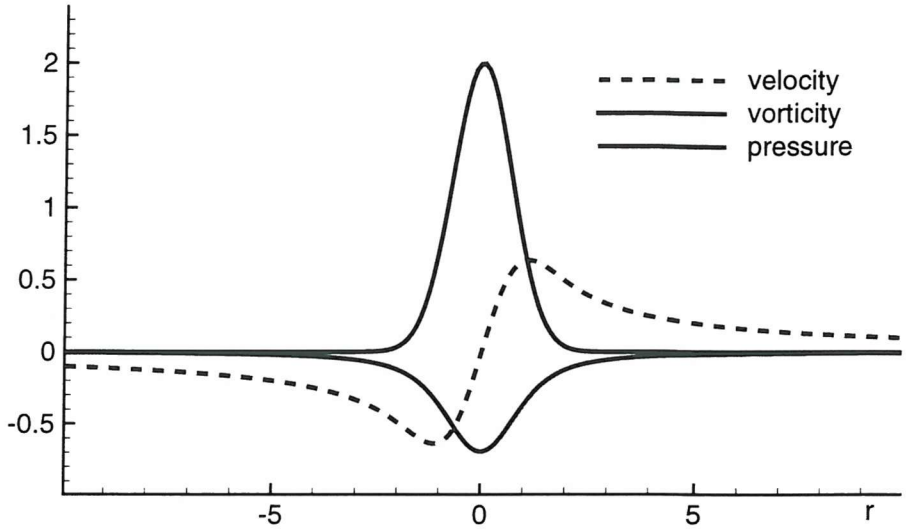

Figure B.1: Velocity, vorticity and pressure distribution for a stationary vortical field.

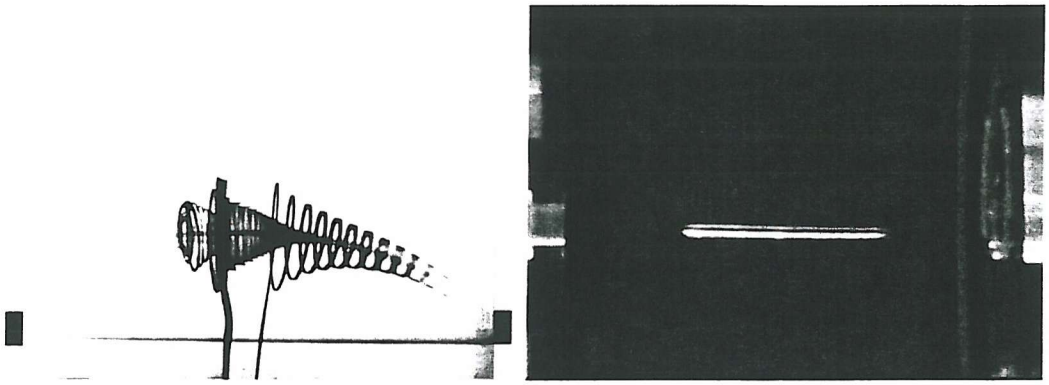

Figure B.2: Experimentally induced vortical field (Petitjeans, 2003). The vorticity in highlighted in the left side of the figure by a coloured ink and a bubble forms in the core of the vortical field in the right.

vorticity has a maximum, the pressure field has a minimum. The immediate effect of this behaviour is shown in Petitjeans (2003) where a vortical field is created in water and visualized with coloured ink in the left side of figure B.2. Even though the pressure is above the threshold value of cavitation, smaller bubbles dispersed in water concentrate in the centre of the vortical field, merging in a long bubble along the axis of vorticity as shown in the right side of figure B.2.

Appendix C

Surface piercing plate

C.1 Modelling of the problem

The vertical plate with no thickness can be very easily introduced in the numerical analysis.

Assuming that the domain is infinite the plate has been chosen as system of reference for the present computation. Positioning it at the centre of a strip of cells, exactly where the horizontal velocity is defined, the boundary conditions are automatically defined on the plate.

The total domain used for the simulation has a length equal to $40h$ and a depth equal to $d = 15h$ so that almost infinite depth conditions are achieved, where h is the initial submergence of the plate; inflow and outflow conditions are imposed at the vertical sides of the computational mesh, these statements should reduce to a minimum the effects of reflections from the real numerical boundaries.

No other change is introduced in the numerical algorithm. The position of the interface is always traced by a single LS function, advected with the velocity results of the NS equations, with wall conditions on the plate. A good and accurate solution in the reinitialization procedure and the assumption that the exact distance is defined in a narrow band makes it easy to deal with the interface reaching the lower tip of the plate. In figure C.1, the level contours in the tube around the interface are shown for a very coarse mesh. The negative contours are drawn with solid lines, the positive contours with dashed lines, and the thicker line is the zero level. The negative lines are interrupted below the plate for graphical reasons only. They are continuous in the computation and are closed behind the plate.

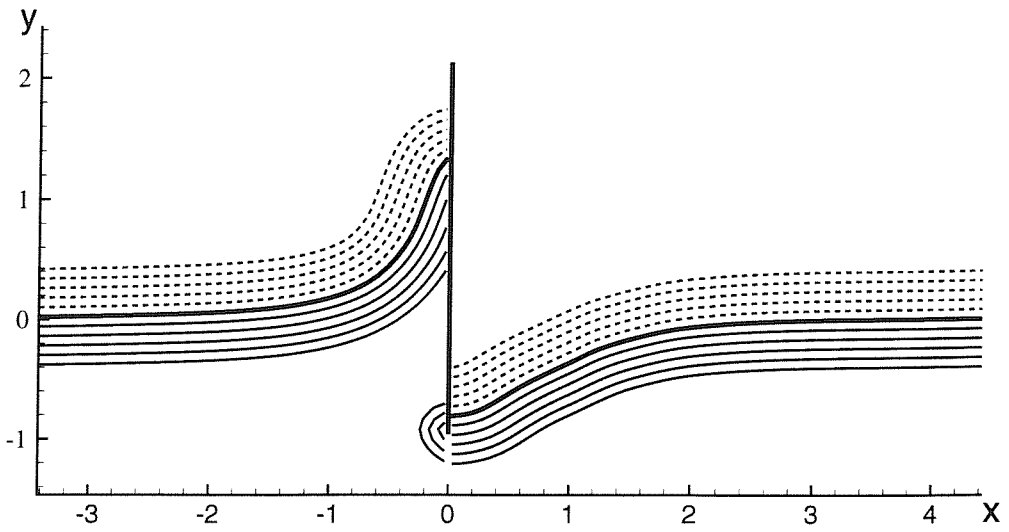

Figure C.1: Example of the displacement of the distance function when the interface reaches the lower tip of the plate. The solid lines are the negative contours, the dashed line the positve.

C.2 Impulsive start

Here the case of an impulsive start is analysed, the plate velocity is $U(t) = U_0 H(t)$ where $H(t)$ is the Heaviside function.

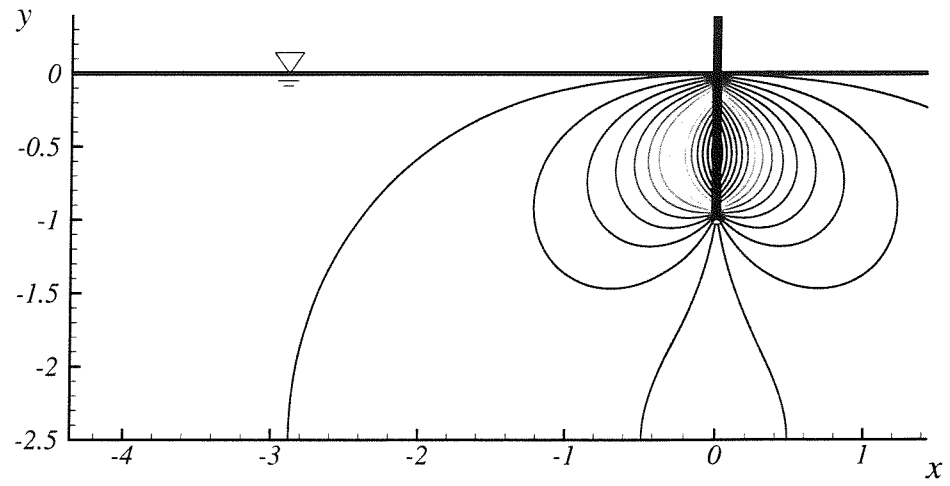

Figure C.2: *Pressure impulse* contours.

The pressure at the initial time step is represented in figure C.2. A more detailed analysis of the initial pressure obtained using different time steps leads to the figures C.3 and C.4. There, on the right hand side, there is the value $p\Delta t/\rho u$

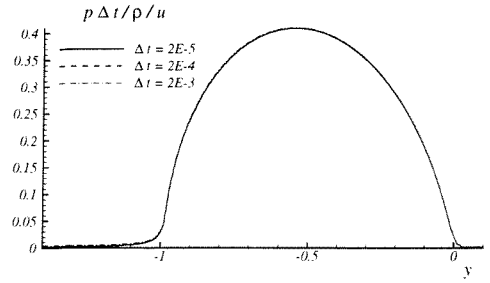

Figure C.3: Pressure on the left side of the plate at the first time-step, for different Δt.

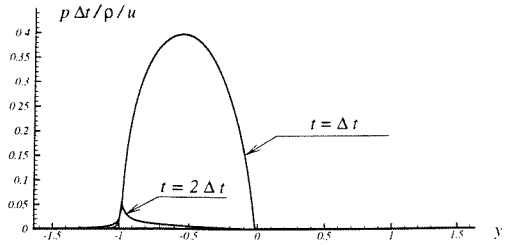

Figure C.4: Pressure distribution at two successive time steps.

close to the left face of the plate for different values of Δt. On the left there is the pressure profile at the first two time steps. There is a large difference between these two profiles. that can be explained using the *pressure impulse* theory (Batchelor, 1967).

The impulsive motion of the plate cases a large change of pressure gradients and the pressure gradient causes a velocity redistribution across the fluid. As the main terms in the equation of motion are the velocity time derivative and the pressure gradient, the Navier-Stokes equation can be simplified as:

$$\frac{\partial \boldsymbol{u}}{\partial t} = \frac{1}{\rho}\nabla p \tag{C.1}$$

so that

$$\boldsymbol{u}_a - \boldsymbol{u}_b = \int_{t_b}^{t_b} \frac{1}{\rho}\nabla p, \quad \nabla^2 P = 0 \tag{C.2}$$

with t_b and t_a respectively the time immediately before the plate starts to move and soon after the motion. The right hand side of equation C.2 is exactly the *pressure impulse*. From a discrete point of view it is the result of the first time step. So the profiles in figures C.2-C.4 are the integral of pressure in the time Δt.

From an experimental point of view it is possible to see that the pressure due to the water impacting on a wall behaves similarly to the one shown in the figure C.5, but measurements of the position of the peak and of its magnitude are not repeatable; nonetheless the pressure impulse can be measured with a good accuracy.

An analytical solution for a problem similar to the one analysed here is shown in Cooker & Peregrine (1995). There a wall limits a semi-infinite rectangle of water and a part of it starts to move with an infinite acceleration. If the water depth is $h = d$ and the length of the wall that starts to move is μh, the pressure

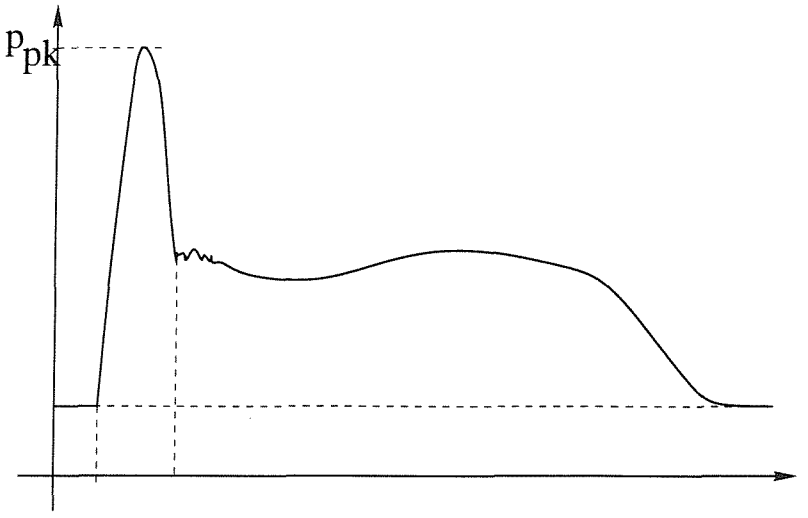

Figure C.5: The pressure evolution at a point on a sea wall undergoing wave impact (Cooker & Peregrine, 1995).

distribution on the wall is

$$2\rho h U_0 \sum_{n=1}^{\infty} \frac{\sin\left(\frac{\left(n-\frac{1}{2}\right)\pi y}{h}\right)\left(\cos\left(\frac{\left(n-\frac{1}{2}\right)\pi \mu}{h}\right)-1\right)}{\left(n-\frac{1}{2}\right)^2 \pi^2} \tag{C.3}$$

Where the y axis is positive in air and has its zero at the interface position.

That kind of pressure distribution is shown in figure C.6, and is very similar to

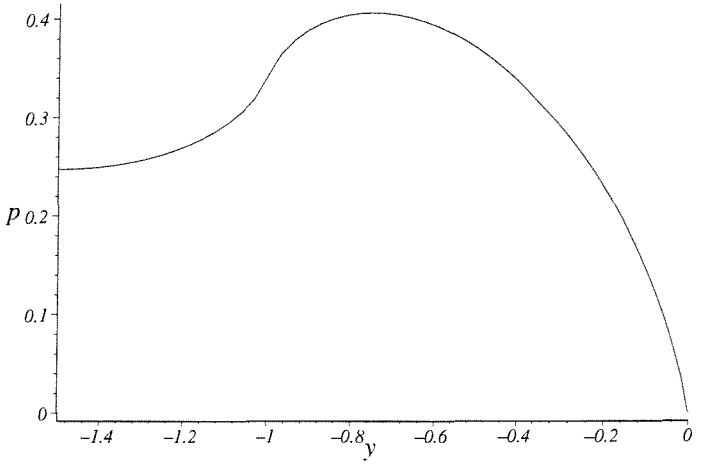

Figure C.6: Analytical solution: Pressure on the wall, whose section $[-1, 0]$ impulsively starts to move. (Cooker & Peregrine, 1995).

the one shown in figure C.3 except in the area below the plate where different

conditions are applied. In fact, neglecting the initial hydrostatic pressure, an anti-symmetric pressure is present in that area.

The method currently used is not very suitable for capturing exactly the initial velocity field for a viscous fluid with a no slip condition at the wall. In fact the singular solution can only be captured by using an expanding mesh with the mesh size proportional to the time and inversely proportional to the Reynolds number (Collins & Dennis, 1971). However the solution obtained can give an overall indication of the force acting on the plate at the start up and that after only a few time steps the solution can be reliable.

Practically the first time step approximately represents the pressure impulse. The following time steps show a drop in pressure similar to the one presented in figure C.5. The numerical drop is smoothed on several steps and gives a smoothed overshoot of the force acting on the plate.

Appendix D

Vorticity and free surface evolution for different plate inclinations

In this appendix there are seven sets of images representing the evolution of the flow field at $Fn = 0.8$ for different inclinations of the plate. For simplicity the images are represented in the frame of reference of the plate so that there is a current from left to right superimposed on them. The seven sets of snapshots refer to the non dimensional times $t\sqrt{g/h}$=0.6, 1.2, 1.8, 2.4, 3.0 and 3.6. In particular, from figure D.1 to figure D.7 the inclination of the plate varies from the angle $\alpha = -45^o$ to the angle $\alpha = 45^o$ with a $\Delta\alpha = 15^o$.

When the inclination of the plate is the lowest, the free surface in the right side of the plate drops down almost to the lower tip, so that the free surface is largely affected by the presence of the vorticity released. As soon as the inclination increases, the suction effect diminishes as well as the intensity of the vorticity released. Nonetheless the vortex sheet is less stable and rolls up on intself.

On the left side of the plate instead the different inclination influences directly the intensity of the jet forming from right to left. At $\alpha = -30^o$ the plunging jet appears, and it becomes more energetic with a higher inclination, until at $\alpha = 30^o$ a second jet forms and rises on the plate. This jet will reach a maximum height and then it will fall down with a parabolic trajectory.

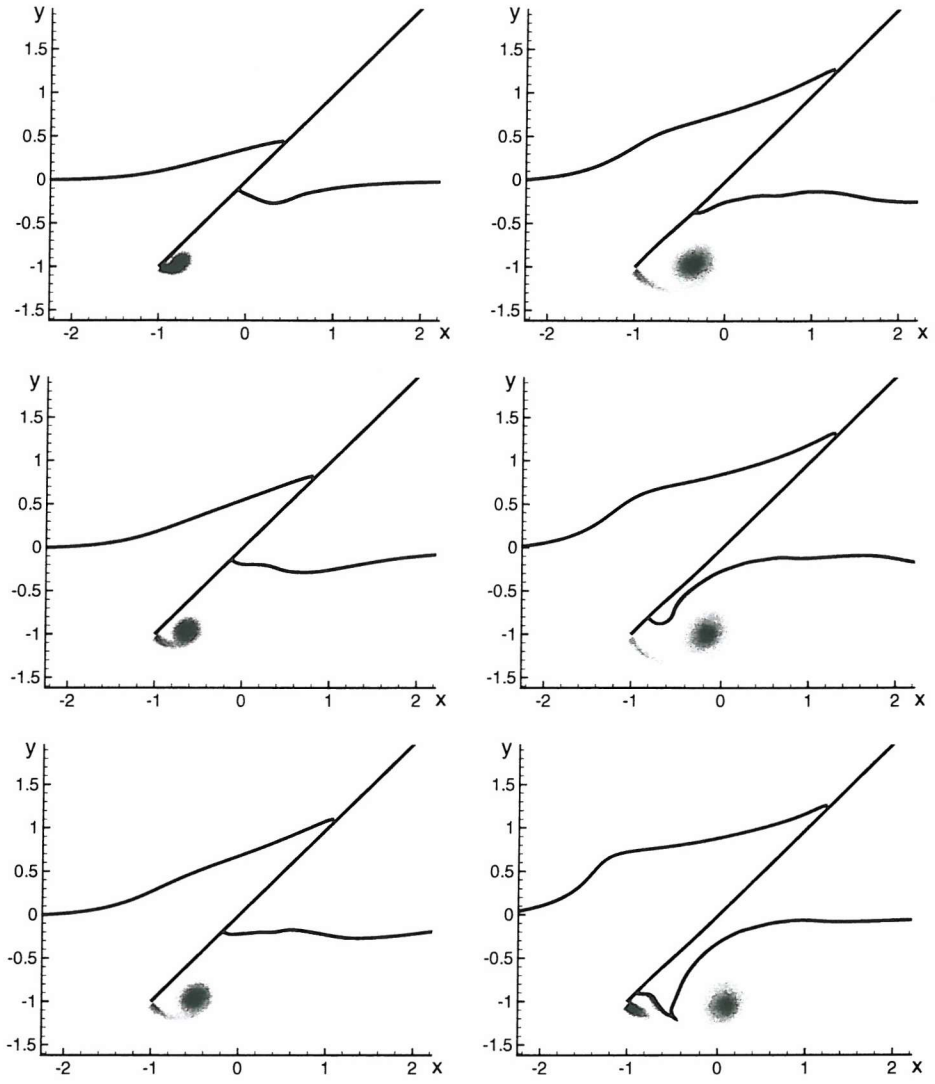

Figure D.1: Deformation of the free surface and vorticity contours for a flate plate with and inclination of $\alpha = -45^o$ from the vertical position (From top to bottom and from left to rigth the snapshosts refer to the non dimensional times $t\sqrt{g/h}$=0.6, 1.2, 1.8, 2.4, 3.0 and 3.6).

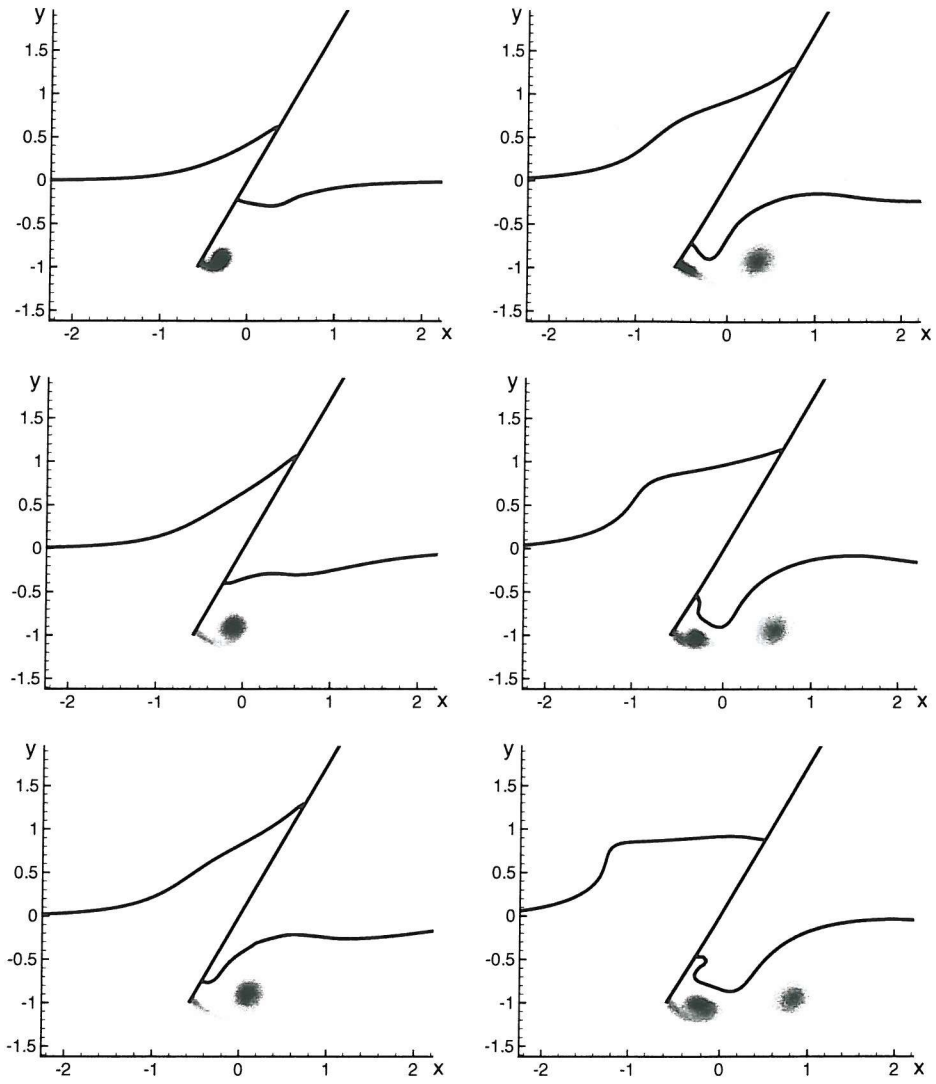

Figure D.2: Deformation of the free surface and vorticity contours for a flate plate with and inclination of $\alpha = -30^o$ from the vertical position (From top to bottom and from left to rigth the snapshosts refer to the non dimensional times $t\sqrt{g/h}$=0.6, 1.2, 1.8, 2.4, 3.0 and 3.6).

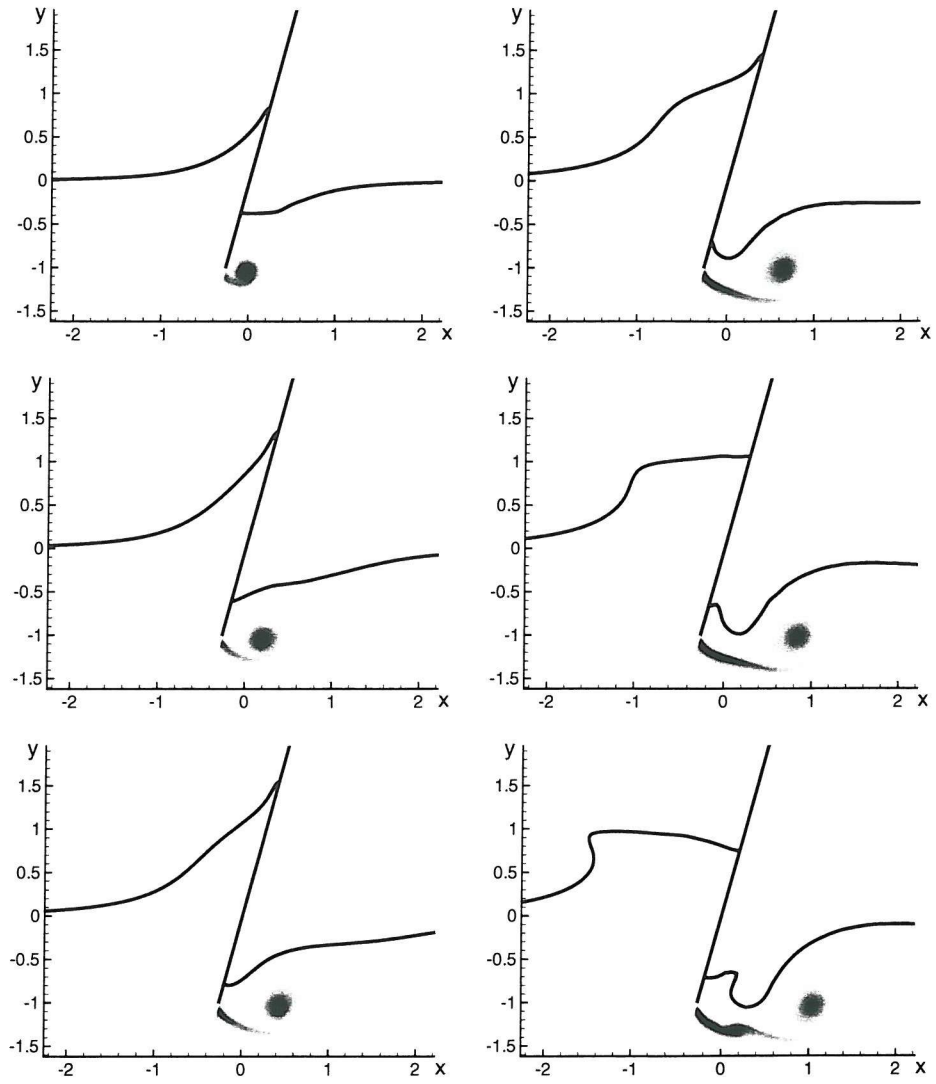

Figure D.3: Deformation of the free surface and vorticity contours for a flate plate with and inclination of $\alpha = -15^o$ from the vertical position (From top to bottom and from left to rigth the snapshosts refer to the non dimensional times $t\sqrt{g/h}$=0.6, 1.2, 1.8, 2.4, 3.0 and 3.6).

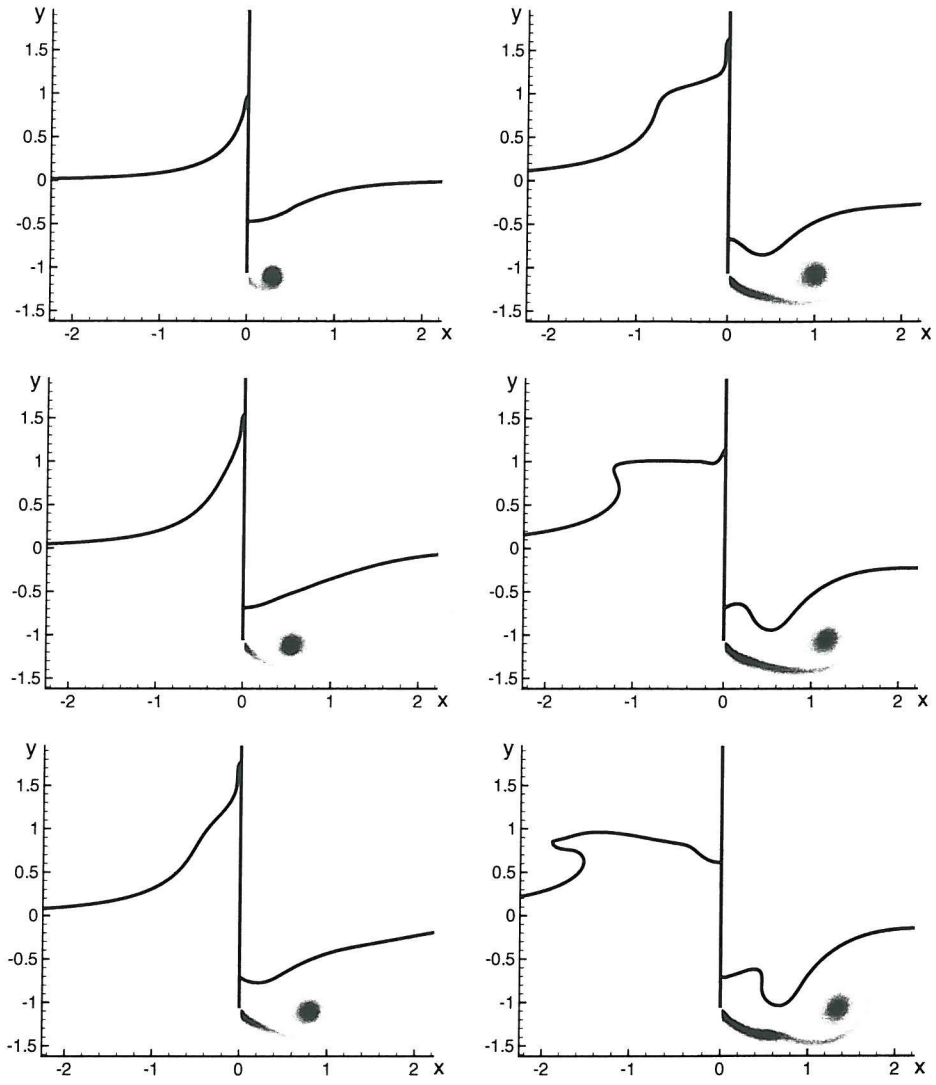

Figure D.4: Deformation of the free surface and vorticity contours around a vertical plate (From top to bottom and from left to rigth the snapshosts refer to the non dimensional times $t\sqrt{g/h}$=0.6, 1.2, 1.8, 2.4, 3.0 and 3.6).

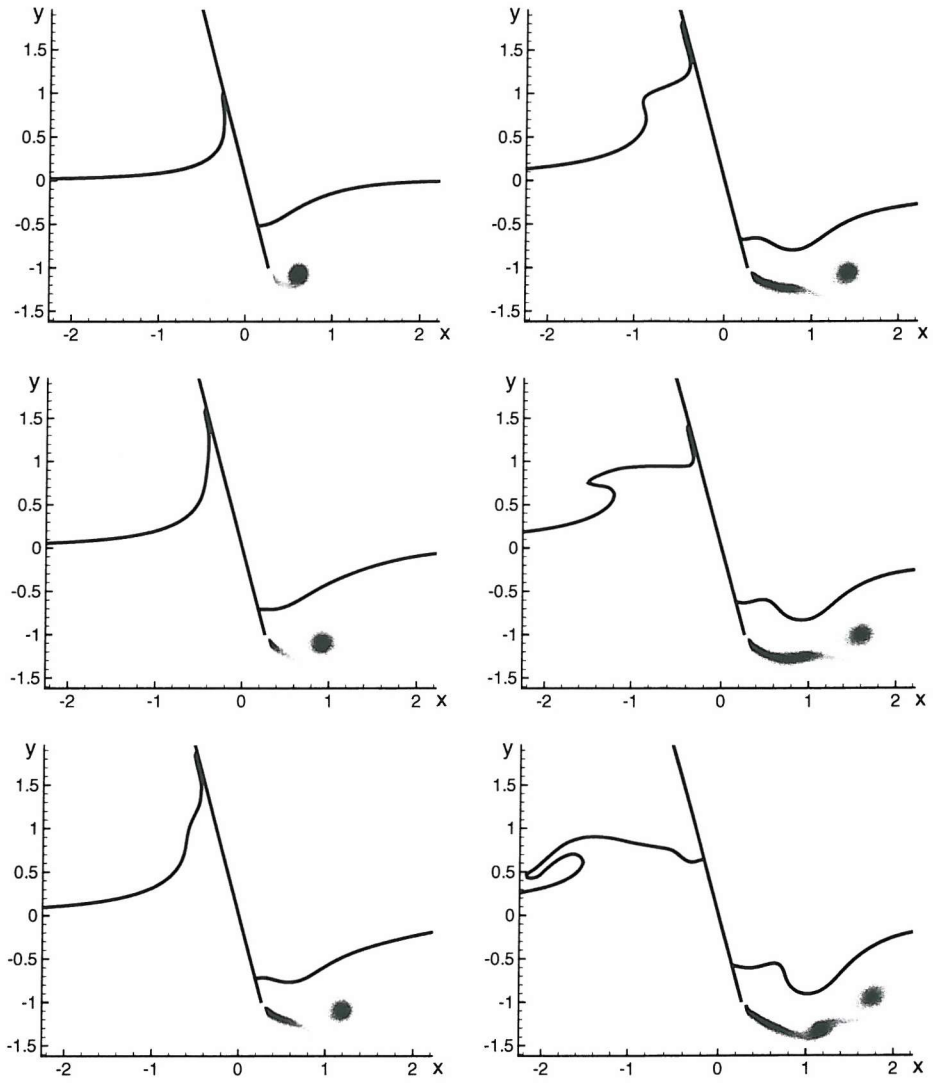

Figure D.5: Deformation of the free surface and vorticity contours for a flate plate with and inclination of $\alpha = 15^o$ from the vertical position (From top to bottom and from left to rigth the snapshosts refer to the non dimensional times $t\sqrt{g/h}$=0.6, 1.2, 1.8, 2.4, 3.0 and 3.6).

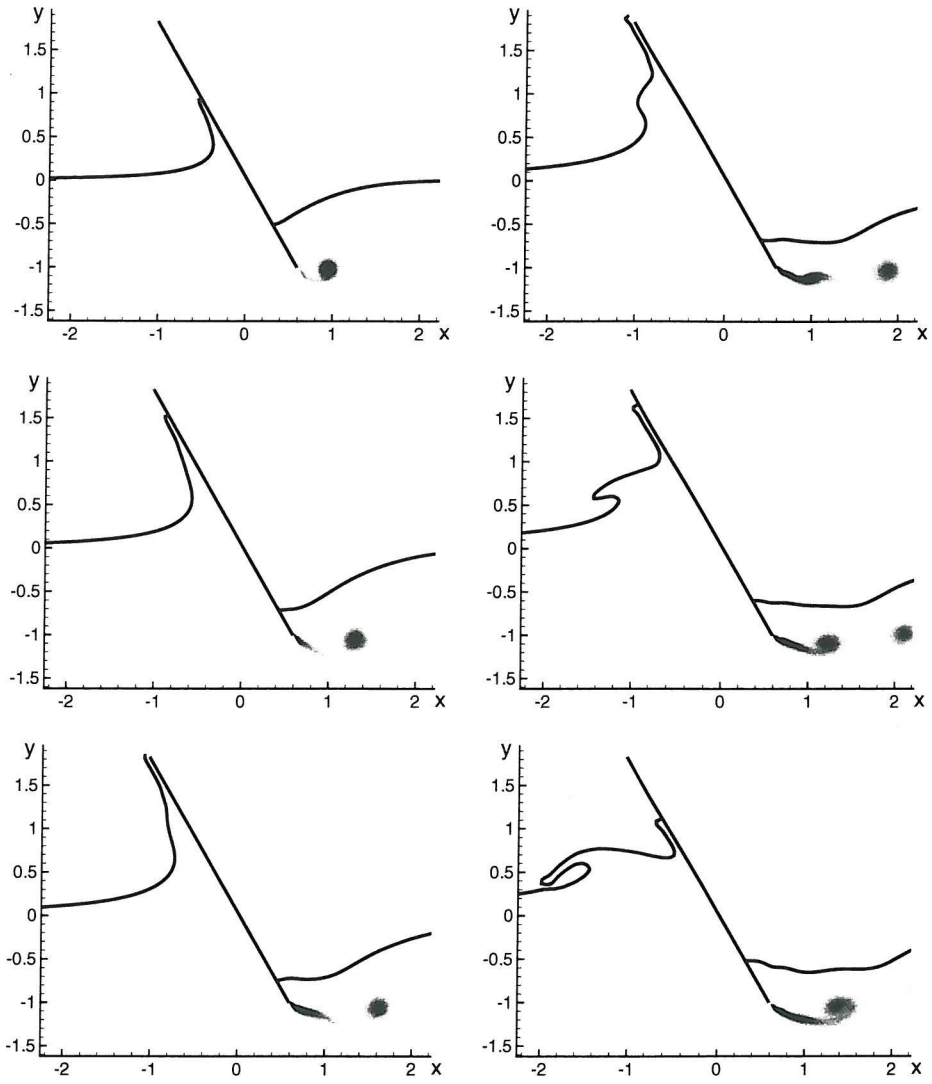

Figure D.6: Deformation of the free surface and vorticity contours for a flate plate with and inclination of $\alpha = 30^o$ from the vertical position (From top to bottom and from left to rigth the snapshosts refer to the non dimensional times $t\sqrt{g/h}$=0.6, 1.2, 1.8, 2.4, 3.0 and 3.6).

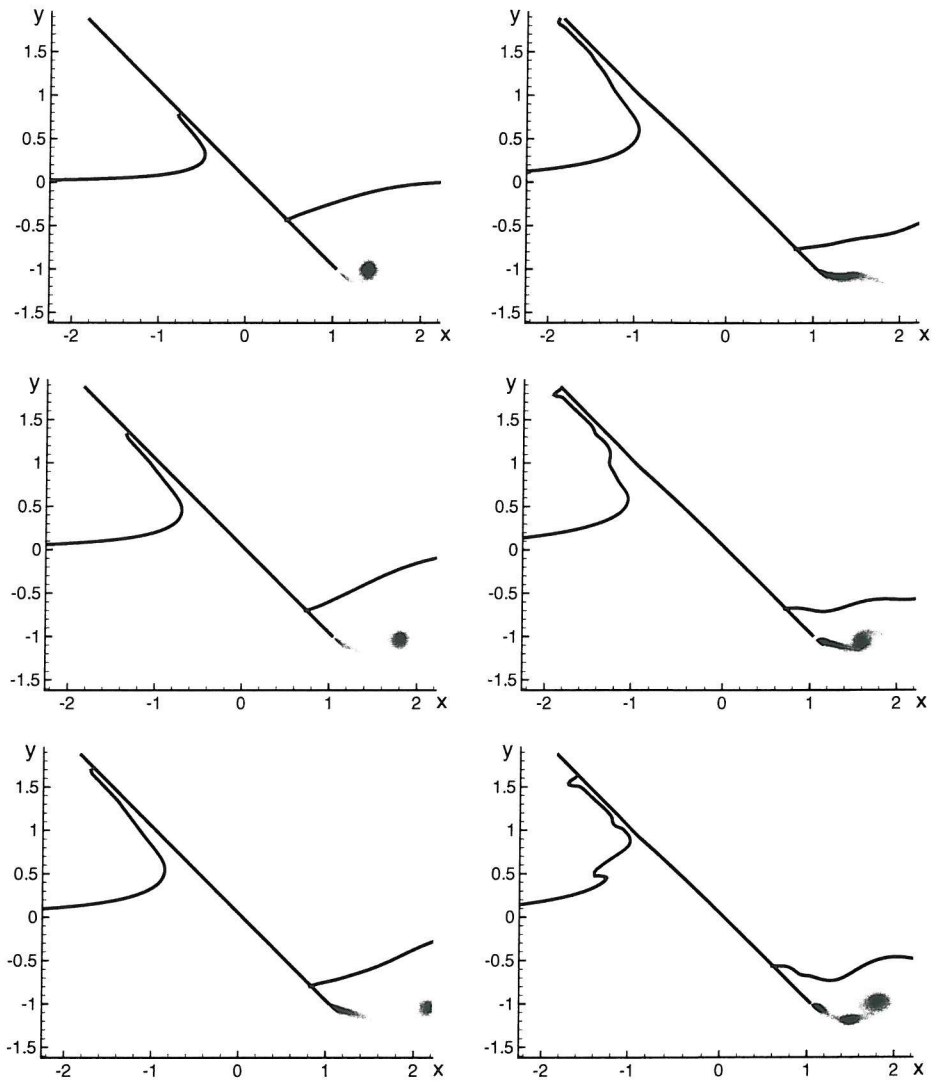

Figure D.7: Deformation of the free surface and vorticity contours for a flate plate with and inclination of $\alpha = 45^o$ from the vertical position (From top to bottom and from left to rigth the snapshosts refer to the non dimensional times $t\sqrt{g/h}$=0.6, 1.2, 1.8, 2.4, 3.0 and 3.6).

Appendix E

A generic body on a Cartesian grid

Usually a boundary fitted mesh is used to model the presence of bodies inside the fluid domain. Such a mesh presents two fundamental drawbacks: a re-mesh is necessary every time the body moves, or the calculations have to be performed in the frame of reference of the body. Both these approaches can present some problems; more precisely, in the first case, the computation becomes inefficient if the body moves continuously and the second option becomes inapplicable if two bodies moving differently are present in the fluid domain. If the mesh is kept fixed a special treatment has to be adopted to link the equations of motion of the fluid with those of the solid body. For this purpose a level set function ψ is computed around the body. It is positive in the points outside the body and negative otherwise. A function $s(\psi)$ is introduced with

$$s(\psi) = \begin{cases} 1 & \text{if } \psi > 0 \\ 0 & \text{if } \psi \leq 0 \end{cases} \tag{E.1}$$

And the Navier-Stokes equations are written as [1]:

$$u^{n+1} = s(\psi)[u^n - \Delta t[/u \cdot \nabla)u]^{n+1/2} - \Delta t \frac{\nabla p}{\rho} + g\Delta t] + (1 - s(\psi))U^{n+1} \tag{E.2}$$

[1] The discrete equations are written here in the non viscous case for simplicity but their extension to the viscous case is straightforward.

where U^{n+1} is the velocity of the body. Applying the divergence operator:

$$\begin{aligned}\nabla u^{n+1} &= s(\psi)\nabla\cdot[u^n - \Delta t[(u\cdot\nabla)u]^{n+1/2} - \Delta t\frac{\nabla p}{\rho} + g\Delta t] - s(\psi)\nabla\cdot U^{n+1} \\ &+ \frac{\partial s(\psi)}{\partial\psi}\boldsymbol{n}\cdot[u^n - \Delta t[(u\cdot\nabla)u]^{n+1/2} - \Delta t\frac{\nabla p}{\rho} + g\Delta t] - \frac{\partial s(\psi)}{\partial\psi}\boldsymbol{n}\cdot U^{n+1}\end{aligned} \tag{E.3}$$

The left hand side is zero by definition and the equation can be written as:

$$\begin{aligned}0 &= s(\psi)\nabla\cdot[u^n - \Delta t[(u\cdot\nabla)u]^{n+1/2} - \Delta t\frac{\nabla p}{\rho} + g\Delta t - U^{n+1}] \\ &+ \frac{\partial s(\psi)}{\partial\psi}\boldsymbol{n}\cdot[u^n - \Delta t[(u\cdot\nabla)u]^{n+1/2} - \Delta t\frac{\nabla p}{\rho} + g\Delta t - U^{n+1}]\end{aligned} \tag{E.4}$$

As $\partial s(\psi)/\partial\psi$ is a step function, if $\psi = 0$, then the pressure gradient on the body is such that the normal velocity of the fluid becomes equal to the velocity of the wall. In the numerical simulations the function $s(\psi)$ is smoothed on a finite number of cells across the body boundary.

References

ABRAMOWITZ, M. & I. STEGUN (1965). Handbook of Mathematical Functions. *Dover Publications Inc. New York.*

BAI, H. & B. G. THOMAS (2001). Bubble formation during horizontal gas injection into downward- flowing liquid. *Metall. Mater. Trans. B-Proc. Metall. Mater. Proc. Sci. 32*, 1143–1159.

BARTH, T. J. & H. DECONINCK (1999). High-Order Methods for Computational Physics. *Springer*.

BATCHELOR, G. K. (1967). An introduction to fluid dynamics. *Cambridge : C. U. P.*.

BIRKHOFF, G. (1962). Helmotz and Taylor instabilities. *Proc. Sympos. Appl. Math. 55*, 55–76.

BONETTO, F. & J. R. T. LAHEY (1993). An experimental study on air carryunder due to a plunging liquid jet. *J. Multiphase Flow 19*, 281–294.

BRACKBILL, J. U., D. B. KOTHE, & C. ZEMACH (1992). A continuum method for modeling surface tension. *J. Comput. Physics 100*, 335–354.

BREBBIA, C. A. & H. POWER (1999). Boundary Elements XXI Advances in Boundary Elements. *WIT Press*.

BRYANT, E. A. & J. NOTT (2001). Geological indicators of large tsunami in Australia. *Natural Hazards 24*, 321–249.

CAIDEN, R., R. P. FEDKIW, & C. ANDERSON (2001). A numerical method for two phase flow consisting of separate compressible and incompressible regions. *J. Comput. Physics 166*, 1–27.

CHANG, K. A. & P. L. LIU (1998). Velocity, acceleration and vorticity under a breaking wave. *Phys. Fluids 10*, 327–329.

CHORIN, A. J. (1967). A numerical method for solving incompressible viscous flow problems. *J. Comput. Physics 2*, 12–26.

COLAGROSSI, A. & M. LANDRINI (2003). Numerical simulation of interfacial flows by Smoothed Particle Hydrodynamics. *J. Comp. Phys. 191*, 448–475.

COLLINS, W. M. & S. C. R. DENNIS (1971). The initial flow past an impulsively started circular cylinder. *Q. J. Mech. Appl. Maths 26*, 53–75.

COOKER, M. J. & D. H. PEREGRINE (1995). Pressure-impulse theory for liquid impact problems. *J. Fluid Mech. 297*, 193–214.

DONG, R. R., J. KATZ, & T. T. HUANG (1997). On the structure of bow waves on a ship model. *J. Fluid Mech. 346*, 77–115.

DRESSLER, F. (1954). Comparison of theories and experiments for the hydraulic dam brak wave. *Ass. Int. d'Hydrologie Scientifique, Assembleè Generale de Rome*, 319–328.

ENGQYUST, B. & S. OSHER (1981). One-sided difference approximations for nonlinear conservation laws. *Mathematics of Computation 36*, 321–352.

ENRIGHT, D., R. FEDKIW, J. FERZIGER, & I. MITCHELL (2002). A Hybrid Particle Level Set Method for Improved Interface Capturing. *J. Comput. Phys. (in press).*

FINGAS, M. S. & C. E. BROWN (2001). Review of ship detection from airborne platforms. *CANADIAN JOURNAL OF REMOTE SENSING 27*, 379–385.

FRAIGNEAU, Y., J. L. GUESRMOND, & L. QUARTAPELLE (2001). Approximation of variable density incompressible flows by means of finite elements. *Commun. Numer. Methods Eng. 17*, 893–902.

GOPALAN, S. & J. KATZ (2000). Flow structure and modelling issues in the closure region of attached cavitation. *Phy. Fluids 12*, 895–911.

GRECO, M. (2001). *A two-dimensional study of green-water loading.* Ph. D. thesis, Dept. Marine Hydrodynamics, NTNU, Trondheim.

GRUNEFELD, G., H. FINKE, J. BARTELHEIMER, & S. KRUGER (2000). Probing the velocity of gass and liquid phase simultaneously in a two-phase flow. *Exp. Fluids 29*, 322–330.

HARLOW & WELCH (1965). Numerical caluclation of time dependent viscous incompressible flow of fluids with free surface. *Phy. Fluids 8*, 2182.

HARTEN, A. (1983). High resolution schemes for hyperbolic conservation laws. *J. Comp. Phys. 49*, 357–393.

HARTEN, A. & S. OSHER (1987). Uniformly high-order accurate nonoscillatory schemes. I. *SIAM J. Numer. Anal. 24*, 279–309.

HELENBROOK, B. T., L. MARTINELLI, & C. K. LAW (1999). A numerical method for solving incompressible flow problems with a surface of discontinuity. *J. Comput. Physics 148*, 366–369.

HIBIKI, T., S. HOGSETT, & M. ISHII (1998). Local measurement of interfacial area, interfacial velocity and liquid turbulence in two-phase flow. *Nuclear Engineering and Design 184*, 287–304.

HIRSH, C. (1988). Numerical computation of internal and external flows. *J. Wiley & sons.*

HIRT, C. W. & B. D. NICHOLS (1981). Volume of fluid (VOF) method for the dynamics of free boundaries. *J. Comput. Physics 39*, 201–225.

HONJI & TANEDA (1972). *Rep. Res. Inst. Appl. Mech. Kyushu University 19*, 265.

HOU, T. Y., J. S. LOWENGRUB, & M. J. SHELLEY (2001). Boundary integral methods for multicomponent fluids and multiphase materials. *J. Comput. Phy. 169*, 302–362.

IM, I. T., W. S. KIM, & K. S. KEE (2001). A unified analysis of filling and solidification in casting with natural convection. *Int. J. Heat Mass Transf. 44*, 1507–1515.

KELECY, F. J. & R. H. PLETCHER (1997). The development of a free surface capturing approach for multidimensional free surface flows in closed containers. *J. Comput. Physics 138*, 930–980.

KIM, J. & P. MOIN (1985). Application of a Fractional-step method to incompressible Navier-Stokes Equation. *J. Comput. Physics 59*, 308–32.

KOUMOUTSAKOS, P. & D. SHIELS (1996). Simulation of the viscous flow normal to an impulsively started and uniformly accelerated flat plate. *J. Fluid Mech. 328*, 177–227.

LAFAURIE, B., C. NARDONE, R. SCARDOVELLI, S. ZALESKI, & G. ZANETTI (1994). Modelling merging and fragmentation multiphase flows with SURFER. *J. Comput. Physics 113*, 134–147.

LAWSON, N. J., M. RUDMAN, A. GUERRA, & J. L. LIOW (1999). Experimental and numerical comparisons of the break-up of a large bubble. *Experiments in Fluids 26*, 524534.

LAX, P. & B. WENDROFF (1960). System of conservation laws. *Commun. Pure Appl. Math. 13*, 217–237.

LEMOS, C. M. (1996). Higher-order schemes for free surface flows with artibrary configurations. *Int. J. Num. Methods fluids 23*, 546–566.

LERICHE, M., N. CHAUMERLIAC, & A. MONOD (2001). Coupling quasi-spectral microphysics with multiphase chemistry: a case study of a polluted air mass at the top of the Puy de Dome mountain (France). *Atmos. Environ. 35*, 5411–5423.

LI, W. Z. & Y. Y. YAN (2002). Direct-predictor method for solving steady terminal shape of a gas bubble rising through a quiescent liquid. *Numer Heat Tranf. B-Fundam. 42*, 55–71.

LIU, X., R. P. FEDKIW, & M. KANG (2000). A boundary condition capturing method for Poisson's equation on irregular domains. *J. Comput. Physics 160*, 151–178.

LONGUET-HIGGINS, M. S. & E. D. COKELET (1976). The deformation of steep surface waves on water. A numerical method of compuation. *Proc. R. Soc. London 350*, 1–26.

MARTIN, J. C. & W. J. MOYCE (1952). An experimental study of the collapse of liquid columns on a rigid horizontal plane. *Phil. Trans. Roy. Soc. London 244A*, 312–324.

MONAGHAN, J. J. (1994). Simulating Free Surface Flows with SPH. *J. Comp. Physics 110*, 399–406.

MORINISHI, Y., T. S. LUND, O. V. VASILYEV, & P. MOIN (1998). Fully conservative higher order finite difference schemes of incompressible flow. *J. Comput. Phys 143*, 90–124.

MUDDE, R. F., J. S. GROEN, & H. E. A. V. D. AKKER (1998). Application of LDA to bubbly flows. *Nuclear Engineering and Design 184*, 329–338.

NGUYEN, D. Q., R. P. FEDKIW, & M. KANG (2001). A boundary condition capturing method for incompressible flame discontinuities. *J. Comput. Physics 172*, 71–98.

OAKLEY, T. R., E. LOTH, & F. J. ADRIAN (1997). A two-phase cinematic PIV method for bubbly flows. *J. Fluids Eng. 119*, 707–712.

OHRING, S. & H. J. LUGT (1991). Interaction of a viscous vortex pair with a free-surface. *J. Fluid Mech. 227*, 47–70.

OTTO, K. (1996). Analysis of preconditioners for hyperbolic partial differential equations. *SIAM Journal on numerical analysis 33*, 2131–2165.

PENG, D., B. MERRIMAN, S. OSHER, H. ZHAO, & M. KANG (1999). A PDE-based fast local level set method. *J. Comput.t. Phys. 155*, 410–438.

PEREIRA, F. & M. GHARIB (2002). Defocusing digital particle image velocimetry and the three- dimensional characterization of two-phase flows. *Meas. Sci. Technol. 13*, 683–694.

PETITJEANS, P. (2003). Stretching of a vortical structure filaments of vorticity. *Europhysics News 34*.

PHELPS, A. D. & T. G. LEIGHTON (1998). Oceanic bubble population measurements using a buoy-deployed combination frequency technique. *IEEE J. Ocean. Eng. 23*, 400–410.

RHIE, C. M. & W. L. CHOW (1983). A numerical study of turbolent flow past an isolated airfoil with trailing edge separation. *AIAA Journal 21*, 179–195.

RITTER, A. (1892). Die Fortpflanzung der Wasserwellen. *Z. Ver. deut. Ing. 36*.

RUSSO, G. & P. SMEREKA (2000). A remark on computing distance functions. *J. Comput. Physics 163*, 51–67.

SAFFMAN, P. G. (1992). Vortex Dynamics. *Cambridge University Press*.

SCARDOVELLI, R. & S. ZALESKI (1999). Direct numerical simulation of free-surface and interfacial flow. *Annu. Rev. Fluid Mech. 31*, 567–603.

SEEGER, A., K. AFFELD, L. GOUBERGRITS, U. KERTZSCHER, E. WELLNHOFER, & R. DELFOS (2002). X-ray-based flow visualization and measurement Application in multiphase flows. *Ann N Y Acad Sci 972*, 247–253.

SETHIAN, J. A. (1999). Level set methods and fast marching methods: evolving interfaces in computational geometry, fluid mechanics, computer vision and materials science. *New York: Cambridge University Press*.

SHOPOV, P. J., P. D. MINEV, I. B. BAZHELKOV, & Z. D. ZAPRYANOV (1990). Interaction of a deformable bubble with a regid wall at moderate Reynolds-numbers. *J. Fluid Mech. 129*, 241–271.

SHU, C. W. & S. OSHER (1991). Higher-Order Essentially Nonoscillatory Schemes for Hamilton-Jacobi Equations. *SIAM J. Num. Anal. 28*, 907–922.

STANSBY, P. K., A. CHEGINI, & T. C. D. BARNES (1998). The initial stages of a dam-break flow. *J. Fluid Mech. 370*, 203–220.

SUSSMAN, M., A. S. ALMGREN, J. B. BELL, P. COLELLA, L. H. HOWELL, & M. L. WELCOME (1999). An Adaptive Level Set Approach for Incompressible Two-Phase Flow. *J. Comput. Physics 148*, 81–124.

SUSSMAN, M. & E. FATEMI (1999). An efficient, interface-preserving level set redistancing algorithm and its application to interfacial incompressible fluid flow. *SIAM J. Sci. Comput. 20*, 1165–1191.

SUSSMAN, M. & G. PUCKETT (2000). A coupled level set and volume of fluid method for computing 3D and axisymmetric incompressible two-phase flows. *J. Comput. Physics 162*, 301–337.

SUSSMAN, M., P. SMEREKA, & S. OSHER (1994). A level set approach for computing solutions to incompressible two phase flows. *J. Comput. Physics 114*, 146–159.

TRYGGVASON, G., B. BUNNER, A. ESMAEELI, D. JURIC, N. AL-RAWAHI, W. TAUBER, J. HAN, S. NAS, & Y. J. JAN (2001). A front-tracking method for the computations of multiphase flow. *J. Comput. Physics 169*, 798–759.

TSAI, W. T. & D. K. P. YUE (1993). Interaction between a free surface and a vortex sheet shed in the wake of a surface-piercing plate. *J. Fluid Mech. 257*, 691–721.

WALTERS, J. K. & J. F. DAVIDSON (1962). The inital motion of a gas bubble formed in an inviscid liquid. *J. Fluid Mech. 12*, 408–416.

WEHAUSEN, J. V. & E. V. LAITONE (1960). Handbuch der Physik. *ed W Fludge 9*, 446–778.

YABE, T., Y. OGATA, K. TAKIZAWA, T. KAWAI, A. SEGAWA, & K. SAKURAI (2002). The next generation CIP as a conservative

semi-Lagrangian solver for solid, liquid and gas. *J. Comput. Appl. Math. 149*, 267–277.

YABE, T., F. XIAO, & T. UTSUMI (2001). The constrained interpolation profile method for multiphase analysis. *J. Comput. Phys. 1969*, 556–593.

ZALESAK, S. (1979). Fully Multidimensional Flux-Corrected Transport Algorithms for Fluids. *J. Comp. Phys. 31*, 335–362.

ZHANG, S., D. K. P. YUE, & K. TANIZAWA (1996). Simulation of plunging wave impact on a vertical wall. *J. Fluid Mech. 327*, 221–254.

ZHAO, Y., H. H. TAN, & B. ZHANG (2002). A high-resolution characteristics-based implicit dual time-stepping VOF method for free surface flow simulation on unstructured grids. *J. Compu. Physics 183*, 233–273.

ZHOU, Z. Q., J. O. D. KAT, & B. BUCHNER (1999). A nonlinear 3-D approach to simulate green water dynamics on deck. *7. Int. Conf. Num. Ship Hydrod, Nantes*, 5.12–5.15.